Boundary-Layer Stabilization with Dielectric Barrier Discharge Plasmas for Free-Flight Application

Vom Fachbereich Maschinenbau
an der Technischen Universität Darmstadt
zur
Erlangung des Grades eines Doktor-Ingenieurs (Dr.-Ing.)
genehmigte

D i s s e r t a t i o n

vorgelegt von

Dipl.-Ing. Alexander Duchmann

aus Frankfurt am Main

Berichterstatter:	Prof. Dr.-Ing. C. Tropea
Mitberichterstatter:	Prof. D. Henningson
Tag der Einreichung:	01.11.2012
Tag der mündlichen Prüfung:	17.12.2012

Darmstadt 2013
D17

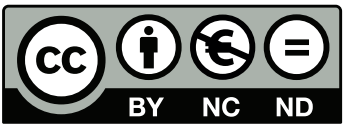

Hiermit versichere ich, die vorliegende Doktorarbeit unter der Betreuung von Prof. Dr.-Ing. C. Tropea und Dr.-Ing. S. Grundmann nur mit den angegebenen Hilfsmitteln selbständig angefertigt zu haben.

Darmstadt, den 01.11.2012.

Abstract

The present work combines experimental and numerical efforts to enhance the maturity of dielectric barrier discharge (DBD) plasma actuators as flow-control devices. In an attempt to increase the effectiveness of controlling laminar-turbulent transition, the understanding of a stabilizing effect of the actuator force field on laminar boundary-layer flow is fostered. Parametrical studies extend the Reynolds number range for effective transition control beyond the limits of earlier investigations. A numerical tool kit, consisting of a boundary-layer solver with implemented DBD force model and coupled stability analysis, is developed to predict the flow-control effectiveness. Validation experiments show considerable transition delay in a wind-tunnel setting. The excellent agreement of the experimental data with the numerical predictions renders the latter valuable for the design of flow-control applications. In order to realize an application of plasma actuators under non-laboratory conditions, a transition control experiment is designed for in-flight application on a full-sized motorized glider. The performed proof-of-concept experiment at a Reynolds number of 3×10^6 is the first to show a successful use of DBD transition control under atmospheric flight conditions. The discussion of the significantly delayed transition and resulting drag reduction concludes with an estimate for the flow-control efficiency.

Kurzfassung

Die vorliegende Arbeit kombiniert experimentelle und numerische Untersuchungen zur Strömungskontrolle mit dielektrischen Barriereentladungs-Plasma Aktuatoren. Um die Effektivität der Kontrolle des laminar- turbulenten Umschlags zu steigern wird das Verständnis für den stabilisierenden Effekt des Aktuator-Kraftfeldes auf laminare Grenzschichtströmungen verbessert. Parameterstudien erweitern den Reynoldszahlbereich, innerhalb dessen eine effektive Kontrolle der Transition möglich ist, jenseits der Grenzen vorheriger Untersuchungen. Ein numerisches Werkzeug, bestehend aus einem Grenzschicht-Löser mit integriertem Modell eines Plasma-Aktuators und gekoppelter Stabilitätsanalyse, dient zur Vorhersage der Kontrolleffektivität. Validierungsexperimente im Windkanal zeigen eine erhebliche Verzögerung der Transition. Die hervorragende Übereinstimmung der experimentellen Daten mit numerischen Vorhersagen ermöglicht die Verwendung der letztgenannten zur Auslegung von Strömungskontrollanwendungen. Um eine Anwendung von Plasma-Aktuatoren außerhalb laboratorieller Bedingungen zu realisieren wird ein Freiflug-Experiment zur Transitionskontrolle auf einem Motorsegler gestaltet. Die Machbarkeitsstudie bei einer Reynoldszahl von 3×10^6 zeigt erstmals eine erfolgreiche Anwendung von Plasma-Aktuatoren zur Transitionskontrolle unter atmosphärischen Flugbedingungen. Eine abschließende Diskussion der Transitionsverzögerung und der ermöglichten Reibungsreduktion resultiert in einer Abschätzung der Strömungskontrolleffizienz.

Acknowledgements

I would like to thank Prof. Dr. Cameron Tropea for ensuring the freedom to pursue the research summarized in this thesis while working at the Department of Fluid Mechanics and Aerodynamics as well as the Center of Smart Interfaces at TU Darmstadt. Furthermore, I appreciate the support by Dr. Sven Grundmann, who always had an open office door and engaged in fruitful discussions. The financial support by the Air Force Office of Scientific Research (Grant FA8655-08-1-3032) is thankfully acknowledged.

The successful cooperation with KTH Stockholm culminated in Prof. Dan Henningson's commitment to co-referee this thesis, for which I am truly thankful. Additionally, I thank Ardeshir Hanifi for his patience and help with the numerical implementations as well as the support during my short-term stay in Stockholm.

Without our exceptional flight-experiment crew, Andreas Reeh, Bernhard Simon, Martin Stenger, and Michael Weismüller, the airborne experiments could not have been successfully performed. I would like to thank them for their technical assistance, but even more for their help and friendly support in pursuing my aviation ambitions. Multiple experimental setups have only been completed in time due to the arduous work of the electrical and mechanical workshops, and I would like to thank the whole workforce for their persistent support.

The excellent working atmosphere at the wind-tunnel facilities in Griesheim has always been motivating, foremost due to the presence of my collaborators. I am grateful to Katrin Barckmann, Andreas Güttler, Daniela Klaubert, Jochen Kriegseis, Armin Kurz, Lars Opfer, Debora Vieira, and Alexander Widmann for their help and suggestions related to experiments and numerical studies, but also for becoming friends beyond the professional sphere. I am delighted to have supervised many excellent students who fundamentally contributed to the results of this research: Ibrahim Budde, Christoph Vetter, Daniel Stehlik, Michael Köhler, Tamino Wetz, Nikolas Kienzle, Philip Magin, Tim Denk, and Kilian Lackhove.

Finally, I would like to express my deepest gratitude to my family as well as my friends and Katharina, who unconditionally supported me during the good and hard times of my doctoral studies.

Contents

1 Introduction

Advancements within the field of aerodynamics, especially driven by increasing potential of sophisticated computational tools, have led to high levels of predictability and optimization of airflow situations. Besides optimized design of airfoil and fuselage shapes, passive flow-control methods like riblets provide additional benefits if designed correctly and applied wisely. Nevertheless, such passive methods usually enhance the efficiency only in a small range around the design point and provoke derogatory effects if this condition is left. This can be caused by flow unsteadiness or changes of ambient conditions, leading to deteriorated performance. Economically and ecologically motivated holistic efficiency considerations over the whole mission of an aerodynamic object require a customized removal of such undesired effects. Active control strategies can beneficially influence the flow at the design state as well as under non-optimal conditions at the expense of energy consumption. The overall relevance of such flow control is comprehensively reviewed by Gad-el-Hak [39] and Arnal and Archambaud [6], providing theoretical and practical approaches. Variation of the expended energy allows for adaptation of the control effectiveness, and variable positioning of flow-control devices enables improvements under off-design conditions. The necessity to spend energy on active flow manipulation requires accurate development of the flow-control application. Only efficient design capacitates dramatic changes of the global flow behavior for minute localized efforts. Surface implementation empowers on-demand use and unobstructed flow without interfering naturally ideal conditions. During the last decade, dielectric barrier discharge (DBD) plasma actuators have demonstrated effective means of active flow control in a wide range of applications.

It is the aim of the present thesis to explore the working mechanisms, the predictability and the efficiency of such devices for transition control. A combination of experimental and numerical investigations is presented to show efficient transition delay and drag reduction in wind tunnels and flight. The investigations focus on an explanation of the hydrodynamically stabilizing effect and the development of a design tool for DBD transition control applications under elevated Reynolds numbers in flight.

1.1 Transition Control

Approximately 47% of modern transport aircraft drag is caused by viscous friction along the wetted surfaces [31], to which the fuselage and the wings contribute about 70% [87]. If the viscous resistance can be reduced even by a small percentage, large energy savings are gained. Estimated worldwide savings of 9 million tons of carbon dioxide per year are imaginable if the friction on commercial airliners can be reduced by 1%. For drag reduction on airfoil shaped objects, delaying the detrimental transition to turbulence can energetically be up to an order of magnitude more efficient than relaminarization of a turbulent flow [53]. It is therefore desirable to maintain laminar flow as long as possible.

Some general aviation aircraft like the *HondaJet* [38] and especially sailplanes combine very smooth surfaces on the wings and fuselage with especially designed airfoils for maximized laminar flow downstream of the leading edge. This natural laminar flow (NLF) concept leads to a pronounced "laminar bucket" within the flight envelope, where the drag can be reduced by up to 50% in comparison to turbulent conditions. The range of flight states for this laminar bucket is determined by the flow speeds and chord length constituting the Reynolds number. The NLF concept is a designated design-point technique since at large Reynolds numbers or in case of a swept wing, the laminar bucket persists only over a small angle-of-attack range. Hence, active laminar flow-control (LFC) techniques are investigated to maintain the laminar flow state and delay the transition to turbulence downstream. Such active flow control combines the advantage to adapt to different flight states during a typical flight mission with a reduction of the net drag at cruise conditions. Successful proofs of concept include small slots in the surface for boundary-layer suction to increase the laminar portion of the flow over a wing glove in flight, demonstrated by Pfenninger and Groth [78]. Alternatively, a porous surface can be generated by high-precision drilling to enable continuous suction through the surface, theoretically maintaining the laminar state up to the trailing edge. Despite the flow-control success of both techniques, large suction mass-flow rates and additional mechanical installations consume the benefit. A hybrid approach called hybrid laminar flow control (HLFC), combining active flow control in the leading edge region with adequate profile shaping, can reduce the viscous drag and appears most appropriate for further research. A comprehensive list of experimental approaches to these techniques is provided by Drake and Kennelly [22]. Feasibility studies relevant for commercial aircraft industry have been conducted on a Boeing 757 wing [89]

and the tail fin of an Airbus A320 [92]. A more detailed review of methods to maintain flow laminarity in flight is provided by Arnal and Archambaud [6] whereas applicable measurement techniques for impact quantification are reviewed by Fisher et al. [32] and Anderson et al. [3].

Smart flow-control approaches are required to reduce the drawbacks of mass increase and space limitations associated with large mechanical structures. Such installations are usually necessary for flow control by means of boundary-layer suction or blowing [36]. Recent research trends in transition control tend to actively approach only the relevant transition mechanisms. Increasing knowledge about flow receptivity and different roadmaps to turbulence are combined with optimization routines to attenuate unstable flow structures. Högberg and Henningson [48] show that linear optimal control strategies can be applied to attenuate the development of different instability mechanisms in spatially evolving boundary layers. Dependent on the flow situation, either the development of Tollmien-Schlichting instabilities, cross-flow modes or global instabilities needs to be tackled to preserve the laminar state. Such reactive strategies, like active Tollmien-Schlichting wave control [45, 104], depend on sensor readings for accurate adaptation of the control action to the relevant flow structure. Following the definition of Gad-el-Hak [39], such techniques need to be differentiated from predetermined ones, e.g. changing the mean-flow stability properties of laminar mean flow [2]. Predetermined active flow-control strategies are also only effective at the cost of energy consumption but do not require real-time information about the flow. Passive mechanisms do not require the expenditure of energy to provoke a flow-control effect, e.g. the described NLF shape optimization. Another passive approach is to employ distributed roughness elements and generate streaky structures for beneficial interaction of modal instabilities [37]. Nevertheless, these passive structures are present under all flow conditions and may deteriorate performance in off-design situations, whereas active flow control may be en- and disabled as required.

Transition investigations and flow-control experiments for aeronautical applications at elevated Reynolds numbers are necessarily performed in flight. The turbulence intensities and frequency spectra encountered in the atmosphere are not reproducible in large wind-tunnel setups, as exemplarily investigated by Weismüller [114]. The experimental work shows a dependence of the turbulence conditions during flight measurements on the time of day as well as on the altitude, and compares these to wind-tunnel measurements. Figure 1.1 illustrates the energy spectra of hot-wire data

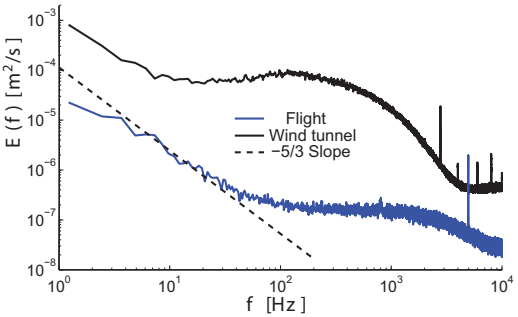

Figure 1.1: Spectra of wind-tunnel and flight turbulence, adapted from Weismüller [114].

in flight and wind-tunnel experiments. Besides a significant difference in the absolute turbulence energy level varying from $Tu = 0.09 - 0.22\%$ in flight in comparison to 0.34% in a wind tunnel, the dominant frequency range does not coincide for both data sets. The receptivity mechanisms by which disturbances enter the viscous boundary layer and initiate the turbulent breakdown depend on the amplitude and type of ambient turbulence. The transition process can differ significantly based on specific mechanisms [13] if a certain threshold (typically $Tu \approx 0.5\%$) is exceeded. Even during atmospheric flight, increased turbulence levels (e.g. caused by thermals) can lead to a deterioration of flight performance on NLF airfoils due to premature transition.

To investigate the exact reasons for this performance drop, transition experiments by Weismüller [114] are performed on a NLF wing glove on a motorized glider at TU Darmstadt. Wing gloves are commonly applied [3, 30, 75, 78, 89, 94, 95] to enable unobstructed integration of sensor equipment and flow-control devices into the surface of an airfoil. Additionally, they enable application-oriented research at elevated Reynolds numbers and realistic pressure gradients under ambient atmospheric conditions. Hence, the laminar wing glove presented in Weismüller [114] is perfectly suited to host an in-flight transition control experiment. The impact on the transition process at the design point as well as under increased turbulence intensities can be investigated under non-laboratory conditions.

1.2 DBD Flow Control

Directed body-force fields provide an intelligent and smart way for flow control and have become increasingly important throughout the last decade. Designated body-force distributions in water can be created by magneto-hydrodynamic (MHD) actuators using Lorentz forces [2] whereas electro-hydrodynamic (EHD) actuators are employed in gaseous media. Within the latter class, dielectric barrier discharge (DBD) actuators are commonly adopted. DBD actuators enjoy a broad usage in industrial applications as ozone generation, panel displays, lasers and surface treatments [55]. While such gas-discharge devices still lack the level of maturity necessary for industrial use in aerodynamic applications, the forces of the ionized gas in an electric field have been applied for manipulation of various flows in laboratory environments. At atmospheric pressures in the order of 1 bar found in many aerodynamic situations, gas discharges can be produced at reasonable energy costs and maintained for steady force production. Comprehensive reviews of flow control employing gas discharges is provided by Corke et al. [21] and Moreau [72]. Cattafesta and Sheplak [17] provide a broad overview of different flow-control actuators and identify advantages and disadvantages of each type. The main advantages of gas-discharge actuators are their short response time and force generation without moving parts.

DBD actuators with AC power supply producing a surface glow discharge have first been applied for flow control by Roth et al. [88]. The definition and working principle of such actuators is reviewed in Chapter 3.1. In the case of quiescent air above a solid surface, the force field induces a flow tangential to the wall. As the actuator represents a zero-net mass-flux device, the tangential acceleration is accompanied by a smaller wall-normal velocity component, i.e. a slow downward movement towards the exposed actuator electrode. Since the discovery of the working principle for aerodynamic applications, DBD actuators have mainly been used for separation control on airfoils at high angles of attack [12] and bluff bodies [54] as well as to control laminar-turbulent transition in fluid boundary layers. If the actuator is applied in a boundary-layer flow, it increases the wall-tangential momentum enabling a change of the boundary-layer properties. Grundmann and Tropea [44] first demonstrated that flush-mounted DBD actuators can delay artificially triggered transition on a flat plate inside a wind tunnel. It was shown that the transition delay can either be achieved by actively canceling single frequency disturbances with a pulsed actuation in a reactive manner, or by continuous forcing in a predetermined way [45].

Whereas the active cancelation of Tollmien-Schlichting waves had been performed with different flow-control devices before, the unique properties of DBD actuation to influence the flow momentum distribution paved the way for a new transition control approach. Although the exact mechanism of the continuous operation remained unknown, it was presumed that the actuator force locally changes the stability properties of the flow and/or leads to anisotropic redistribution of the velocity fluctuations. Velkoff and Ketcham [109] had utilized corona discharges earlier to obtain a delay of transition at freestream speeds around 50 m/s along a flat plate, but neither this experimental approach nor a theory for the transition impact were further developed. The main reason may be the necessary installation of corona wires above the surface, impeding an unobstructed integration into the structure. Moreau et al. [73] employed wall-mounted corona wires to alter turbulent boundary-layer profiles on a flat plate obtaining a significant drag reduction at flow velocities up to 25 m/s. Surface integrated and flush-mounted DBD actuators were applied by Magnier et al. [70] who noticed premature triggering of transition due to the DBD operation. A destabilizing effect of an orthogonal electrode configuration was observed by Gibson et al. [40] on a slotted flat plate subjected to external suction. Jacob and Ramakumar [52] investigated the impact of a single DBD actuator on a laminar boundary-layer profile at low speeds and measured a decrease of the displacement thickness δ_1 and the momentum loss thickness δ_2. Increased velocity perturbations downstream of the actuator were measured, which led the authors to apply the actuator as a tripping device for separation control. More recently, the stability impact of DBD operation has been studied by Séraudie et al. [97] who observed either a delay or acceleration of natural transition on an airfoil depending on the actuator configuration. They derived a dependency of the effect on actuator placement and voltage, a complementary numerical study enabled a stability analysis to explore the stabilizing actuator effect. The importance of thoroughly analyzing the actuator's impact on hydrodynamic stability is also underlined by recent numerical studies of Riherd and Roy [86].

Until now, all such stability investigations are based on numerical computations and lack a thorough comparison to experimental data. Additionally, all successful DBD flow-control applications so far have been limited to low Reynolds number experiments in wind tunnels. The force magnitude is limited by the discharge physics and the ambient conditions, which reduces the relative effectiveness with increasing ambient flow velocity. The present work presents a predetermined active flow-control strategy by means of

continuously operated DBD actuators to stabilize laminar boundary-layer flow and to delay Tollmien-Schlichting wave dominated transition. It is the aim of this work to foster the understanding of the stabilizing DBD effect, thereby enabling an optimization of the transition control effectiveness at increasing Reynolds numbers. The delineated application of DBD transition control under non-laboratory conditions in free-flight significantly enhances the maturity of DBD flow control.

1.3 Key Questions and Outline

The relatively new approach to use DBD actuators for transition control leaves a variety of questions to be answered.

First experiments showed the capability to delay transition on laboratory setups without exploring the physical background in detail. For flow-control purposes, it may be acceptable to neglect a thorough investigation of all discharge physics involved in the generation of the actuator force field. Nevertheless, it must be investigated how these body forces, confined to a small region around the actuator position, alter the flow field and lead to the macroscopically measurable transition delay much further downstream. The **effect on the stability properties** of the flow needs to be discussed and experimentally verified. Stability analysis can be applied to obtain a detailed view of the flow properties and to anticipate the transition process, but it remains questionable how the results relate to experimental data under the influence of DBD actuation.

Secondly, the maturity of DBD actuators as flow-control devices needs to be enhanced. Until now, successful transition delay was achieved only on generic configurations at low Reynolds numbers. At higher flow speeds and under strong adverse pressure gradients relevant for aviation applications, the actuators have not been successful in any flow-control application. The physically limited body force restricts the effectiveness of actuation in a high-momentum flow. Under such conditions, an optimization regarding the positioning and configuration of DBD actuators is necessary to design a pertinent flow-control application. An experimental optimization is time consuming and cost intensive, because of the number of variables and necessary hardware adaptations. Functional computational tools are required to circumvent measurement uncertainties and to conduct large parametrical studies. The aim is to provide a **design tool for optimization** of flow-control applications.

Finally, flow control under **non-laboratory conditions** is of importance for real-world applications. The ambient pressure, temperature and

humidity of the surrounding fluid influence the effectiveness of DBD actuation. To demonstrate that such devices can be successfully applied under varying conditions is of major importance for the credibility of all DBD flow-control research.

The structure of the present thesis is oriented as to answer the key questions and to provide further insights on DBD transition control.

Chapter 2 reviews the concepts of boundary-layer theory and hydrodynamic stability necessary for the understanding of the transition process and the numerical procedures introduced in the following chapter.

Chapter 3 elucidates details on the methodology for answering the key questions. The experimental setups and numerical tools are introduced, enabling a direct understanding of the results presented in the subsequent chapters.

Chapter 4 presents the results of generic wind-tunnel experiments based on the experimental findings by Grundmann [43]. Experiments at higher flow velocities and under natural disturbance conditions are performed showing effective transition delay at elevated Reynolds numbers. The investigations aim at the impact of the force field on the flow properties in direct vicinity of the actuator. Additionally, a parametric study on actuator positioning and force amplitudes related to the macroscopic transition location is conducted, providing rules of thumb for further design of flow-control experiments.

Chapter 5 provides numerical data on the stability properties and allows a comparison to the experimental data from the preceding chapter. The validation with experimental data demonstrates that a stability analysis of computational boundary-layer data can provide design guidelines for optimized flow-control applications. An in-flight experiment is designed and the numerical investigation allows for an estimate of the expected flow-control effect.

Chapter 6 demonstrates the application of DBD transition delay in flight and lifts the level of DBD flow control to a higher level of maturity. The impact of ambient condition variations on the flow-control performance during atmospheric flights is quantified. The identification of influencing parame-

ters allows the design of a closed-loop controller to maintain constant flow control authority at elevated Reynolds numbers and all conditions encountered during a full flight mission.

Chapter 7 summarizes the experimental and numerical results. It provides a conclusive report on the findings from a wide-ranging perspective before Chapter 8 essays an outlook for future investigations.

2 Hydrodynamic Stability

One of the main objectives of this work is to increase the understanding of boundary-layer transition under the influence of dielectric barrier discharges. In order to estimate the flow-control authority and gain insight into the physical mechanisms of transition delay, the fundamental concepts of boundary-layer theory and hydrodynamic stability need to be understood. This thesis cannot review all relevant information found in excellent textbooks specialized on these topics, e.g. [90, 91]. Nevertheless, the following paragraphs provide a concise overview of important aspects and mathematical formulations to facilitate the understanding of the computational methodology delineated in Chapter 3.5.

The basic equations to describe the dynamics of Newtonian fluids are the continuity equation and the Navier-Stokes equations. In their general form, these equations are elliptical and do not provide closed analytical solutions. Therefore, simplifications are necessary in order to obtain solutions for specific problems. For sufficiently low fluid velocities, the assumption of incompressibility (ρ = const.) is valid and reduces the complexity of the equations. In vectorial notation those equations read

$$\nabla \cdot \vec{u} = 0 \tag{2.1}$$

$$\rho \left(\frac{\partial \vec{u}}{\partial t} + \vec{u} \cdot \nabla \vec{u} \right) = -\nabla p + \mu \nabla^2 \vec{u} + \vec{f} \tag{2.2}$$

comprising the velocity vector $\vec{u}$, the scalar pressure p, the dynamic viscosity $\mu = \nu\rho$, and the force vector $\vec{f}$. The full three-dimensional formulation is required to derive the stability equations in Chapter 2.2, whereas the boundary-layer flow will subsequently be treated two-dimensionally.

2.1 Boundary-Layer Theory

Prandtl [82] introduced the concept of boundary layers, suggesting that viscosity only dominates the flow close to the surface of an immersed body. In this region, special assumptions apply to the incompressible continuity

equation (2.1) and the Navier-Stokes equations (2.2). For simple geometries like flat plates with straight leading edges or infinitely spanned wings, the flow over the body can be approximated to be two-dimensional. The relevant dimensions are then the streamwise coordinate x and the wall-normal coordinate y, and the velocity vector is composed of the corresponding components $\vec{u} = [u, v]^T$. For each incompressible flow situation, the Navier-Stokes equations and the continuity equation can be normalized with appropriate reference scales. For boundary-layer flows, these are the freestream velocity $U_{\mathrm{ref}} = U_\infty$ and the chord length $l_{\mathrm{ref}} = c$ of the immersed body.

Several other simplifications are accessible via estimates of the orders of magnitudes of the single terms of (2.1) and (2.2) which can be reviewed in standard fluid mechanics text books, e.g. [90, 102], finally simplifying the set of equations for steady flow to

$$\frac{\partial u}{\partial x} + \frac{\partial v}{\partial y} = 0 \tag{2.3}$$

$$u\frac{\partial u}{\partial x} + v\frac{\partial u}{\partial y} = -\frac{f_x}{\rho} - \frac{1}{\rho}\frac{\mathrm{d}p}{\mathrm{d}x} + \nu\frac{\partial^2 u}{\partial y^2} \tag{2.4}$$

$$\frac{\mathrm{d}p}{\mathrm{d}y} = 0. \tag{2.5}$$

It should be noted that wall-normal body forces f_y are neglected whereas wall-tangential forces f_x remain in the governing equations, which is valid and of importance for the inclusion of DBD forcing discussed in Chapter 3.5.2. The obtained equations (2.3) - (2.5) describe the physical phenomena within steady two-dimensional boundary-layer flow. A direct implication of (2.5) is the independence of the pressure in wall-normal direction such that the pressure distribution is imposed from outside the boundary layer. Viscous effects vanish at the edge of the boundary layer such that the flow-field evolution $U_e(x)$ can be calculated by potential-flow solvers. With this quantity known, the relation

$$-\frac{1}{\rho}\frac{\mathrm{d}p}{\mathrm{d}x} = U_e\frac{\mathrm{d}U_e}{\mathrm{d}x}, \tag{2.6}$$

reduces the number of variables from four (u, v, p, f_x) to only three (u, v, f_x). Furthermore, the elliptical nature of the Navier-Stokes equations vanishes in favor of a parabolic set of equations. Hence, no upstream influences are considered which simplifies the solution of the equations dramatically.

The boundary conditions at the solid surface and in the undisturbed outer flow read

$$\begin{aligned} y = 0: &\qquad u = v = 0 \\ y \to \infty: &\qquad u = U_e(x). \end{aligned} \tag{2.7}$$

This simplified set of equations can be solved with numerical tools as described in Chapter 3.5.1. The Reynolds number

$$Re = \frac{U_{\mathrm{ref}}\, l_{\mathrm{ref}}}{\nu} \tag{2.8}$$

defines the ratio between inertial and viscous forces within the flow at a speed of U_{ref}, l_{ref} being a characteristic length scale and ν the kinematic viscosity. For sufficiently low Reynolds numbers, viscous forces attenuate any fluctuations within the laminar flow. Beyond a certain Reynolds number Re_{crit}, the initially laminar boundary-layer flow becomes susceptible to naturally present disturbances. By amplification of such instabilities, the flow approaches a turbulent state of chaotic fluid motion. This process is called transition and has been extensively studied experimentally and numerically for boundary layers. If the characteristic reference length l_{ref} is replaced by the distance x which the flow has traveled since impinging on the solid surface and the mean flow velocity U_∞ is employed, the local Reynolds number

$$Re_x = \frac{U_\infty\, x}{\nu} \tag{2.9}$$

is obtained. It then becomes clear that the transition process takes place over a certain streamwise range and divides the domain into a laminar and a turbulent portion. For a low disturbance environment in two-dimensional flow under moderate pressure gradients, the initial stage of this process is dominated by two-dimensional instabilities called Tollmien-Schlichting waves. The amplification or attenuation of such disturbances poses a stability problem which can be assessed by linear stability theory (compare Chapter 2.2). Subsequent amplification of oblique wave modes and nonlinear interactions with the 2D-waves form secondary instabilities. These three-dimensional structures amplify rapidly and give rise to the formation of turbulent spots. The initially two-dimensional instabilities thus initiate the breakdown to fully turbulent motion within the boundary layer beyond the transition Reynolds number Re_{trans}.

The wall-normal extent of the boundary layer defines the region where viscosity is of interest. Since the asymptotic convergence of the flow velocity

towards the outer flow inhibits a clear analytical definition of the boundary-layer thickness, integral quantities are employed to describe the boundary layer. One of these is the displacement thickness δ_1 which accounts for the displacement of streamlines of the outer flow

$$\delta_1 = \int_0^\infty \left(1 - \frac{u}{U_e}\right) \mathrm{d}y. \tag{2.10}$$

If the displacement thickness is known and treated as an additional thickness on top of the limits of the immersed body, the outer flow field can be treated inviscidly. In combination with potential-flow solvers, this enables an iterative solution of the full flow field and the boundary-layer equations (2.3) - (2.5). Apart from the displacement thickness δ_1, another important integral boundary-layer quantity is the momentum thickness δ_2 defined as

$$\delta_2 = \int_0^\infty \left[\frac{u}{U_e}\left(1 - \frac{u}{U_e}\right)\right] \mathrm{d}y. \tag{2.11}$$

The quantity accounts for the momentum loss due to the viscous forces and is of interest concerning the momentum transfer due to DBD operation. The displacement thickness as well as the overall wall-normal extent of the laminar boundary layer typically grow along the flow direction and show even larger growth after transition to the turbulent state. In conjunction with the momentum loss thickness, this behavior will be used for transition indication as described in Chapter 3.3.1. Due to the increased momentum exchange and mixing within the turbulent boundary layer, the velocity distribution close to the wall deviates clearly from the laminar flow state. Different velocity profiles are included in Figure 2.1, illustrating the difference in the wall-normal velocity gradient at the wall (subscript w indicating $y = 0$). The friction along the surface

$$\tau_\mathrm{w} = \mu \left(\frac{\partial u}{\partial y}\right)_\mathrm{w} \tag{2.12}$$

is dominated by this gradient, which is higher for turbulent flow as compared to laminar one. Therefore it is desirable to maintain the laminar flow state as long as possible. Active flow control, as reported later within this work, can be employed to accomplish this objective.

The wall-normal velocity gradients at the wall are also of importance for the flow stability and the resistance against flow separation. The streamwise momentum equation (2.13) is derived from (2.2) for a two-dimensional flow case, normalized and considered at the wall.

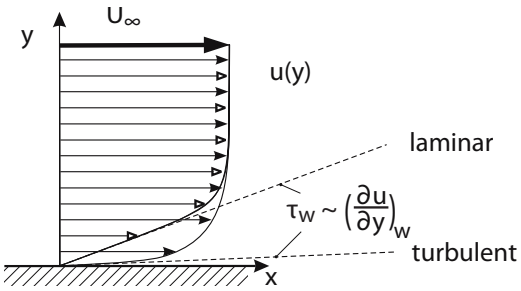

Figure 2.1: Laminar and turbulent boundary-layer profiles.

$$\rho_{\mathrm{w}}\Bigg(\underbrace{\left.\frac{\partial u}{\partial t}\right|_{\mathrm{w}}}_{1}+\underbrace{u_{\mathrm{w}}\left.\frac{\partial u}{\partial x}\right|_{\mathrm{w}}}_{2}+\underbrace{v_{\mathrm{w}}\left.\frac{\partial u}{\partial y}\right|_{\mathrm{w}}}_{3}\Bigg)+\underbrace{\left.\frac{\partial p}{\partial x}\right|_{\mathrm{w}}}_{4}-\underbrace{f_{\mathrm{w}}}_{5}-\underbrace{\mu_{\mathrm{w}}\left.\frac{\partial^2 u}{\partial x^2}\right|_{\mathrm{w}}}_{6}=\mu_{\mathrm{w}}\left.\frac{\partial^2 u}{\partial y^2}\right|_{\mathrm{w}} \tag{2.13}$$

Gad-el-Hak [39] shows that the second derivative of the streamwise velocity with respect to the wall-normal direction on the right hand side dictates the stability properties and the resistance to flow separation. The so-called stability modifiers on the left hand side of the equation include the following mechanisms and may have stabilizing or destabilizing effects, depending on the sign and direction:

- wall motion: terms 1, 2 and 3
- wall transpiration: term 3
- pressure gradients: term 4
- body forces: term 5
- wall curvature: term 6
- viscosity gradients: term 6 & right hand side

The stability of boundary layers can be enhanced by ensuring a fuller velocity profile, i.e. negative profile curvature. In gaseous media this can be achieved by compliant wall movement, wall suction, negative pressure gradients or streamwise body force fields as well as cooling to modify the viscosity at the wall. The linear superposition of any of these methods enables a combination of passive and active flow-control approaches. Within this work, the modification of the stability properties due to dielectric barrier discharge force fields will be investigated under various pressure gradients.

The theoretical background for the stability considerations investigated numerically and experimentally will be provided in the following section.

2.2 Linear Stability Theory

The evolution of small two-dimensional waves inside a laminar boundary layer can be regarded as a stability problem. Stability signifies that the flow returns to the initial state after a specified perturbation. Accordingly, boundary-layer instabilities will lead to a state change of the laminar flow towards turbulent conditions. Linear stability theory provides an approach to investigate under which conditions a certain disturbance will exhibit stable or unstable behavior. Due to a necessary linearization of the problem around the basic laminar state, only the initial stages of the developing instabilities can be predicted.

Following the approach chosen by Schmid and Henningson [91], the governing equations of the linearized stability problem are derived. Most of the concepts of linear stability presented hereafter also apply to other flows (Kelvin-Helmholtz instabilities, Rayleigh-Bernard convection), but the following derivation is focussed on boundary-layer flows without further consideration of generalized problems. Equations (2.1) and (2.2) govern the mean-flow dynamics but also the behavior of the disturbances inside the flow. To describe the beginning disturbance motion inside the boundary layer, the full three-dimensional equations are necessary. They are normalized with the freestream velocity U_∞ and the displacement thickness δ_1 as defined in equation (2.10).

Since the equations for a disturbance evolution inside the mean flow are to be derived, the flow is decomposed into a mean state (capitalized characters) and a disturbed state (small characters with primes),

$$\vec{u} = \vec{U} + \vec{u}' \tag{2.14a}$$

$$p = P + p'. \tag{2.14b}$$

Inserting the decomposition into (2.1) and (2.2) and taking into account that the mean flow necessarily fulfills the continuity and Navier-Stokes equations (2.2), leads to the non-linear disturbance equation

$$\frac{\partial \vec{u}'}{\partial t} + \vec{u}' \cdot \nabla \vec{U} + \vec{U} \cdot \nabla \vec{u}' = -\nabla p' + \frac{1}{Re} \nabla^2 \vec{u}' - \vec{u}' \cdot \nabla \vec{u}'. \tag{2.15}$$

For boundary layers, a first but strong simplification is to consider the base flow to be wall-parallel. A streamwise unidirectional flow with a velocity gradient in the wall-normal direction y

$$\vec{U} = [U(y), 0, 0]^T \tag{2.16}$$

is assumed and introduced into (2.15). These simplifications facilitate the derivation of the stability equations for a local approach. If the amplitudes of the disturbances $\vec{u}' = [u', v', w']^T$ and p' are sufficiently small (usually a threshold of approx. $1\,\% U_\infty$ is assumed for the velocity fluctuation amplitudes), non-linear interactions can be neglected. The continuity equation and the disturbance equations are simplified to

$$\frac{\partial u'}{\partial x} + \frac{\partial v'}{\partial y} + \frac{\partial w'}{\partial z} = 0 \tag{2.17}$$

and

$$v'\frac{\partial U}{\partial y} + \frac{\partial u'}{\partial t} + U\frac{\partial u'}{\partial x} = -\frac{\partial p'}{\partial x} + \frac{1}{Re}\nabla^2 u' \tag{2.18a}$$

$$\frac{\partial v'}{\partial t} + U\frac{\partial v'}{\partial x} = -\frac{\partial p'}{\partial y} + \frac{1}{Re}\nabla^2 v' \tag{2.18b}$$

$$\frac{\partial w'}{\partial t} + U\frac{\partial w'}{\partial x} = -\frac{\partial p'}{\partial z} + \frac{1}{Re}\nabla^2 w' \tag{2.18c}$$

in component notation. The boundary conditions (2.7) are also transformed into the disturbance boundary conditions

$$\begin{aligned} y = 0: &\qquad u' = v' = w' = 0 \\ y \to \infty: &\qquad u' = v' = w' = 0. \end{aligned} \tag{2.19}$$

Stability theory considers the growth or decay of disturbances inside the boundary-layer flow. Since their correct form is generally unknown, the modal approach assumes a combination of wavelike disturbances. Each partial disturbance is a designated mode and may be considered as a traveling wave along the surface in the x-z-plane. The initial growth of the small wavelike disturbances can be described by an exponential ansatz

$$q'(x, y, z, t) = \hat{q}(y) e^{i(\alpha x + \beta z - \omega t)} \tag{2.20}$$

with the shape function

$$\hat{q} = (\hat{u}, \hat{v}, \hat{w}, \hat{p})^T \tag{2.21}$$

where ω is the angular frequency and α and β represent the chordwise and spanwise wavenumbers.

The wavenumbers or the frequency are either complex or real values, dependent on whether the temporal or the spatial problem is considered. If the temporal evolution of a certain disturbance defined by the real wavenumber α or β is of interest, the angular frequency $\omega = \omega_r + i\omega_i$ is a complex quantity. The real part then describes the temporal frequency whereas the imaginary part determines if the disturbance is exponentially amplified or damped, compare (2.20). Positive imaginary parts ω_i provoke exponential growth of the disturbance whereas negative values indicate a decay of this mode. Contrarily, if the spatial evolution of a temporally periodic disturbance (ω is real) is considered, the imaginary part of the wavenumber α or β defines the growth or attenuation of the mode. A negative value leads to growing amplitudes whereas positive values indicate stable conditions. In the following, the spatial approach is chosen to consider the convective evolution of wavelike perturbations which grow spatially in proportion to $\vec{u}' \propto e^{-\alpha_i x + \beta_i z}$. Here, the convective speed of a single wave is defined by the phase velocity c_r which is the real part of the quantity $c = \omega/\alpha = c_r + ic_i$. If a single disturbance frequency is considered, the (complex) wavenumber α influences the phase velocity of the wave and vice versa. This will be of relevance for the results presented in Chapter 4.2.

For a given frequency ω and a provided range of the local Reynolds number Re_x, the disturbance equations (2.18) in combination with the boundary conditions (2.19) pose an eigenvalue problem for the wavenumbers α and β. The procedure to solve this problem is discussed in Chapter 3.5.3. For a purely two-dimensional disturbance without spanwise modulation ($\beta = 0$), the problem is reduced to the analysis of the imaginary part of α, named the spatial growth rate. Since the eigenvalue problem yields a large number of eigenvalues, the most prominent one influencing the stability of the flow has to be identified. The obtained eigenvalues can be displayed in the complex plane as exemplarily illustrated in Figure 2.2 (a) for a simple 2D-flow over an airfoil. Eigenvalues with negative real parts are not physical, just like the so-called continuous spectrum forming a Y-shaped structure. The relevant mode obtained for the indicated setting is found on the right side of the figure and is marked with a red circle. It is the so-called Tollmien-Schlichting mode which is initially stable (positive growth rates α_i) but turns unstable during the downstream evolution, illustrated by the red crosses including negative values. Eventually, the mode returns to sta-

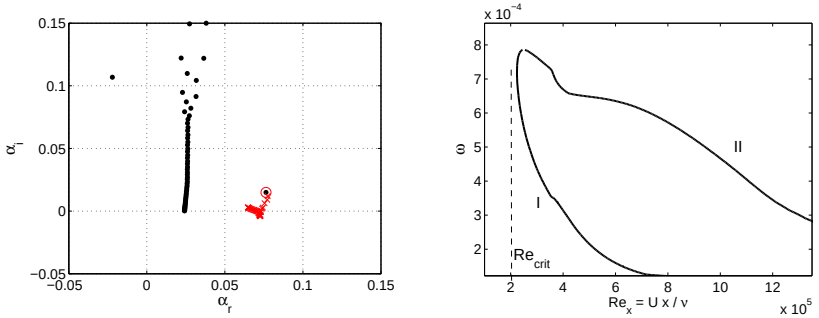

(a) complex plane (b) neutral stability curve

Figure 2.2: Eigenvalues in the complex plane (a) and the neutral stability curve plus N-factor evolution for combinations of Reynolds number Re and disturbance frequencies ω (b).

ble conditions such that three phases during the downstream propagation can be identified. First, the mode is damped until reaching a critical point where the excitation of the mode is initiated. The disturbance amplitude increases up to a certain position from which on the disturbance is damped again. If the disturbance frequency $f \propto \omega$ is systematically varied, this behavior can be illustrated in form of the so-called neutral stability curve. This tongue-shaped solid line in Figure 2.2 (b) encloses the region of disturbance amplification. The curve indicates the indifference of the spatial growth rate, i.e. $\alpha_i = 0$. The aforementioned differentiation into three regions of stability for a distinct frequency is represented by branch I and II of the curve. This depiction immediately reveals to which disturbance frequencies the flow will be sensitive at a given Reynolds number. It also shows the critical Reynolds number Re_{crit}, namely the Reynolds-number for which a first amplification of disturbances is found.

Generally speaking, a negative velocity profile curvature as discussed in Section 2.1 increases the critical Reynolds number and decreases the growth rates of modal disturbances, accordingly enhancing the flow stability. Integration of the growth rates α_i along the streamwise dimension x yields the non-dimensional N-factor [108]

$$N = \ln \frac{A}{A_0} = \int_{x_{\mathrm{crit}}}^{x} -\alpha_i \mathrm{d}x \tag{2.22}$$

It is proportional to the logarithm of the ratio between the disturbance amplitude A at a streamwise position x and the initial amplitude A_0 at the neutral point x_{crit}. Based on this parameter, empirical correlations enable an estimation of the approximate transition location for low-disturbance environments ($Tu < 1\%$) with Tollmien-Schlichting wave domination. The N-factor will be utilized in Chapter 5 to evaluate the impact of DBD flow control on the stability of laminar boundary-layer flow. Although the N-factor method is not based on actual disturbance amplitudes but on disturbance amplification rates, results of stability computations may serve as a guide to evaluate experimental transition measurements [85]. This technique is comprehensively reviewed by Arnal [5, pp. 105-158] and compared to other empirical-based approaches.

3 Methodology

Detailed information on the experimental and numerical approaches to answer the key questions elaborated in Chapter 1.3 are provided in the following. First, the dielectric barrier discharge plasma actuator and the necessary equipment is introduced. Different flow quantities are reviewed which enable experimental observation of the boundary-layer state. To investigate the impact of DBD actuators on natural boundary-layer transition and to evaluate the effect of actuator placement on the flow-control effectiveness, a generic flat plate setup is employed in a small scale wind tunnel. The experimental details of these investigations are provided, followed by the introduction of the experimental setup for more sophisticated flight experiments. Finally, the computational routines for the numerical analysis of the boundary-layer flow under control of DBD actuators are presented.

3.1 Dielectric Barrier Discharges

To investigate the flow-control effect of a DBD plasma actuator on laminar boundary-layer flow, the working principle of the device needs to be understood. The principal setup of a dielectric barrier discharge actuator is illustrated in Figure 3.1. DBD actuators consist of two electrodes separated by a dielectric, non-conducting material. The material constituting the dielectric barrier may be chosen arbitrarily, but high dielectric strengths are desirable to achieve a maximized electric potential. Since the actuator needs to be implemented into the surface to avoid disturbances

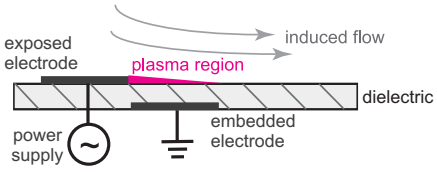

Figure 3.1: Sketch of DBD actuator setup for boundary-layer flow control.

like roughness or surface imperfections, it is typically aimed for a low total thickness of the actuator. One of the electrodes is exposed to the flow whereas the other one is embedded under the dielectric, both consisting of highly conducting material to decrease the resistance and thermal dissipation. The electrodes are usually applied in an asymmetric configuration to achieve a directed flow-control effect. If the potential difference between the two electrodes is increased and surpasses a certain breakdown voltage, a surface discharge occurs and ionization of fluid molecules in the immediate proximity of the exposed electrode is observed, generating a weakly ionized plasma. The breakdown voltage is mainly determined by the geometry and spacing between the electrodes and defined through the dielectric material and thickness. Ionized particles are accelerated in the directed electric field and transfer momentum to neutral air molecules by particle collisions. This momentum transfer may be regarded as a volume force field imposed on the surrounding fluid. The discharge is limited by saturation of the charge deposition on the dielectric barrier, such that sinusoidal supply voltages are generated for a repetitive force generation. During both half cycles of the alternating potential, different ions are created and involved in the force production. It has not finally been agreed within the community whether the force is directed in the same direction throughout the whole cycle [14, 65, 101]. Forte et al. [34] measured a temporal unsteadiness of the force production throughout the voltage cycle. For aerodynamic applications, the relevant time scales are orders of magnitudes larger than the discharge physics scales. To identify the impact on the averaged flow field surrounding the DBD actuator, only the obtained quasi-steady net force in one direction is of relevance. Supply voltage frequencies in the Kilohertz range provide a sufficiently high net force per time and ensure that modal flow receptivity to unsteady force production can be neglected.

For the experiments reported in this thesis, copper tape of 35 μm thickness constitutes the exposed and embedded electrodes at a width of 2.5 mm and 10 mm, respectively. The principal sketch in Figure 3.1 illustrates the abutted placement of the electrodes in the horizontal direction. In the vertical dimension between the electrodes, five layers of *Kapton* tape with a total thickness of $d = 300\,\mu$m provide the dielectric barrier. The actuator length in the third dimension depends on the desired application and ranges from $0.44 - 0.6$ m in the reported experiments whereas supply voltages $V_{pp} = 9$ kV and 13 kV peak-to-peak are chosen dependent on the desired force magnitude. Although several different power supplies for sinusoidal wave generation are available, a *GBS Elektronik MiniPuls 2.1* is

selected for all reported experiments. This power supply is implementable into the flight setup due to its small dimensions of 160 mm × 300 mm and weight below 1 kg. An additional advantage is a $0 - 5$ V input channel to control the high voltage output between $V_{pp} = 0 - 20$ kV, sufficient for all employed DBD configurations. The possibility to control the output based on an analog signal is of relevance for the closed-loop performance control presented in Chapter 6.2.2. The use of one power supply for all experiments reduces the number of parameters, although the resonance frequency may change depending on the actuator length. For each setup, the resonance frequency is chosen to obtain a maximum electrical efficiency and a robust high frequency generation. Despite the alternating polarity and associated unsteadiness of the body force production, the resonant frequencies $f_{pl} \geq 6$ kHz are well beyond the receptivity limit of the boundary-layer flows investigated. Stability analysis presented in Chapter 5 shows that all disturbances in the high frequency range are effectively damped and do not influence the transition process.

Kriegseis et al. [62] investigated the force distribution created by an equally composed DBD actuator. For sufficiently long electrodes, the force generation and fluid acceleration can be regarded to take place in a two-dimensional plane. In quiescent air, the actuator creates a laminar jet tangential to the wall directed from the exposed electrode along the embedded electrode. This wall jet scales with similarity laws formulated by Glauert [41] and can be characterized by its thickness and maximum induced velocity. Above the exposed electrode, a suction region replenishes the fluid volume and exhibits a small wall-normal force component. Particle image velocimetry (PIV) provides the velocity field induced by the discharge and solving the Navier-Stokes equations for the body force reveals the spatial force distribution in the vicinity of the electrodes as proposed by Wilke [116]. The analysis reveals that the main force is directed in wall-tangential direction and the wall-normal force component is one order of magnitude lower [58]. Figure 3.2 illustrates the spatial distribution of both components. The wall-tangential force exhibits a distinctive peak approximately 1 mm downstream of the exposed electrode, indicating the region of maximum fluid acceleration. A parasitic force region close to the wall downstream of $x = 2$ mm illustrates self-induced, wall-friction drag leading to a decay of the total force magnitude by approximately 30%, which is in agreement with observations by Enloe et al. [29]. A large portion of the induced force is dissipated by wall-shear stress and small-scale turbulence close to the wall. The original force f and the residual thrust T need to be

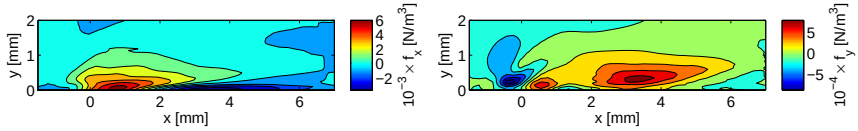

(a) $10^{-3} \times f_x$ (b) $10^{-4} \times f_y$

Figure 3.2: Wall-tangential (f_x) and wall-normal (f_y) force distribution at $V_{pp} = 10$kV, data from [58].

distinguished. Considering the net thrust T obtained by a single DBD, the integral values range between 5 mN and 25 mN per meter actuator length and are validated by force balance measurements. It is obvious that the thrust production cannot be monitored during flow-control experiments due to the sensible balance equipment. This requires another measurable variable to relate to the flow-control authority expressed by the net thrust.

Kriegseis et al. [59] describe a correlation between thrust measurements and the power consumption P of DBD actuators. Both quantities are employed to define the flow-control effectiveness $\eta' = T/P$ as a first approach to quantify the performance of DBD actuators for flow-control applications. Though, it should be emphasized that only a small portion of the consumed energy is transformed into fluidic kinetic energy. The majority is spent on dissipative heating of the electric circuit. The power consumption is determined by the applied voltage and the dielectric material. It can be measured by integration of the actuator charge Q over the periodic voltage V_{pp} during one cycle as introduced by Manley [71]. The charge Q can be measured by using a monitor capacitance between the embedded electrode and electrical ground as first employed by Pons et al. [80]. The Lissajous plot, which illustrates the consumed power by the area enclosed between the curves for charge over voltage, is shown in Figure 3.3 for a peak-to-peak voltage amplitude of $V_{pp} = 10$ kV. In this configuration, the actuator consumes $P = 45.9$ W per meter actuator length, which is representative for the presented actuator configuration. Since actuators of varying length are employed in this work, the net power consumption is always related to the actuator length to facilitate a comparison. The electrical measurements are conducted with a *Tektronics TDS 3032C* oscilloscope or a *Picotech PicoScope 4424* USB-based data-acquisition device. Details on the power measurements employing the same actuator configuration as in the present work are provided by Kriegseis et al. [60]. For a unique actuator config-

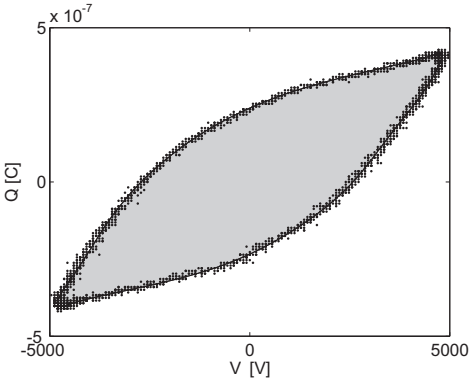

Figure 3.3: Lissajous figure of actuator charge Q vs. voltage V.

uration, the power consumption P is related to the thrust production T by a monotonic dependence. The relation between both values can be approximated by a linear function even for different operating frequencies in [59], allowing a direct conversion between the two parameters if the electrical setup of the actuator is kept constant. Since an identical actuator composed of five layers of *Kapton* and the same electrode material is used in the present study, this analogy is exploited to relate the actuator thrust to the easily measurable power consumption.

Other quantities have been proposed to quantify the fluid mechanic impact of DBD actuator. The ratio between the maximum flow velocity induced by an actuator in quiescent air and the freestream flow velocity is commonly used [40, 70]. However, the maximum wall-jet velocity in quiescent air alone does not sufficiently characterize the integral impact of the additional momentum. Hence, it is emphasized that the integral actuator thrust is a more relevant quantity for characterization of the flow-control impact. Since the consumed actuator power can be measured instantaneously during any flow-control experiment, an experimental correlation to the produced thrust is recommended and needs to be investigated for every particular actuator configuration. For the experiments described in the following chapters, the corresponding integral thrust and power consumption are indicated to put the actuator impact into context.

Several restrictions and limiting factors apply to the flow control by DBD actuation. The force magnitudes are limited by the maximum potential

difference endured by the dielectric material. Additionally, recent investigations [61, 70] report a deterioration of the DBD performance due to increasing flow velocities. Bénard et al. [10, 11] discuss the impact of surrounding pressure and humidity on the DBD power consumption and force magnitude. For varying ambient conditions (e.g. atmospheric variations during flight), it is a prerequisite for systematic experiments to provide a constant flow-control forcing. Hence, a closed-loop control method for constant force production is necessary and developed in Chapter 6.2.2.

3.2 Transition Detection

In order to determine the state of the boundary layer and track the transition process, several methods can be employed. For comparison of different data sets and correct quantification of a possible transition delay by DBD actuation, unambiguous and reliable criteria are necessary. The following section provides an overview of the most common methods which will be utilized throughout the present investigations on various experimental setups.

Statistical measures of time-resolved boundary-layer data are commonly employed for analysis of the transition process. The semi-deterministic nature of the transition process provokes a broadband increase of the spectral content, complicates repeatability and sets high demands on experimental accuracy [106, pp. 886 - 896]. Amplified Tollmien-Schlichting waves and turbulent breakdown lead to an increasing standard deviation σ of velocities inside the boundary layer or pressure on the wall. The so-called flow intermittency region contains randomly occurring turbulent spots (or Emmons spots) such that the flow undergoes a stochastic state change between laminar and turbulent. The position of this region is mainly governed by the relation between the transitional and local Reynolds numbers. It becomes accessible by varying the local Reynolds number Re_x in a range around the transition Reynolds number Re_{trans}, either by varying the flow speed U or the measurement location x. Both approaches have specific advantages, but in case of a velocity-dependent pressure gradient of the flow, a variation of the probe position should be favored over velocity variations.

If sufficiently long velocity or pressure measurements across the intermittency region are conducted, a characteristic evolution of the signal standard deviation is obtained. The lines in Figure 3.4 (a) illustrate the standard deviation $\sigma_U = U_{rms}$ of a hot wire placed at $y/\sqrt{x\nu/U_\infty} = 2.2$ normalized

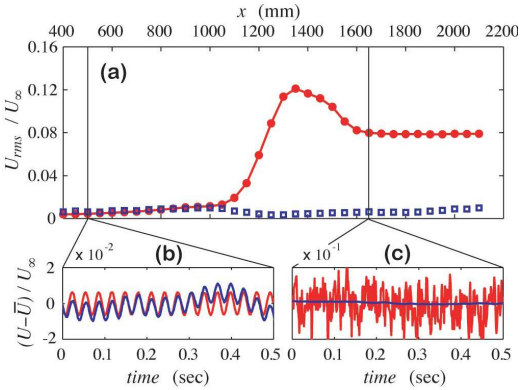

Figure 3.4: Characteristic evolution of signal standard deviation (a) during transition along a flat plate. The lower plots illustrate the time signal in the laminar (b) and fully turbulent (c) flow region. Circles without flow control, squares with roughness elements, from [37].

with the freestream velocity U_∞ along a flat plate measured by Fransson et al. [37]. The transition evolution under excited disturbance conditions is illustrated by the circled line. In the laminar region upstream of $x \approx 1'000\,\text{mm}$, only small deterministic velocity fluctuations (b) are present limiting the standard deviation. As the disturbances grow and the flow temporally starts to experience turbulent spots, a steep increase of the standard deviation is observed. With increasing temporal percentage of the turbulent content, the signal approaches an apex around $x = 1350\,\text{mm}$. Beyond this characteristic peak, the turbulent state starts to dominate and the standard deviation decreases until settling at a constant level for fully turbulent flow (c). Although the illustrated experiments were conducted with artificially excited disturbances, the same trend can be seen during natural transition. The standard deviation of a measurement signal directly at the wall can also be used, e.g. from static pressure measurements at high temporal resolution or hot-film experiments [77]. Arnal and Archambaud [6] provide a review of several transition control experiments based on such standard deviation measurements.

The squares in Figure 3.4 (a) illustrate the behavior with flow control by means of specially arranged roughness elements, totally mitigating the

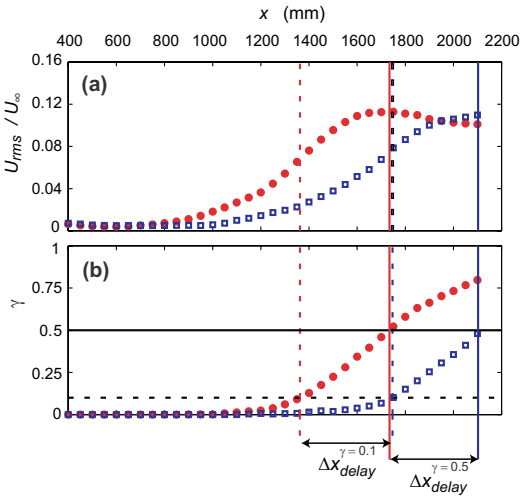

Figure 3.5: Use of signal standard deviation (a) and intermittency factor (b) for quantification of the transition delay obtained by laminar flow control. Circles without, squares with roughness elements, from [37].

transition process over the observed streamwise range. For transition control experiments in boundary layers, the signal standard deviation σ is the most frequently chosen value to quantify the obtained effect on the transition location. Its main advantages are the freedom of choice of the sensor type and no necessity to calibrate the sensor, as well as the possibility to measure either at the wall or inside the flow. To ensure reliable data, the measurements need to be sufficiently long for statistical certainty and the temporal resolution high enough to capture all relevant turbulence scales. Figure 3.5 illustrates additional measurements by Fransson et al. [37] to delay natural transition by means of roughness elements. The displacement of the standard deviation peak for two measurements is used to quantify the transition delay $\Delta x_{\mathrm{delay}}$ in 3.5 (a). Circles again illustrate the case without flow control whereas the controlled conditions are presented by squares.

Additionally, the intermittency factor γ is illustrated (b) which quantifies the temporal ratio between laminar and turbulent state of the boundary layer. A balanced ratio of $\gamma = 0.5$ indicates equal distribution of laminar and turbulent flow during a measurement, and the streamwise position

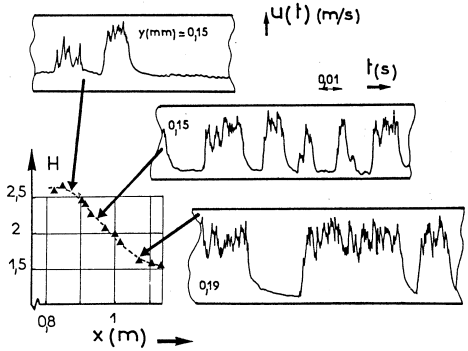

Figure 3.6: The shape factor during transition related to intermittent hot-wire signals, from [7].

where it is found coincides with the position of maximum standard deviation in (a). The unambiguous intermittency value ranges between 0 and 1 in contrast to the standard deviation, which does not have a clearly defined absolute maximum value even if normalized with the freestream velocity U_∞. The main disadvantage is the existence of various definitions for γ, all based on empirical calibration constants. Three of the most commonly used definitions, including the TERA and M-TERA methods, are reviewed by Zhang et al. [119] and a strong dependence on the calibration constants is observed. Especially if different experimental setups are to be compared, a universal specification of these constants is difficult. The necessity to measure velocities inside the boundary layer inhibits the calculation of intermittency factors from wall-mounted sensor data.

If velocity data across the whole boundary layer is acquired, the integral properties of the velocity field are accessible. The shape of the profiles characterizes the state of the flow and can be represented by the shape factor $H_{12} = \delta_1/\delta_2$. The ratio between two integral quantities, the displacement thickness δ_1 and the momentum loss thickness δ_2 defined in equations (2.10) and (2.11), is a measure of the momentum distribution across the boundary layer. Knowing that the shape factor is closely related to the stability properties of the flow, e.g. the critical Reynolds number as shown by Wazzan et al. [112], it provides an indication of the hydrodynamic stability. Laminar profiles experience strong shape changes due to external pressure gradients such that the shape factor spans in a broad

range, $H_{12} \approx 2.3 - 3.9$. During transition the profiles become 'fuller' and the displacement thickness is locally decreased whereas the momentum loss thickness grows monotonically. The shape factor H_{12} shows a steep and characteristic decrease until settling at $H_{12} = 1.4$ for fully turbulent flow [90]. Figure 3.6 reports the shape factor and hot wire measurement signals throughout the transition region. The monotonic evolution of the shape factor observed by Arnal et al. [7] without any characteristic peaks aggravates the exact quantification of the transition process. Nevertheless, it delivers valuable information based on the whole flow profile as compared to statistical data analysis at the wall. Within the laminar flow domain, the pressure gradient and some stability properties may additionally be estimated from available shape factor evolutions. Since knowledge of the exact wall position is crucial for accurate calculation of the displacement thickness δ_1, a high spatial resolution of the velocity data with high statistical significance is required, rendering measurements time consuming and difficult.

All above mentioned methods have been employed to analyze transitional boundary-layer data on the different experimental setups reported in the following.

3.3 Flat Plate Experiments

In order to enhance the understanding of DBD flow control imposed on transitional boundary layers, controllable and well-defined flow conditions are necessary. Although lacking relevance for practical application, generic flat plate setups have proven valuable to foster the understanding of fundamental physical processes. Grundmann [43] showed the applicability of DBD actuators for transition delay on a flat plate at flow velocities below 8 m/s and under controlled disturbance conditions. The current project aims to increase the Reynolds number range at which DBD actuators can be applied successfully for delaying transition and to demonstrate their effectiveness in a naturally occurring transition scenario. The easily accessible experimental data on the generic setup enables a parametric study of different actuator configurations. Additionally, a numerical analysis of the flat plate setup is straightforward and facilitates a validation and optimization of the flow-control application.

The transition experiments reported in Chapter 4 are conducted in an open-circuit wind tunnel with a 1 : 24 contraction nozzle. The 450 mm $\times$ 450 mm test section contains a flat plate of 1600 mm length with an 1 : 6

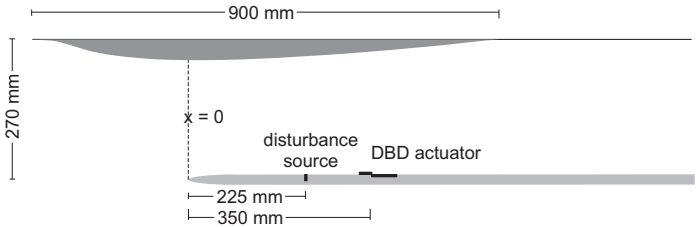

Figure 3.7: Displacement body and flat plate in test section, including flush-mounted DBD actuator and disturbance source. Maximum contraction located at leading edge ($x = 0$).

elliptical leading edge and inclinable trailing-edge flap for adjustment of the stagnation point. The flat plate provides an insert centered 350 mm downstream of the leading edge to flush mount single DBD actuators of 440 mm spanwise length. Since transition would naturally occur far downstream in the test section for the projected freestream velocity $U_\infty = 20\,\mathrm{m/s}$, a displacement body is installed on the tunnel ceiling to destabilize the laminar boundary-layer flow. The maximum thickness of the displacement body is located at the beginning of the flat plate ($x = 0$) as illustrated in Figure 3.7, creating an adverse pressure gradient downstream of the leading edge. At $U_\infty = 20\,\mathrm{m/s}$, an average turbulence intensity of $Tu = 0.24\%$ is measured at the inlet of the test section. This intensity, comparable to values found by Weismüller [114] at elevated turbulence in flight, renders the flow quality acceptable for transition measurements. A disturbance source is installed 225 mm downstream of the leading edge. It consists of a spanwise array of 12 miniature loudspeakers driving a flush-mounted brass bar. By harmonic excitation with an amplified signal, a wall-normal displacement of the brass bar induces deterministic disturbances inside the boundary-layer flow. The disturbance source enables defined disturbance conditions and experimental stability investigations. Although the focus of the work is the delay of naturally developing transition without external excitation, controlled disturbance conditions are valuable for the analysis of the interaction between the flow-control device and a single modal disturbance, as delineated in Chapter 4.2.

Various measurement techniques are utilized to quantify the transition process and acquire data in close proximity of the force generating high-voltage electrodes. Since each measurement principle offers different advantages, the potentially best-suited strategy is chosen to answer a variety

of questions as explained in the following.

3.3.1 Hot-Wire Measurements

Under conditions of low freestream turbulence and in the absence of acoustic disturbances or surface roughness, the boundary-layer transition along the flat plate is expected to be triggered by two-dimensional Tollmien-Schlichting waves. The linear amplification process of these modal disturbances is governed by the stability of the boundary layer which is accessible via stability analysis as described in Chapter 3.5.3. The later stages of transition are characterized by the breakdown of the Tollmien-Schlichting waves into three-dimensional, chaotic structures and increasing velocity fluctuations inside the boundary layer.

Hot-wire anemometry allows the acquisition of time-resolved velocity information to resolve all relevant disturbance frequencies in the presented experiment. Throughout this work, all hot-wire measurements are conducted in a constant temperature anemometer (CTA) setting at sampling frequencies of 16 kHz. In the wind-tunnel experiments, a *DISA 55M01* hot-wire anemometry Wheatstone bridge is used to measure flow velocities and fluctuations along the flat plate. A *Dantec 55P15* type single-wire boundary-layer probe mounted on a *Dantec 55H21* probe support can be traversed via an *Velmex BiSlide* 2-axis automated system and is calibrated with a reference *Schildknecht MiniAir6 Micro* vane anemometer. Data is sampled via a *National Instruments USB-6259* analog-digital converter and a *DISA 55D26* analog signal conditioner provides a low-pass filter with a cutoff at 3.15 kHz. This cutoff frequency removes electromagnetic noise caused by the dielectric barrier discharge and enables determination of disturbance frequencies in the expected flow instability range. A spectral analysis of the velocity data enables identification of the critical disturbance frequencies and a quantification of disturbance amplitudes. Measurements at different streamwise positions or variation of the flow velocity lead to a variation of the signal standard deviation σ_U and can provide an intermittency factor γ as described in Section 3.2. Hot-wire anemometry additionally enables the acquisition of averaged velocity profiles within the boundary layer as illustrated in Figure 2.1. The shape factor may be calculated to identify the influence of the pressure gradient and to track the transitional behavior of the full velocity field. Both techniques are employed in Chapter 4.1 to evaluate the impact of DBD actuation on the transition process on the flat plate.

Since the technique is highly sensitive to changing ambient temperature, the fluid temperature T_a is monitored during the measurements and a temperature compensation according to Lemonis and Dracos [64]

$$E_{corr} = E_{meas}\sqrt{\frac{T_W - T_{a0}}{T_W - T_a}} \tag{3.1}$$

is applied. The measured hot-wire voltage E_{meas} is transformed into the corrected value E_{corr} by relating the hot wire operation temperature T_W to the ambient flow temperature during the hot-wire calibration T_{a0} and the actual flow temperature T_a during the measurement. The correction is applied before conversion to the calibrated velocity U_{CTA} according to King's law [74]

$$E_{corr} = \sqrt{A + BU_{\mathrm{CTA}}^n}. \tag{3.2}$$

The calibration factors A, B and n can be obtained by least-squares regression of multipoint reference data.

Hot-wire anemometry is advantageous for continuous data acquisition at high temporal resolution, beneficial for a statistical analysis. The actuator effect in the immediate proximity of the exposed electrode cannot be assessed. The alternating, high electric potential induces disturbance currents within the wire and poses the risk of arcing, eventually destroying the probe and the Wheatstone bridge. Only non-intrusive methods are capable of measuring fluid properties directly at the exposed electrode without either disturbing the flow field or damaging the sensor. Optical measurement techniques are predestined to quantify the interaction of the plasma with the flow close to the high voltage electrodes (e.g. [23, 26, 34, 51, 81]). Two optical measurement techniques are introduced in the following to characterize the flow closer than 20 mm to the zone of ionization.

3.3.2 Particle Image Velocimetry

The mean flow field and the impact of DBD operation can be characterized using a *Dantec Nano-S* $2D-2C$ particle image velocimetry system similar to the setup used by Duchmann et al. [23]. A *Dantec FlowSense 2M* CCD camera with 1600×1200 pixel resolution and equipped with an *AF Mikro Nikkor* 105 mm $f = 2.0$ lens is positioned outside of the test section. The imaging plane is parallel to the x-y-plane of the test setup and adjusted to a field of view of 32 mm $\times$ 24 mm in the center of the test section. A Nd:YAG *Litron* dual-cavity laser with a *Dantec 80X70* light-sheet optic

provides a maximum power output of 135 mJ per cavity to illuminate the DEHS-seeded wind-tunnel test section. The repetition rate of the laser pulses is limited to 15 Hz. In order to reduce background light reflections a monochromatic filter at the laser wavelength of $\lambda = 532$ nm is installed on the lens. 10 bit images are acquired in double-frame mode and for the correlation of the velocity vectors, an interrogation area size of 16×16 pixels with an overlap of 50% is chosen. The main advantage of the PIV measurement is the acquisition of the whole flow field within the camera field of view. Nevertheless, a large number of PIV images needs to be averaged to obtain a reliable velocity field, rendering the measurement time consuming and difficult for varying flow conditions.

The current work employs a phase-locked approach to measure boundary-layer instabilities and their interaction with a DBD force field via particle image velocimetry. Widmann et al. [115] introduce a method to measure the spatial distribution and evolution of artificially excited Tollmien-Schlichting instabilities in laminar boundary layers and present details on the experimental apparatus. The application of this method for the evaluation of disturbance damping by arbitrary flow-control actuators has been suggested in the outlook and is realized for DBD actuation in the present work. In the context of flow stability, it is helpful to investigate the DBD flow-control effect on modal instabilities which eventually trigger transition. Both the streamwise and the wall-normal velocity component of deterministic modal disturbances are accessible via triggered particle image velocimetry.

In order to ensure repetitive boundary-layer disturbances of fixed frequency and amplitude, the disturbance source implemented at $x = 225$ mm creates a two-dimensional convective disturbance. The disturbance source on the flat plate is energized with a sinusoidal reference signal, creating a single frequency boundary-layer instability. A delay generator is employed to trigger the PIV data acquisition - by adjusting the time delay between the reference signal and the data acquisition, arbitrary phase-relations Φ to the disturbance signal can be chosen. By repetitive phase measurements and ensemble averaging, the deterministic flow disturbance dominates over random velocity fluctuations and measurement errors. The accuracy of the velocity quantification can be correlated to the standard deviation which is a function of the ensemble size. For increasing sample numbers, the standard deviation asymptotically converges towards a fixed value. An ensemble of 1700 velocity fields is found to provide a good compromise between measurement accuracy and duration for the conducted experiments.

An equidistant spacing of $\Delta\Phi = 30°$ is chosen to resolve the disturbance period by twelve different phases Φ. The raw data are cross-correlated with *Dantec Dynamic Studio* and processed further using *MATLAB*. The single vector fields undergo a range validation to eliminate spurious values due to lack of seeding material, reflections and variations of the freestream velocity. For clarity, the vector fields are decomposed into a streamwise component u and the wall-normal component v. The postprocessing is exemplarily explained for the streamwise component but applies in the same way to the wall-normal direction. One averaged two-dimensional velocity field $\overline{u}_\Phi$ is calculated for each phase Φ. Averaging over all twelve $\overline{u}_\Phi$ eliminates the influence of the disturbances and yields the mean velocity field of the boundary layer $\hat{u}$ which would be found without disturbance excitation. The mean velocity field is finally subtracted from each $\overline{u}_\Phi$ to yield periodic flow fluctuations $u'_\Phi = \overline{u}_\Phi - \hat{u}$. The results acquired with the described method have been published in [26] and are recapitulated in Chapter 4.2. The observations are helpful to understand the interaction between flow disturbances and the DBD device in direct vicinity of the force generation.

3.3.3 Laser Doppler Anemometry

Alternatively, laser Doppler anemometry (LDA) provides both the streamwise and wall-normal velocity component in a point-like measurement volume of approximately 0.2 mm diameter and 1 mm length. A *Dantec Flow Explorer* 35 mW laser head emits two laser beam wavelengths and creates a interferometric measurement volume at a focal distance of 300 mm. DEHS particles seed the flow and provide the backscatter signal which is post-processed with the *BSA Flow Software*. In combination with an *ISEL* 3-axis traverse system the measurement volume can be positioned anywhere inside the wind-tunnel test section. The LDA setup measures velocity profiles close to the DBD electrodes and enables a comparison of the boundary layer's momentum content with and without flow control. The wall-normal resolution is not limited by camera resolution or interrogation area size as in the case of the PIV setup. Therefore, high-precision velocity profile measurements with wall-normal spacings of 0.1 mm are available and shown in Chapter 4.3. Such measurements complement the hot-wire measurements further away from the actuator and enable a stability analysis reported in Chapter 5.4. Since such stability analysis only requires averaged velocity information, no phase-locking or disturbance excitation are necessary during the LDA measurements.

3.4 Flight Setup

In the preceding chapter, the advantages of a generic flat plate setup to systematically investigate certain aspects of DBD flow control have been elaborated. Nevertheless, the application of such actuators under realistic conditions for a net gain is desirable and aimed at within the presented project. One promising task is the prolongation of laminar flow along an airfoil to reduce its friction drag. Initial success has been achieved by Séraudie et al. [97] showing a measurable transition delay on the ONERA-D airfoil at low Reynolds numbers ($U_\infty < 17\,\mathrm{m/s}$ and chord length $c = 0.35\,\mathrm{m}$). At chord Reynolds numbers of approximately $Re = 4 \times 10^5$, a transition delay of up to 35% of the chord length is reported.

The imparted momentum due to the DBD forcing is limited and needs to be considered in relation to the freestream momentum. Therefore, DBD flow control at low Reynolds numbers is more effective than for the range above $Re > 1 \times 10^6$ which is of interest for human flight. Apart from the necessary increase of chord length and flow velocity to obtain sufficiently high Reynolds number, the ambient conditions during flight are of eminent importance. Changing humidity affects the DBD performance whereas incoming turbulence and the absolute value of the pressure gradient along the airfoil dictate the transition behavior of the boundary layer. In order to evaluate the limits of DBD flow control in the Reynolds number regime of interest, an airborne flight setup on a double seated motorized glider is presented. The realistic combination of all relevant parameters cannot be provided in any wind-tunnel setting and therefore, flight tests are required. Nevertheless, initial wind-tunnel tests of the flight setup reduce the necessary installation and testing period due to simplified accessability. The flight equipment was therefore designed such that it can alternatively be applied on the wing of a full scale G109b motorized glider or within the large-scale NWK wind tunnel. Details on the wind tunnel are provided in Chapter 6.1 whereas the flight setup including the motorized glider are introduced in the following sections.

3.4.1 Glider

A double-seated G109b motorized glider by *Grob Aircraft* is employed to investigate the effect of DBD actuation on boundary-layer transition under free-flight conditions. The aircraft combines the advantages of vibrationless gliding flight with a 96 kW engine for autonomous take-off and effective altitude gain. The *Limbach 2400 DT1* turbo-charged motor can be

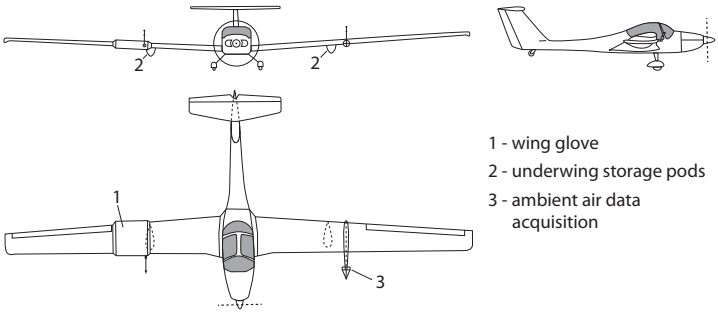

Figure 3.8: Flight setup including G109b glider and measurement equipment.

powered down and the *Hoffmann* propeller rotated into a gliding position for minimum vibrational, electromagnetic and acoustic disturbances during transition experiments. The wing and fuselage of the aircraft are composed of glass and carbon fibre reinforced plastics yielding an empty gross weight of 660 kg. The trapezoidal wing with a span of 17.4 m and aspect ratio of 15.9 comprises the E580 natural laminar flow airfoil designed by Eppler with subtle forward sweep. With a taper ratio of 0.55, the sweep angle at the leading edge is almost zero, minimizing spanwise pressure gradients and creating almost two-dimensional flow along the chord such that amplified Tollmien-Schlichting waves are expected to dominate the transition process. Several modifications of the airframe structure as well as non-permanent adjustments are necessary and certified by the German Federal Aviation Authority (LBA) in order to implement measurement equipment and host a laminar wing glove which is in detail discussed in Section 3.4.2. Details of the airframe modifications for flight investigations are presented by Erb [30] and Weismüller [114]. Non-permanent modifications with valid LBA certification include a vibration-isolated platform to host data acquisition equipment in the rear part of the cockpit [117], a sting-mounted wind vane with adjacent storage pod for ambient condition monitoring on the port wing and a NLF wing glove mounted on the starboard wing. To account for the additional payload, a temporary "permit to fly" is issued by the LBA to allow a maximum take-off weight of $m_{MTOW} = 950\,\text{kg}$. Under regulations of this permit to fly with increased weight, the maximum flight

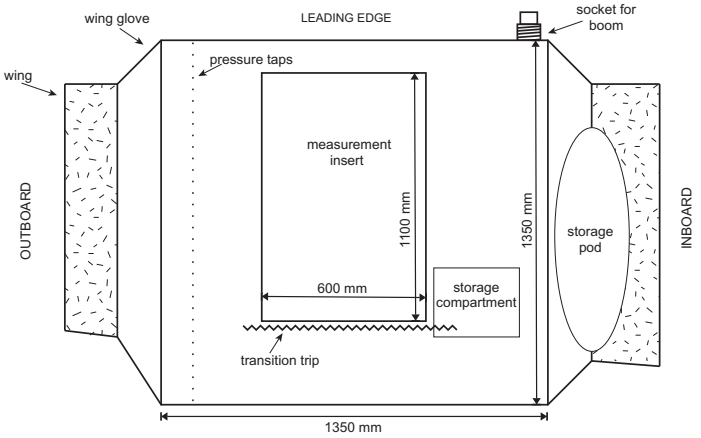

Figure 3.9: Bottom view of wing glove dimensions fixed on the glider wing.

speed is limited to $U_{max} = 44.5\,\mathrm{m/s}$. The lower end of the flight envelope is marked by stall speed with retracted air brakes at $U_{min} = 20.3\,\mathrm{m/s}$. Since for steady flight conditions the necessary lift is governed by the aircraft mass and glide angle, the angle of attack α has to be chosen accordingly. The angle of attack exploitable for the experiments range between $-3°$ close to the speed limit and $\sim 13°$ just before complete flow separation. The Approved Flight Manual [57] and the Type Certificate Data Sheet [67] provide additional data and limits of operation for the motorized glider. The measurement system including the plane, the wing glove and the ambient condition acquisition is illustrated in Figure 3.8. Details of the measurement equipment are presented in the following.

3.4.2 Wing Glove

To quantify the influence of atmospheric turbulence on natural laminar flow airfoils, Weismüller [114] developed a wing glove for assembly on the right glider wing. Such a wing glove slides over the outer section of the tapered wing and matches smoothly at one defined spanwise position as illustrated in Figure 3.9. The wing glove enables implementation of arbitrary sensors without interfering with the airframe structure. Similar experiments have been conducted [30, 94, 95] to measure the laminar-turbulent transition process along a wing glove with hot-film anemometry. Since the wing glove

slides over the wing and exhibits higher chord and thickness, it is specially designed to match the lift and drag of the covered wing section. This is a necessity to retain the same flight characteristics with or without the asymmetric equipment installed. A custom designed airfoil based on the Althaus AH93-157 with 5% higher thickness and 25% increased camber in combination with a steeper trailing edge angle was selected and forms a rectangular section of 1.35 m × 1.35 m. The characteristics of the pressure side of this airfoil predestines it for flow-control investigations since the pressure gradient is almost linear and adjustable between moderate positive and negative values, expanding the region of possible transition locations. The flow over the wing glove was numerically investigated by Schulze [93] and shown to be largely two-dimensional, except for the lateral tapered regions connecting the wing glove to the glider wing. In the center portion, where an exchangeable measurement insert made from acrylic glas accommodates a streamwise row of microphones described in detail in Section 3.4.4, the boundary layer does not show crossflow velocity components. A laminar separation bubble on the pressure side detected by Weismüller [114] downstream of $x/c = 0.8$ would lead to a considerable drag increase. To avoid an influence of the separation bubble on the sensor readings, a transition trip is installed at $x/c = 0.78$. On the inboard side of the leading edge, a connection socket enables installation of a front boom for hot wire and pressure measurements of the incoming flow. An underwing pod and a storage compartment for equipment complete the wing glove.

3.4.3 Exchangeable Insert

The exchangeable measurement inserts of 600 mm width and 1100 mm length cover the central region of the pressure and suction side of the wing glove. To ensure surface smoothness and minimize streamwise and spanwise waviness, the inserts are made from cast plexiglas of 2 mm thickness. They are connected to the wing glove via *3M* adhesive tape for non-destructive removal and to avoid temperature induced stress. Such loads could be a consequence of different thermal expansion coefficients as the glove surface is heated by the sun. The inserts can be replaced for different measurement tasks and sensor-actuator configurations. For the evaluation of DBD-based boundary-layer transition control, the insert holds a disturbance source, a single DBD actuator and wall-mounted sensors for transition detection.

A spanwise row of 20 miniature loudspeakers is implemented at $x/c = 0.17$ on the pressure side and at $x/c = 0.18$ on the suction side to excite

disturbances in the laminar portion of the boundary layer, artificially triggering the transition to turbulence. Such investigations are described in Chapter 6.3 and enable a comprehensive analysis of the stability characteristics of the wing glove under flight conditions. The amplification of discrete frequencies can be evaluated and compared to numerical computations of the transition process or stability analysis as discussed in Chapter 5.

A single DBD actuator is placed at $x/c = 0.33$ on the pressure side, providing a body force in streamwise direction to influence the laminar boundary-layer flow. The geometric configuration is defined in Section 3.1 and the actuator spans the whole width of the measurement insert in spanwise direction, namely 600 mm. A sinusoidal high voltage is applied via a *MiniPuls 2.1* generator installed in the storage compartment. The resonant frequency of this combination of actuator and high voltage generator is $f_{pl} = 7.8\,\text{kHz}$ and applied for all flight experiments. The thrust and power consumptions during each flow-control experiment are referenced in the corresponding Chapter 6.3.

Downstream of the DBD actuator, a streamwise array of microphones is implemented to quantify the transition location and disturbance frequencies. More details on the sensors are provided in the following.

3.4.4 Sensors

The wing glove is designed for boundary-layer measurements and to quantitatively compare the transition process under the influence of DBD operation to the case without flow control. For such a task, adequate sensors have to be selected. Optical measurement techniques are non-intrusive and not influenced by electromagnetic disturbances in the proximity of the high-voltage ionization region, but they cannot be easily implemented in the non-stationary and spatially confined flight setup. Horstmann and Miley [49] used surface-mounted hot-wire probes to detect Tollmien-Schlichting waves. The most significant disadvantage of such an approach is the disturbance of the flow downstream of the probe position such that the spatial evolution of disturbances cannot be tracked. Since the desired information of the boundary-layer state is available from the wall-near region of the flow, surface implemented sensors can be chosen to characterize the flow state around the wing glove.

Along the outboard portion of the wing glove, 64 pressure taps are distributed over the suction and pressure side of the wing glove. The pressure taps have an opening diameter of 0.2 mm and are drilled perpendicularly into the carbon-fibre reinforced surface, connecting to underlying, airtight

brass pipes. A *Pressure Systems ESP-64HD* differential pressure scanner is connected by 1.2 m long flexible PVC tubes enabling static pressure measurements. The pressure distribution along the wing glove facilitates comparison of the experiments to numerical investigations and determination of the correct angle of attack. The necessary tube lengths and the small orifice restrict the resolvable frequencies of pressure variations. Sinclair and Robins [100] provide a formula based on assumed laminar pipe flow to estimate the time the pressure information requires to travel through the tubes. For the given setup, the temporal resolution is limited to less than 10 Hz, which impedes quantification of the transition process through the pressure readings.

Wall-integrated microphones have been proposed by Nitsche and Brunn [74] for transition detection. In the past, various in-flight transition experiments have been successfully performed with either flush-mounted microphones or highly sensitive pressure transducers [32]. On the center portion of the pressure-side measurement insert, a streamwise row of 15 *Sennheiser KE 4-211-2* microphones is installed 2 mm underneath the surface. The microphones are evenly distributed with 30 mm spacing between $x/c = 0.36$ and $x/c = 0.67$ and the signals are conducted to a self-built amplifier. The connection to the flow is provided by one small orifice of 0.2 mm diameter for each microphone. The maximum resolvable frequency $f_{\max} \approx 8\,\text{kHz}$ is limited by the inertia of the air volume contained inside the orifice, but since the relevant flow instabilities inside the boundary layer are expected not to exceed 2 kHz, the chosen setup is appropriate to track the streamwise development of transition in flight. For a complete calibration of the microphone array, the frequency response of each microphone needs to be known, requiring an acoustic laboratory. A simplified approach is selected and justified by the similarity of the frequency responses of structurally identical microphones. On ground, a loudspeaker is situated in sufficient distance to the wing glove to create a quasi two-dimensional acoustic wave front with a white noise frequency distribution. A *ROGA Instruments RG-50* reference microphone is installed at the same distance to the sound source. The root-mean-square (RMS) values of the microphone output voltages are related to the calibrated reference microphone sensing a sound pressure level $L_p = 20 \log_{10} \frac{p_{\text{rms}}}{p_{\text{ref}}}$ in dB. The reference pressure $p_{\text{ref}} = 20\,\mu Pa$ is used and the sensitivity of the sensors is evaluated based on the reference microphone signal. The sensitivity of the single microphones varies between 6.78 and 1.55 mV/Pa, and therefore requires a calibration coefficient s_i for every microphone to be determined, in order to compensate for similar output

levels for the various sensors. The calibration factor for the first microphone within the array is $s_1 = 57.03\,\mathrm{dB/V}$. Henceforth the logarithmic scale is applied for all microphone signals. During the flight-measurement campaign, artificial triggering of transition upstream of the first microphone position provides a quasi-white noise signal. The turbulent boundary layer contains multi-frequent disturbances of invariant intensity and allows for a checkup of the obtained calibration factors.

Weismüller [114] installed two booms in front of the wing glove leading edge to enable pressure and hotwire measurements of the incoming flow. A negative impact on the two-dimensionality of the flow was observed at high angles of attack. The flow separating on the protruding structure induces turbulence on the wing glove flow, especially in the case of large additional side slip angles β. In contrast to the reported experiments, only one boom is installed in the present study. The problematic angles of attack are well beyond the interesting angles, such that these effects are neglected. A pitot and static pressure probe on the boom enables measurements of the flight speed. Both pressures are digitized with the differential pressure scanner described above. The maximum allowable pressure difference of this scanner is 24.8 hPa enabling the resolution of dynamic pressures and pressure distributions across the full flight envelope. The front boom can additionally accommodate a X-shaped hot-wire probe for acquisition of the flow speed U_{CTA} and angle of attack α_{CTA}. Due to hardware problems with sensor crosstalk the corresponding data will not be discussed in this thesis.

Boundary-layer velocity profiles can be acquired with a *Dantec 55P15* type hot-wire probe mounted to a 3D-traverse system described in more detail in Section 3.4.6. All hot-wire sensors are connected to a multichannel constant temperature anemometer system based on *Dantec MiniCTA* bridges contained inside the underwing storage pod. The hot-wire equipment is calibrated to the expected flight speed via King's law and a temperature correction is applied as described in Section 3.3.1. The circuit-integrated analog filter is set to 3.15 kHz. Although higher frequencies can be resolved, this filter is chosen to avoid aliasing and minimize disturbing effects due to high-frequency DBD operation. An overall sketch of the pressure side of the wing glove instrumented with the different sensors is provided in Figure 3.10.

Microphone and hot-wire data are acquired via a modular *National Instruments 9074 cRIO* real-time system equipped with 4 analog-digital converters of the type *NI 9205*. All flow measurements are acquired with a sampling rate of 16 kHz to resolve the DBD operating frequency and avoid

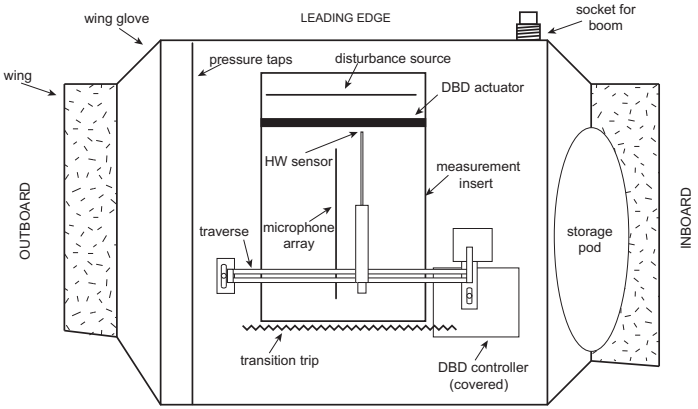

Figure 3.10: Overview of the wing glove pressure side with sensors and traverse system installed.

aliasing effects. Additional flow temperature measurements are digitized with a *NI 9211* module and a *NI 9263* module enables the generation of analog output signals. The latter is relevant for closed-loop controlled DBD operation as described in Chapter 6.2. Due to the large amount of data streamed during measurements, a binary file format is chosen in the *LabView* based acquisition software. The copilot foot compartment contains a 24 V battery providing the power for all measurement equipment and the high-voltage generator, ensuring independence from the aircraft power system for 2 hours of measurement operation. All sensors are selected to unambiguously track the transition process on the wing glove and ensure repeatability of the experiments. Since no severe post processing is necessary for the chosen measurement methods, online evaluation of the data in flight is available. This facilitates the appropriate reproduction of flight states during the measurements since the momentary ambient conditions are known.

3.4.5 Ambient Air Data Acquisition

The environmental conditions during flight are measured on the left wing with a system introduced by Erb [30] and Weismüller [114]. *Setra 270 & 239* absolute and differential pressure sensors are employed to acquire the static and total pressure on static and pitot tubes at an additional

boom, mounted upstream of the left wing. The ambient air temperature is measured with a *PT1000* temperature sensor neglecting the influence of empirical recovery factors for the conversion between static and total temperature. A humidity sensor is installed to determine the current air density and to calculate the correct Reynolds number and true airspeed U_{TAS}. A *Dornier Flight Log*, which is a wind vane following the incident flow, is mounted on the boom and provides the angle of attack α as well as the sideslip angle β. A GPS receiver installed on the suction side of the left wing provides the longitudinal and latitudinal position as well as altitude information. All ambient data are sampled with 16 bit at a frequency of 10 Hz with a *National Instruments USB-6221* AD converter and transferred to the measurement platform in the baggage compartment within the cockpit. The calibration functions and correction factors for all air data measurement equipment can be reviewed in [114].

3.4.6 Boundary-Layer Traverse

Boundary-layer measurements along the wing-glove surface are crucial to determine the state of the transitional boundary layer and measure the shape and amplitudes of contained disturbances. In order to acquire time-resolved velocity data along the exchangeable plexiglas measurement insert, a light-weight three-axis traversing system was developed which can be installed on either side of the wing glove. A sketch of the traversing system is provided in Figure 3.11 (a), indicating the single components with different colors. Two turrets (grey) are connected to variable mounting threads along the glove chord to both sides of the measurement insert. Both turret heads provide coaxial pivot points on which a linear traversing assembly for the spanwise direction (blue) is supported. On the moving sledge of this linear traverse, another linear traverse (green) is mounted enabling streamwise movement of a hot-wire probe support. The set of linear traverses may be rotated around the pivot point by a stepper motor positioned next to the inboard turret (red), leading to a wall-normal displacement of the hot-wire support with respect to the glove surface. The wall-normal positioning accuracy of the hot-wire probe is 0.1 mm for highly resolved boundary-layer profiles. The lateral dimensions can be approached with approximately 1 mm accuracy. *NanoTech* stepper motors with feedback encoders ensure repeatability of the probe positioning.

Due to the convex nature of the wing glove and especially the non-monotonous curvature on the pressure side, the traverse kinematic illustrated in Figure 3.11 (b) has to account for non-linear movements by ad-

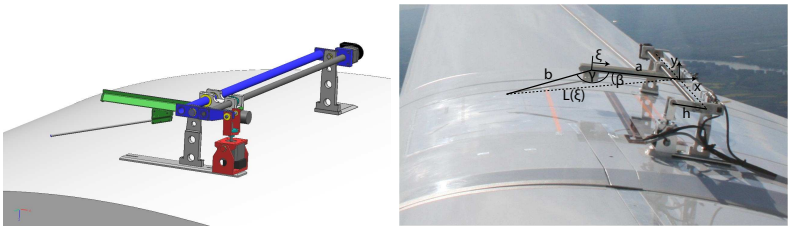

(a) Sketch of single traverse components for application on pressure side.

(b) Kinematic of the traverse system on the suction side during flight.

Figure 3.11: Sketch (a) and kinematic (b) of the traverse system for boundary-layer measurements on the wing glove.

equate software programming and stepper motor control. Small modifications of the hardware and sign changes within the relative coordinate systems are necessary when switching between pressure and suction side installation. The software is implemented in *LabView* and allows for user-controlled single movements as well as automated positioning according to predefined schemes. The combination of linear and rotatory components creates a non-linear kinematic with mutual dependence of the positions of each stepper motor, requiring the definition of an absolute reference position. In order to calculate the next probe motion in wall-normal and streamwise direction, the actual probe location in relation to the absolute reference needs to be known. The curved surface contour is defined by three reference positions and cubic spline interpolation within the streamwise range of the traverse. Detailed information on the kinematics and the software implementation are provided by Simon [99]. The in-flight transition measurements on the NLF wing glove performed with this traverse will be presented in Chapter 6.3.

3.5 Numerical Tools

In contrast to experimental investigations with associated measurement uncertainties and limited spatial resolution of sensors, computational studies offer a detailed glance on any desired fluid property. A numerical treatment of the problem enables a detailed analysis of the flow-control mechanisms and exact repeatability for parametrical studies – if the problem is described appropriately by the underlying equations and with the proper

boundary conditions. Several assumptions and simplifications are usually necessary to enable a numeric treatment of fluid mechanic problems. The boundary-layer and stability equations derived in Chapter 2.1 require adequate discretization and implementation into a computing environment.

3.5.1 Boundary-Layer Solver

For the evaluation of flow-control strategies and the effect on boundary-layer stability, the boundary-layer velocity distribution needs to be known. It can either be obtained by experimental measurements as described in Section 3.3 or by a numerical solution of the governing equations derived in Chapter 2.1. Simplified solutions exist to compute the evolution of integral boundary-layer quantities like the displacement thickness δ_1 or the shape factor H_{12}, e.g. the Thwaites [19] or Pohlhausen [79] methods. For a numerical treatment of flow-control effects, this is not sufficient and the full boundary-layer information including velocity gradients and curvature need to be accessible. The boundary-layer problem (2.3) - (2.7) consists of partial differential equations for which no general analytical solution is available. Only for certain simplifications and conditions, analytical treatments (e.g. for the zero pressure-gradient Blasius flow) are applicable. For a numerical solution of the problem, several transformations are necessary which are discussed hereafter.

The solver numerically approximates the partial differential boundary-layer equations by finite differences based on a transformation of the physical domain. Since the boundary-layer thickness increases during the downstream development, the wall-normal coordinate y is conveniently normalized with dependence on the physical downstream coordinate x. A normalized wall-normal coordinate η is obtained by employing the so-called Falkner-Skan transformation introducing the Blasius length scale δ_N,

$$\eta = y/\delta_N = y\sqrt{Re\frac{U_e(x)}{x}}. \tag{3.3}$$

With this transformation, the wall-normal coordinate is stretched to preserve a similar order of magnitude in the streamwise direction. Hence, the size of the computational grid cells can be maintained along the downstream direction x without a loss of precision. Applying this transformation to (2.4) and employing (2.6), the streamwise momentum equation reads

$$u\left(\frac{\partial u}{\partial \eta}\frac{\partial \eta}{\partial x}+\frac{\partial u}{\partial x}\right)+v\frac{\partial u}{\partial \eta}\frac{\partial \eta}{\partial y}=f_x+U_e\frac{\partial U_e}{\partial x}+\frac{1}{Re}\frac{\partial^2 u}{\partial \eta^2}\frac{\partial^2 \eta}{\partial y^2}. \tag{3.4}$$

The boundary-conditions (2.7) remain valid in the transformed form

$$\begin{aligned} \eta = 0: &\qquad u = v = 0 \\ \eta \to \infty: &\qquad u = U_e(x) \end{aligned} \tag{3.5}$$

and the partial derivatives with respect to the normalized coordinate η are

$$\begin{aligned} \frac{\partial \eta}{\partial x} &= \frac{1}{2}\eta\left(\frac{\partial U_e/\partial x}{U_e} - \frac{1}{x}\right) \\ \frac{\partial \eta}{\partial y} &= \sqrt{Re\frac{U_e}{x}}. \end{aligned} \tag{3.6}$$

The necessary input for the computations is the velocity field at the outer limit of the boundary layer $U_e(x)$. Equation (2.6) enables the calculation of this quantity from a known pressure distribution which can be obtained from potential flow solutions or measurements. Once the pressure distribution is known, the stagnation point of the flow needs to be identified. The measured or computed pressure distribution generally does not cover the exact stagnation point, because of which the maximum pressure value is linearly extrapolated to approximate the position of the stagnation point as accurately as possible. Directly at this position, no velocity profile for the streamwise direction can be computed, requiring a special treatment to initialize the boundary-layer solver. For the following approach, no body force terms are allowed at the stagnation point. According to Cebeci and Cousteix [19], the problem can be solved by computing the derivative of the boundary-layer equation (2.4) with respect to x. Neglecting force terms at the leading edge, this results in

$$\left(\frac{\partial u}{\partial x}\right)^2 + \underbrace{u}_{=0}\frac{\partial^2 u}{\partial x^2} + \frac{\partial v}{\partial x}\underbrace{\frac{\partial u}{\partial y}}_{=0} + v\frac{\partial}{\partial y}\frac{\partial u}{\partial x} = \left(\frac{\partial U_e}{\partial x}\right)^2 + \underbrace{U_e}_{=0}\frac{\partial^2 U_e}{\partial x^2} + \frac{1}{Re_x}\frac{\partial^2}{\partial y^2}\frac{\partial u}{\partial x}.$$

All terms containing the streamwise velocity u and its derivatives in wall-normal direction as well as the edge velocity at the stagnation point vanish, simplifying to

$$\left(\frac{\partial u}{\partial x} + v\frac{\partial}{\partial y} - \frac{1}{Re_x}\frac{\partial^2}{\partial y^2}\right)\frac{\partial u}{\partial x} = \left(\frac{\partial U_e}{\partial x}\right)^2. \tag{3.7}$$

At the stagnation point, η and its derivatives become

$$\eta = y\sqrt{Re\frac{\partial U_e}{\partial x}} \tag{3.8a}$$

$$\frac{\partial \eta}{\partial x} = \frac{1}{2}\eta\frac{\partial^2 U_e/\partial x^2}{\partial U_e/\partial x} \tag{3.8b}$$

$$\frac{\partial \eta}{\partial y} = \sqrt{Re\frac{\partial U_e}{\partial x}}. \tag{3.8c}$$

By inserting (3.8c) into (3.7), adding $(\partial u/\partial x)^2$ on both sides to increase numerical stability and then dividing by $(\partial U_e/\partial x)^2$ it follows

$$\left[2\frac{\frac{\partial u}{\partial x}}{\frac{\partial U_e}{\partial x}} + \frac{v}{\frac{\partial U_e}{\partial x}}\frac{\partial \eta}{\partial y}\frac{\partial}{\partial \eta} - \frac{1}{Re\frac{\partial U_e}{\partial x}}\left(\frac{\partial \eta}{\partial y}\right)^2\frac{\partial^2}{\partial \eta^2}\right]\frac{\frac{\partial u}{\partial x}}{\frac{\partial U_e}{\partial x}} = 1 + \left(\frac{\frac{\partial u}{\partial x}}{\frac{\partial U_e}{\partial x}}\right)^2. \tag{3.9}$$

This equation is solved for $\frac{\partial u}{\partial x}/\frac{\partial U_e}{\partial x}$ with a finite-difference approach delineated in the following. The relevant velocities and derivatives in x- and y-direction to initialize the boundary-layer code are then found by multiplication with $\partial U_e/\partial x$.

For a numerical solution of the problem, the nonlinear partial differential equation (3.4) is discretized by finite differences on a numerical grid. The streamwise discretization is imposed by the experimental pressure data or the potential flow solution, whereas in the wall-normal direction the grid spacing is defined by the necessary resolution of all velocity derivatives. At the wall, these change significantly while approaching constant values in the freestream. For this reason, a non-equidistant grid with finer resolution at the wall is selected by employing the formula [18]

$$\eta_{(j)} = h_1\frac{K^j - 1}{K - 1} \quad \text{for} \quad j = 1, 2, \ldots, J \quad \text{and} \quad K > 1 \tag{3.10}$$

with $h_1 = 0.1$ being the distance of the first grid point from the wall and $K = 1.1$. For laminar flows considered here, $\eta_{max} = 8$ is sufficient to resolve the whole boundary layer whereas in turbulent flows and at higher Reynolds numbers, the transformed boundary-layer thickness would need to be increased. The computational grid is illustrated in Figure 3.12, comparing the grid in physical coordinates y, x (a) and the coordinates transformed via (3.3) to η, x (b). Visible are the enhanced resolution close to the wall as well as the grid-size equality in streamwise direction due to the transformation of the wall-normal variable.

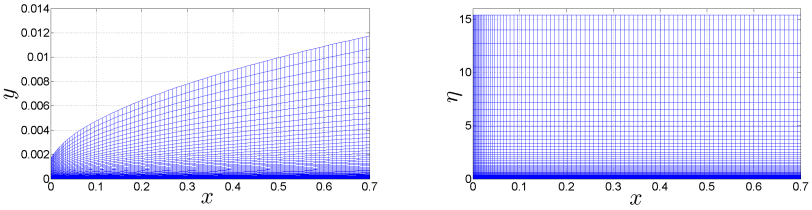

(a) y, x (b) η, x

Figure 3.12: Comparison of the computational grid in physical (a) and transformed (b) coordinates.

Throughout the boundary-layer calculation, several first and second order derivatives in the wall-normal and streamwise direction have to be computed. The use of matrix multiplications is an elegant method to compute these. Exemplarily, the gradient of the edge velocity $U_e(x)$ in the streamwise direction x can be calculated based on finite-differences using a differentiation operator

$$\frac{\partial U_e(x)}{\partial x} = \boldsymbol{D_1} U_e(x) \tag{3.11}$$

where the subscript 1 stands for the first partial derivative in x-direction. To build such a differentiation operator $\boldsymbol{D}$, the derivatives are approximated by truncated Taylor series expansions neglecting terms of third and higher order. A central differencing scheme is applied except for the first and last positions x_1 and x_N where a forward and, respectively, backward scheme need to be applied due to the lack of surrounding data. For the central differencing scheme, the Taylor series expansion centered at the position x_n yields

$$f(x_{n-1}) = f(x_n) + d_{n,1} f'(x_n) + \frac{d_{n,1}^2}{2} f''(x_n) + \mathcal{O}(d_{n,1}^3) \tag{3.12a}$$

$$f(x_{n+1}) = f(x_n) + d_{n,2} f'(x_n) + \frac{d_{n,2}^2}{2} f''(x_n) + \mathcal{O}(d_{n,2}^3) \tag{3.12b}$$

with

$$d_{n,1} = x_{n-1} - x_n \quad \text{and} \quad d_{n,2} = x_{n+1} - x_n. \tag{3.13}$$

Neglecting terms of third or higher order, the system (3.12) can be solved for $f'(x_n)$ and $f''(x_n)$

$$f'(x_n) = -\frac{d_{n,2}}{d_{n,1}\left(d_{n,1}-d_{n,2}\right)} f(x_{n-1}) - \frac{d_{n,1}+d_{n,2}}{d_{n,1}d_{n,2}} f(x_n) + \frac{d_{n,1}}{d_{n,2}\left(d_{n,1}-d_{n,2}\right)} f(x_{n+1}) \tag{3.14a}$$

$$f''(x_n) = \frac{2}{d_{n,1}\left(d_{n,1}-d_{n,2}\right)} f(x_{n-1}) + \frac{2}{d_{n,1}d_{n,2}} f(x_n) - \frac{2}{d_{n,2}\left(d_{n,1}-d_{n,2}\right)} f(x_{n+1}). \tag{3.14b}$$

A matrix representation of these equations for all streamwise positions $x_1 - x_N$ yields the tridiagonal differentiation operators $\boldsymbol{D_1}$ and $\boldsymbol{D_2}$ for the first and second derivatives. Such differentiation operators can be derived for the streamwise as well as the wall-normal direction and all necessary components $D_{i,j}$ are comprehensively reviewed by Köhler [56] based on a formulation from Weideman and Reddy [113].

Once the differentiation operators are formulated to numerically represent the nonlinear partial differential equation (3.4), a streamwise marching procedure is employed. Starting with the initializing solution at the stagnation point, the next possible streamwise position is selected. Since only upstream information is available, a backward differencing scheme is employed for the streamwise marching. The derivatives of the streamwise velocity component in (3.4) are projected on discrete grid positions i and are expressed by

$$\frac{\partial u^{(i)}}{\partial x} = D_{x,n} u^{(n),(i)} + D_{x,n-1} u^{(n-1)} + D_{x,n-2} u^{(n-2)}$$

where the terms $D_{x,n}$ to $D_{x,n-2}$ are the backward derivative terms in x-direction. Sorting already known terms on the right hand side, (3.4) is discretized as

$$\left[D_{x,n} u^{(n),(i)} + \left(u^{(i)} \frac{\partial \eta}{\partial x} + v^{(i)} \frac{\partial \eta}{\partial y} \right) \frac{\partial}{\partial \eta} - \frac{1}{Re} \left(\frac{\partial \eta}{\partial y} \right)^2 \frac{\partial^2}{\partial \eta^2} \right] u^{(i)} = f_x^{(i)} + U_e \frac{\partial U_e}{\partial x} - u^{(i)} \left(D_{x,n-1} u^{(n-1)} + D_{x,n-2} u^{(n-2)} \right). \tag{3.15}$$

The equation can be written in matrix form and the boundary conditions (3.5) are imposed on the first and last rows of the resulting system. The

continuity equation (2.3) is utilized to find the wall-normal velocity component

$$v^{(i)} = v_0^{(n)} + \frac{1}{\frac{\partial \eta}{\partial y}} \int_0^{\eta_{max}} -\frac{\partial u^{(i)}}{\partial \eta}\frac{\partial \eta}{\partial x} - \left(D_{x,n} u^{(n),(i)} + D_{x,n-1} u^{(n-1)} + D_{x,n-2} u^{(n-2)} \right) d\eta \tag{3.16}$$

where $v_0^{(n)}$ is an optional blowing or suction velocity at the wall. An iterative computation of the equations is performed until $\partial u^{(i)}/\partial \eta$ at the first grid point above the wall convergence with a tolerance of 10^{-6}. Once the iteration condition is satisfied, the derivatives of the velocity components are obtained and the calculation starts at the next streamwise position. Since this method cannot deal with separating flows, the calculation is stopped after a maximum iteration count to avoid infinite loops and hence only resolves the attached laminar part of the boundary layer.

3.5.2 Force Model

In order to numerically analyze the flow under influence of DBD actuation and design a flow-control application, a model of the actuator is required. The spatial force distribution described in Section 3.1 is implemented in the boundary-layer solver. For comparison with experiments, the integral value of the model force field needs to be equal to the actuator thrust. Kriegseis et al. [62] experimentally acquired force field distributions at various power consumption levels which enables a numeric treatment of different actuation magnitudes. Until now, no closed formulation of the actuator force as a function of the power consumption is available. Nevertheless, the experimentally chosen force magnitudes (compare Table 4.1) agree with the available force-field data to facilitate a comparison between numerics and experiment. Maden et al. [69] proved the implementability of the force fields for computational fluid dynamics (CFD) simulations by reproducing the wall jet created in quiescent air.

The physical force f_x^* is normalized with the boundary-layer scales

$$f_x = \frac{f_x^*}{\rho^* {l_{\mathrm{ref}}^*}^2} \tag{3.17}$$

and $l_{\mathrm{ref}}^* = \delta_N$ as defined in (3.3) before it can be implemented in the boundary-layer computations. The discretized boundary-layer equation

(3.15) contains a source term $f_x^{(i)}$ for the streamwise force at each grid point. Therefore, the force distribution needs to be discretized on the numerical grid. This is conveniently achieved by a multi-dimensional interpolation routine in *MATLAB*. Since no experience with implementation of force fields in the mentioned boundary-layer code exists, a validation of the computations with experimental data is necessary. The generic flat plate setup introduced in Section 3.3 appears appropriate and the computational results are presented in Chapter 5.2.

3.5.3 Linear Stability Solver

The stability of experimentally (Chapter 4.3) and numerically (Chapter 5) derived velocity profiles is analyzed based on the linear stability theory explained in Chapter 2.2. The aim is to quantify the impact of DBD flow control on the flow stability and anticipate the transition behavior.

Introduction of the disturbance ansatz (2.20) into the equations (2.17) and (2.18a) - (2.18c) results in a set of second-order differential equations

$$i\alpha\hat{u} + \hat{v}_y + i\beta\hat{w} = 0 \tag{3.18a}$$

$$-i\omega\hat{u} + \hat{v}U_y + iU\alpha\hat{u} + i\alpha\hat{p} + \frac{1}{Re}\left(\alpha^2\hat{u} + \beta^2\hat{u} - \hat{u}_{yy}\right) = 0 \tag{3.18b}$$

$$-i\omega\hat{v} + iU\alpha\hat{v} + \hat{p}_y + \frac{1}{Re}\left(\alpha^2\hat{v} + \beta^2\hat{v} - \hat{v}_{yy}\right) = 0 \tag{3.18c}$$

$$-i\omega\hat{w} + iU\alpha\hat{w} + i\beta\hat{p} + \frac{1}{Re}\left(\alpha^2\hat{w} + \beta^2\hat{w} - \hat{w}_{yy}\right) = 0, \tag{3.18d}$$

subscripts indicating differentiation in the corresponding direction. The boundary conditions for this set of equation read

$$\begin{aligned} y = 0: &\qquad \hat{u} = \hat{v} = \hat{w} = 0 \\ y \to \infty: &\qquad \hat{u} = \hat{v} = \hat{w} = 0. \end{aligned} \tag{3.19}$$

The disturbance developments in time (expressed by the angular frequency ω) and space (characterized by the wavenumbers α and β) are physically connected via a dispersion relation of the type

$$D(\alpha, \beta, \omega, Re) = 0 \tag{3.20}$$

for which non-trivial solutions can be obtained via eigenvalue analysis. In general the quantities α, β and ω are complex and two of the three quanti-

ties must be known to enable a numerical treatment of the stability problem. The stability equations (3.18) can be expressed in operator form as

$$\boldsymbol{L}\hat{q} = 0 \tag{3.21}$$

with the linear operator

$$\boldsymbol{L} = \boldsymbol{A} + \boldsymbol{B}\frac{\partial}{\partial y} + \boldsymbol{C}\frac{\partial^2}{\partial y^2} \tag{3.22}$$

and formulation of the disturbance shape function $\hat{q}$ as in (2.21). The matrices $\boldsymbol{A}$ - $\boldsymbol{C}$ are then found to be

$$\boldsymbol{A} = \begin{pmatrix} i\alpha & 0 & i\beta & 0 \\ M & U_y & 0 & i\alpha \\ 0 & M & 0 & 0 \\ 0 & 0 & M & i\beta \end{pmatrix} \tag{3.23a}$$

$$\boldsymbol{B} = \begin{pmatrix} 0 & 1 & 0 & 0 \\ 0 & 0 & 0 & 0 \\ 0 & 0 & 0 & 1 \\ 0 & 0 & 0 & 0 \end{pmatrix} \tag{3.23b}$$

$$\boldsymbol{C} = \begin{pmatrix} 0 & 0 & 0 & 0 \\ -\frac{1}{Re} & 0 & 0 & 0 \\ 0 & -\frac{1}{Re} & 0 & 0 \\ 0 & 0 & -\frac{1}{Re} & 0 \end{pmatrix} \tag{3.23c}$$

where

$$M = i\omega + iU\alpha + \frac{1}{Re}\left(\alpha^2 + \beta^2\right). \tag{3.24}$$

For non-swept wings and TS-wave dominated transition in incompressible flow, Squire [103] proves that two-dimensional perturbations experience larger growth than three-dimensional instabilities and initiate the breakdown to turbulence. For this reason, only two-dimensional disturbances are considered in the framework of this thesis, rendering the spanwise wavenumber β zero. The eigenvalue problem is considered in the spatial framework to obtain the complex streamwise wavenumber $\alpha = \alpha_r + i\alpha_i$ for a predefined disturbance frequency ω.

The homogeneous boundary conditions (3.19) at the solid wall and outside the boundary layer are conserved, posing a boundary-value problem for which no exact analytical solution is available. To enable a numerical solution, a discretization scheme is applied. A spectral Chebyshev collocation

method is chosen to approximate eigensolutions of $\hat{q}$ as accurately as possible. The spectral approach leads to higher accuracy for the small growth rates α_i based on a global approximation of the solution as compared to e.g. finite differences or finite element methods. A further advantage is the reduced number of necessary discretization points and the approximation of derivatives by analytical differentiation of the known basic function. The spectral approach delineated in detail by Schmid and Henningson [91] is adapted to the necessities of the boundary-layer problem.

The dependent variable $\hat{q}$ is represented by truncated sums of first-kind Chebyshev polynomials of the order j,

$$T_j(\xi) = \cos\left(j \arccos(\xi)\right) \tag{3.25}$$

which can be alternatively be calculated by a recurrence relation

$$T_0(\xi) = 1 \tag{3.26a}$$
$$T_1(\xi) = \xi \tag{3.26b}$$
$$T_{j+1}(\xi) = 2\xi T_j(\xi) - T_{j-1}(\xi) \tag{3.26c}$$

on a Gauss-Lobatto grid with N gridpoints defined as

$$\xi_i = \cos\frac{i\pi}{N}. \tag{3.27}$$

This grid enables the discrete presentation of the independent variable y and is selected for its good applicability to spectral procedures. Since the Gauss-Lobatto points are only defined on the finite domain $\xi \in [-1, 1]$ the algebraic function $y(\xi) = \frac{\delta}{2}(1 + \xi)$ maps the grid points into the physical boundary-layer domain $y \in [0, \delta]$.

The Chebyshev representation enables a reformulation of the problem in terms of truncated polynomials (3.25) and differentiation matrices $\mathbb{D}^k$,

$$\hat{q}(\xi) = \sum_{j=0}^{N} p_j T_j(\xi) = \mathbb{D}^0 \vec{p} \tag{3.28}$$

$$\frac{\mathrm{d}^k}{\mathrm{d}\xi^k}\hat{q}(\xi) = \sum_{j=0}^{N} p_j T_j^k(\xi) = \mathbb{D}^k \vec{p}. \tag{3.29}$$

$$\tag{3.30}$$

The derivatives in equation (3.22) are reformulated employing the differentiation matrices $\mathbb{D}^0 - \mathbb{D}^2$ which require the Chebyshev polynomial derivatives to be known. These are again described by a recurrence relation

$$T_0^{(k)}(\xi_i) = 0 \tag{3.31a}$$

$$T_1^{(k)}(\xi_i) = T_0^{(k-1)}(\xi_i) \tag{3.31b}$$

$$T_2^{(k)}(\xi_i) = 4T_1^{(k-1)}(\xi_i) \tag{3.31c}$$

$$T_j^{(k)}(\xi_i) = 2jT_{j-1}^{(k-1)}(\xi_i) + \frac{j}{j-2}T_{j-1}^{(k)}(\xi_i) \tag{3.31d}$$

where the superscript $k \geq 1$ indicates the order of differentiation and $j \geq 3$ the polynomial degree. The differentiation matrices are easily obtained through a *MATLAB* implemented routine according to Weideman and Reddy [113]. The boundary conditions (3.19) are incorporated by setting the lines inside the matrix $\boldsymbol{L}$ (3.21) to zeros which correspond to the freestream and the solid wall. Subsequently, the matrix equations are solved with built-in linear algebra functions. The computational cost is largely defined by the size of the discretization domain. Since ξ is a vector of length $N + 1$, a matrix system of size $(N + 1) \times (N + 1)$ needs to be solved.

The numerical calculation of the eigenvalues α within the spatial framework reveals the amplification or attenuation of disturbances of given frequency ω. If the imaginary part α_i is negative, the disturbance ansatz in equation (2.20) indicates exponential growth of the amplitudes in the streamwise direction. The imaginary part α_i is therefore also referred to as the growth rate of the instability. The growth rate of the most unstable disturbance dictates the transition behavior of the boundary-layer flow. If the amplitude of this modal disturbance has grown large enough, secondary stages of transition are triggered which subsequently induce three-dimensional structures. The simplified equations derived before do not account for such mechanisms which require special treatment beyond the scope of this work.

The downstream evolution of the linear growth rates can be utilized by empirical methods to predict when the fully turbulent state of the boundary layer will be reached. One of such methods is the N-factor method introduced in Chapter 2.2. Since the absolute disturbance amplitude A at a given location x depends on the initial amplitude A_0 as well as the growth rate α_i, the ambient disturbance conditions are to be taken into

account. The initial disturbance conditions, mainly governed by the turbulence intensity Tu of the freestream flow, play a crucial role for the absolute transition location. It is generally agreed that transition is a continuous evolutionary process, nevertheless it will henceforth be assumed that the critical N-factor N_t defines the position of completed transition, resulting in fully turbulent flow. Typical values for N_t in wind tunnels are in the order of $8-9$, depending on the bulk-flow quality. For flight investigations, the lower freestream turbulence levels require $N_t = 9 - 11$ [7].

For flat plate boundary-layer flow, Mack [68] proposes a functional relationship between N_t from linear stability considerations and the freestream turbulence intensity,

$$N_t = -8.34 - 2.4\ln(Tu). \tag{3.32}$$

This correlation is derived from several experimental studies and comparison to linear stability analysis. It is valid for turbulence intensities $10^{-3} < Tu < 10^{-2}$ and is used in the present work to evaluate the critical N_t-factor for transition experiments on a flat plate in Chapter 4. Arnal et al. [7] elaborate that the functional relationship can be applied under varying pressure gradients but care has to be taken to calibrate the method with experimental data. Since this function is only applicable to flat plate flow, it cannot simply be employed for transition prediction on any kind of airfoil. Here, another empirical correlation between the measured transition location and the numerically derived N-factor evolution needs to be applied. According to Arnal et al. [7], this cannot easily be done for conventional airfoils with steep pressure gradients as for example in [75]. Since a NLF airfoil with moderate pressure gradients is employed in the current work, it is expected to facilitate the correlation between the experimentally measured transition location and the N-factor method.

In all cases, the combination of experiments and numerical stability analysis helps to explain and correlate the effect of DBD actuators on the transition process. The procedure was successfully applied for large eddy simulations by Quadros [83] to evaluate the effect of a pulsed DBD actuator on the hydrodynamic stability of laminar boundary-layer flow presented in [24]. For continuously operated DBD, the stability calculations were validated with direct numerical simulations by comparison of the growth rates [27], showing excellent agreement. In the following chapters, the approach is extended to flow-control experiments in wind tunnels and flight.

4 Flat Plate Experiments

A variety of different experimental setups is employed to quantify the impact of DBD plasma actuators on laminar boundary-layer flow. Primarily, a generic flat plate experiment in an open-circuit wind tunnel enables the quantification of the transition delay obtainable with different DBD actuator configurations. At the same time, the ionization region close to the electrodes is accessible by optical measurement techniques to evaluate the actuator impact on laminar velocity profiles and contained modal instabilities.

The generic flat plate setup does not comprise all features of a realistic application, however it decreases the number of variables to be considered and facilitates comparability with earlier experiments conducted by Grundmann [43]. The flat plate in combination with a displacement body reduces the dependence between pressure gradient and flow velocity to a simple linear relation. The sturdy setup presented in Chapter 3.3 enhances the repeatability of experiments and reduces the complexity of accompanying numerical investigations.

In order to quantify the pressure gradient imposed by the displacement body, the freestream velocity is measured over a large portion of the plate where transition occurs naturally. The results of the measurement for a nominal freestream velocity of 20 m/s, which will be kept constant for all experiments on the flat plate reported hereafter, are illustrated in Figure 4.1. Circles indicate the dynamic pressure calculated from a reference vane anemometer at the leading edge while squares illustrate simultaneous hot-wire measurements outside of the boundary layer ($y = 25\,\mathrm{mm}$) along the flat plate. A linearized fit for the hot-wire signal, converted into dynamic pressure, is applied and the function is indicated in the diagram. Whereas the wind-tunnel bulk velocity U_{ref} at the leading edge of the flat plate remains almost constant throughout all measurements, the downstream evolution of decreasing hot-wire velocities U_{CTA} indicates a positive pressure gradient of 83.6Pa/m along the test section. The pressure can be normalized by considering the evolution of $c_p = 1 - (U_{CTA}/U_{ref})^2$ along the plate. The pressure gradient over the considered downstream region is almost linear with $\Delta c_p/\Delta x = 0.4\,m^{-1}$. The hot-wire measurements within

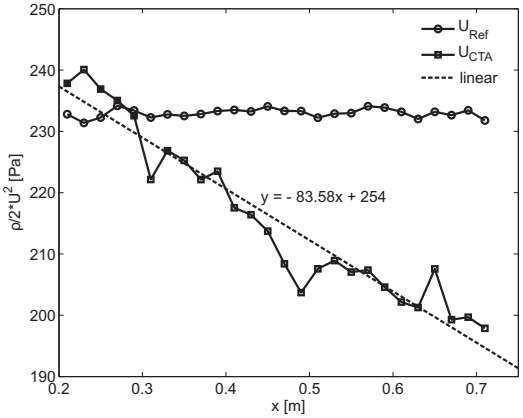

Figure 4.1: Pressure gradient along the flat plate at $U_\infty = 20\,\mathrm{m/s}$. Illustrated are the dynamic pressures calculated from the averaged reference velocity and the hot wire velocity signal.

the test section yield an average turbulence intensity of $Tu = 0.24\%$ outside of the boundary layer ($y = 50\,\mathrm{mm}$). This value is of importance for empirical transition prediction since the inflow conditions largely influence the transition process.

The DBD actuators applied in the following investigations are based on the standard setup defined in Chapter 3.1 and extend 440 mm in the spanwise dimension, exerting the force in streamwise direction. The resonant frequency of the combination of actuator and high voltage generator is $f_{pl} = 6\,\mathrm{kHz}$, yielding optimal efficiency of the body-force generation. The supply voltages and power consumptions of all configurations experimentally investigated are listed in Table 4.1 together with the approximate integral body force according to Kriegseis et al. [59]. All power and thrust values are normalized by the actuator length to facilitate a comparison of experiments with different actuator length and two-dimensional numerical calculations. The results suggest a slight non-linear dependence between actuator voltage and power consumption and an approximately linear relation between power consumption and produced thrust. Both observations are in agreement with the cited reference. Kriegseis et al. [61] investigate the impact of increasing flow velocities in the same wind-tunnel setting. Although a detrimental impact on the power consumption is reported at higher flow velocities and a corresponding decrease of the actuator thrust

V_{pp} [kV]	P [W/m]	T [mN/m]
8	33.7	7.8
9	38.1	9.1
10	45.7	11.3
11	55.1	13.5
12	64.4	15.6
13	74.6	17.7

Table 4.1: Comparison of actuator voltage peak-to-peak amplitude V_{pp}, power consumption P and produced integral thrust T for the investigated actuator settings.

may be assumed, negligible effects are found at flow velocities below 30 m/s. Since the airspeed is kept constant at 20 m/s for the following flat plate experiment, such effects are neglected. Furthermore, a velocity impact would influence all reported power settings in a similar way, scaling the absolute values but preserving the relative dependencies.

It should nevertheless be emphasized that the relation between the high voltage, power consumption and integral thrust is only known for the employed actuator setup. Other dielectric materials, thicknesses, power supplies or any other modifications to the actuator configuration require new measurements of all values. For the present DBD actuator, all quantities can be referenced correspondingly. From a fluid dynamics point of view, the integral thrust is usually the only relevant one. Since in experiments only the high voltage and the power consumption are directly measurable, the latter will be indicated to relate to the integral thrust. In numerical investigations, the force is directly integrable from the predefined model distributions. In all following experiments, the integral thrust will be primarily stated together with the power consumption to facilitate a comparison of different cases and to numerical studies presented in Chapter 5.

Excellent accessability of the flow by intrusive and optical measurement techniques introduced in Chapter 3.3 is one major advantage of the reported wind-tunnel setup. In the following, various measurements are presented to characterize the transition of the boundary layer and the impact of DBD flow control.

4.1 Hot-Wire Anemometry

A single boundary-layer hot wire is positioned directly at the surface of the flat plate and traversed along the streamwise direction. Each position is measured for 2 seconds at a sample rate of 16 kHz. The solid lines in Figure 4.2 (a) illustrate the standard deviation of the velocity signal σ_U within the intermittent region of the boundary layer, measured on three consecutive days. Starting from the laminar state with small velocity perturbations, the flow exhibits increasingly random fluctuations leading to an increase of the standard deviation of the sensor signal. It culminates within the intermittency region where the flow alternates between laminar and turbulent state until finally converging at the fully turbulent level. This characteristic evolution comparable to Figure 3.4 is seen both for the case without and with DBD actuation. As a first flow-control experiment, a single DBD actuator is applied $x = 350\,\text{mm}$ downstream of the leading edge and operated with a supply voltage of $V_{pp} = 10\,\text{kV}$. The circles and dashed line indicate the results under DBD operation at a thrust of $T = 11.3\,\text{mN/m}$ and a power consumption of $P = 45.7\,\text{W/m}$. Despite certain deviations due to the experimental sensitivity to changed ambient conditions, DBD operation moves the peak of the signal standard deviation to farther downstream locations in all three experiments. If the position of the signal peak is taken as a reference, an average transition delay of $\Delta x_{\text{trans}} \approx 50\,\text{mm}$ is observed. Considering the location of unaffected transition at $x = 500\,\text{mm}$, this corresponds to an increase of the transition Reynolds number $Re_{\text{trans}} = 6.6 \times 10^5$ of 10%. These initial flow-control experiments show that, despite experimental uncertainties involved in the highly sensitive transition experiments, repeatability is acceptable for the generic configuration to derive a flow-control effect.

The intermittency factor γ is illustrated in Figure 4.2 (b) for one of the presented flow-control experiments. The intermittency is calculated with the M-TERA method described by Zhang et al. [119] and a recommended calibration factor of $C = 2.0$. Although several different calibration factors were investigated, $\gamma = 0.5$ does not coincide with the peak of σ_U as described in literature [7, 37]. In the shown results, the intermittency slope starts at $x = 410\,\text{mm}$, far upstream of the standard deviation increase. Nevertheless, the quantified transition delay of $\Delta x_{\text{trans}} \approx 50\,\text{mm}$ found from the standard deviation approximately agrees with the offset of the intermittency factor curves. Because the calibration factor C needs to be adjusted for any new setup and since the intermittency slope is too steep to be adequately resolved at the chosen spatial resolution, the results of

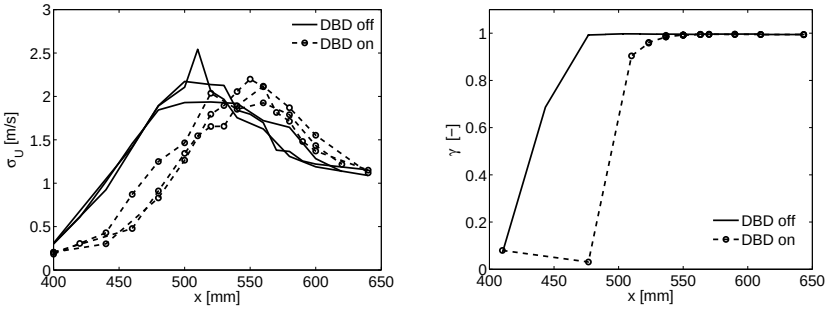

(a) standard deviation σ_U (b) intermittency γ

Figure 4.2: Transition behavior of boundary-layer flow at $U_\infty = 20\,\mathrm{m/s}$ characterized by the hot-wire standard deviation σ_U (a) and the intermittency factor γ (b), without and with DBD flow control at $T = 11.3\,\mathrm{mN/m}$ ($P = 45.7\,\mathrm{W/m}$).

intermittency investigations will not be shown henceforth.

In addition to the velocity standard deviation and the intermittency along the streamwise direction, the average velocity profiles and the disturbance profiles along the wall-normal coordinate indicate the boundary-layer state. Figure 4.3 illustrates the mean velocity profiles (solid lines) as well as the disturbance profiles (dashed lines) at four different streamwise locations, normalized with the freestream velocity U_∞. The ordinate shows the wall-normal position normalized with the displacement thickness δ_1 of the corresponding profile. Two different cases, without (crosses) and with (circles) DBD operation at $T = 11.3\,\mathrm{mN/m}$ ($P = 45.7\,\mathrm{W/m}$), are presented. Additionally, the solution of a laminar boundary-layer computation as discussed in Chapter 3.5.1 is illustrated as a dotted line at the first streamwise position (a) to indicate the accurate agreement between measurements and computations. For the disturbance profiles the hot-wire signal is bandpass filtered within the expected Tollmien-Schlichting instability range ($100 - 500\,\mathrm{Hz}$, compare Chapter 5), the standard deviation is calculated at each wall-normal location y and normalized with the mean flow velocity U_∞. For better visualization, the values are multiplied by a factor of 100.

At the first measurement location ($x = 400\,\mathrm{mm}$ downstream of the leading edge) presented in Figure 4.3 (a), only small velocity fluctuations are

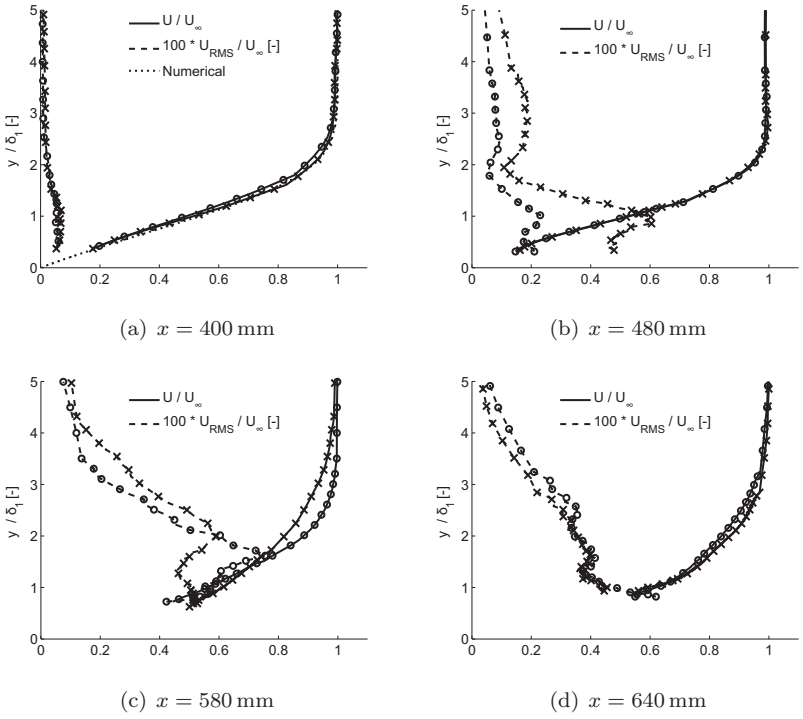

(a) $x = 400\,\mathrm{mm}$ (b) $x = 480\,\mathrm{mm}$

(c) $x = 580\,\mathrm{mm}$ (d) $x = 640\,\mathrm{mm}$

Figure 4.3: Velocity profiles (solid lines) and standard deviation of filtered hot-wire signal (100 Hz−500 Hz, dashed lines) for four different streamwise locations, without (x) and with (o) DBD operation at $T = 11.3\,\mathrm{mN/m}$ ($P = 45.7\,\mathrm{W/m}$). Flow velocity $U_\infty = 20\,\mathrm{m/s}$.

measurable inside the laminar boundary layer. The small differences for the cases with and without DBD operation are hardly distinguishable from measurement noise and random velocity fluctuations. At this early stage, the boundary-layer disturbances are yet too small to experience a dramatic influence by the boundary-layer stabilization. The averaged velocity profiles on the other hand do no longer show significant differences since the stabilizing impact is limited to a small region downstream of the actuator at $x = 350\,\mathrm{mm}$. As the disturbances propagate downstream (b), they are amplified and eventually show typical characteristics of Tollmien-Schlichting waves. These are the global disturbance maximum within ($y/\delta_1 \approx 1$) and another local maximum on top of the boundary layer ($y/\delta_1 \approx 3$), as well as the minimum close to the boundary-layer edge ($y/\delta_1 \approx 2$). Although an impact on the mean velocity profiles can hardly be distinguished, the disturbance amplitude under the influence of the actuation is reduced. At farther downstream locations (c), the disturbance looses the typical TS-wave shape as the breakdown into three-dimensional structures is initiated. Here, the actuated velocity profile still shows laminar characteristics whereas a turbulent or highly intermittent shape is obtained without flow control. In the fully turbulent flow (d), the maximum standard deviation decreases and is situated directly at the wall. As soon as the controlled flow is fully turbulent, it no longer exhibits any differences compared to the uncontrolled case.

The averaged velocity profiles experience a dramatic shape change during transition which can be characterized by the shape factor $H_{12} = \delta_1/\delta_2$. Solid lines in Figure 4.4 illustrate the distribution of the shape factor H_{12} along the streamwise coordinate x without DBD operation. Lines with circles as markers indicate experimental results obtained under operation of the single DBD actuator at $T = 11.3\,\mathrm{mN/m}$ ($P = 45.7\,\mathrm{W/m}$). The scatter of the results for three different days is higher than for the standard deviation measurements presented in Figure 4.2 (a). In the initially laminar phase between $x = 400 - 470\,\mathrm{mm}$, the shape factor H_{12} being larger than 2.6 agrees with the theory for laminar flow subjected to adverse pressure gradients. Downstream of the actuator location it drops continuously to a value of 1.4 characterizing a fully turbulent velocity profile. For the case with DBD actuation, the slope starts farther downstream as compared to the case without DBD forcing. Since the shape factor experiences a monotonous decrease throughout the transition region and no clearly specified value relates to the onset or end of transition, a threshold has to be defined to compare the cases with and without DBD actuation. To quantify

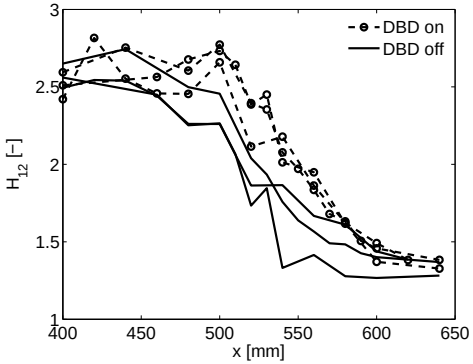

Figure 4.4: Transition behavior of boundary-layer flow at $U_\infty = 20\,\mathrm{m/s}$ characterized by shape factor H_{12} without and with DBD actuation at $T = 11.3\,\mathrm{mN/m}$ ($P = 45.7\,\mathrm{W/m}$).

the distance $\Delta x_{\mathrm{trans}}$ by which the transition is delayed, a value of $H_{12} = 2$ is used in accordance with earlier investigations by Grundmann and Tropea [47]. This yields an average transition delay of $\Delta x_{\mathrm{trans}} = 30\,\mathrm{mm}$ with significant scatter of the results of different days.

The spectral content of the hot wire velocity signal is evaluated via fast Fourier transformation (FFT) and plotted in Figure 4.5 for different streamwise locations. The dotted curve illustrates the frequency content outside of the boundary layer where only the broadband, low-amplitude freestream turbulence is found. The solid line presents the data for a position $y = 0.1\,\mathrm{mm}$ above the flat plate without DBD forcing and is contrasted with the case with DBD operation (dashed line) at $T = 11.3\,\mathrm{mN/m}$ ($P = 45.7\,\mathrm{W/m}$). It should again be noted that a low-pass analog filter with a cutoff frequency of $f_c = 3.15\,\mathrm{kHz}$ is applied to remove electromagnetic noise produced by the DBD actuation. In the laminar region of the boundary layer (a), a prominent frequency range around 250 Hz dominates. The naturally amplified frequencies inside the boundary layer range between 100 Hz and 500 Hz which agrees well with stability analysis (Chapter 5.2). The disturbance amplitudes increase during the downstream development (b), indicating the growth of two-dimensional Tollmien-Schlichting waves. For this position the positive influence of the DBD actuator becomes apparent. The velocity fluctuations without DBD actuation increase and start to spread to higher frequencies, whereas with the DBD actuator turned on,

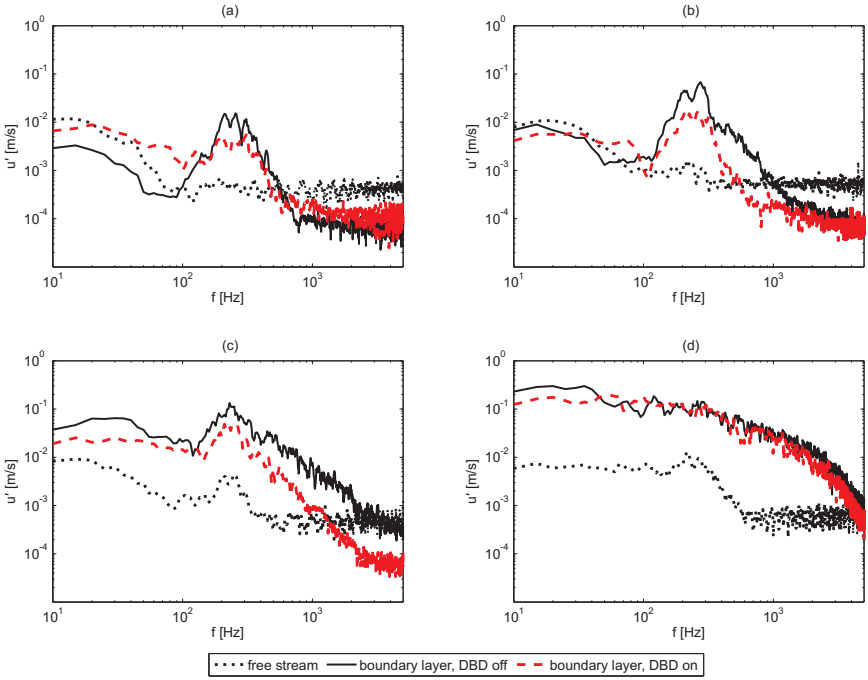

Figure 4.5: Spectral analysis of hot-wire signal for positions (a) $x = 400\,\mathrm{mm}$, (b) $x = 440\,\mathrm{mm}$, (c) $x = 480\,\mathrm{mm}$, (d) $x = 640\,\mathrm{mm}$. Dotted lines outside ($y = 15\,\mathrm{mm}$), solid lines inside ($y = 0.1\,\mathrm{mm}$) the boundary layer at $U_\infty = 20\,\mathrm{m/s}$. Band-pass filtering between 20 Hz and 3.15 kHz. Dashed lines inside boundary layer with DBD forcing at $T = 11.3\,\mathrm{mN/m}$ ($P = 45.7\,\mathrm{W/m}$).

the state remains similar to that shown in (a). As the boundary layer transitions (c) without the flow control, a broadband increase of the fluctuations occurs until finally reaching the chaotic, turbulent state characterized by the monotonic spectrum at (d) $x = 640\,\mathrm{mm}$. For the actuated case, this transitional behavior is postponed. Finally, the overall level of the frequency content of the laminar freestream is one order of magnitude lower than within the turbulent boundary layer.

The present investigation demonstrates that DBD actuation can delay transition initiated by naturally developing Tollmien-Schlichting waves under adverse pressure gradients. The stabilizing effect does not only lead to an attenuation of single frequency disturbances as shown by Grundmann and Tropea [44], but also delays transition initiated by broadband multi-frequency instabilities. Statistical and integral, experimentally determined quantities are compared concerning the quantifiability of the transition delay $\Delta x_{\mathrm{trans}}$. Comparing the results for σ_U, γ and H_{12}, the observed transition delay varies between 30 and 50 mm dependent on the considered flow quantity. At DBD operating frequencies $f_{pl} \geq 6\,\mathrm{kHz}$, a negative influence on the stability due to unsteady force production can be neglected since high frequency content is naturally damped by viscous effects. With the presented configuration of a single DBD actuator operating at $T = 11.3\,\mathrm{mN/m}$ ($P = 45.7\,\mathrm{W/m}$), the transition Reynolds number can be increased by approximately 10%. An experimental optimization of the obtainable transition delay by variation of the operating power or actuator placement is possible with the generic setup. Before such investigations are presented in Section 4.4, other measurement techniques are employed to learn more about the stability characteristics of the flow subject to DBD forcing.

4.2 Phase-Locked Particle Image Velocimetry

The phase-locked particle image velocimetry described in Chapter 3.3.2 is employed to investigate the impact of DBD operation on deterministic flow instabilities inside the laminar boundary layer. At a freestream velocity of $U_\infty = 20\,\mathrm{m/s}$, the disturbance source excites two-dimensional Tollmien-Schlichting (TS) instabilities at a frequency of $f_{\mathrm{exc}} = 250\,\mathrm{Hz}$ and creates streamwise wave amplitudes of approximately $0.8\%\,U_\infty$. Only being this close to the limit of linear disturbance evolution does the signal-to-noise ratio enable adequate acquisition of the wave amplitudes and propagation.

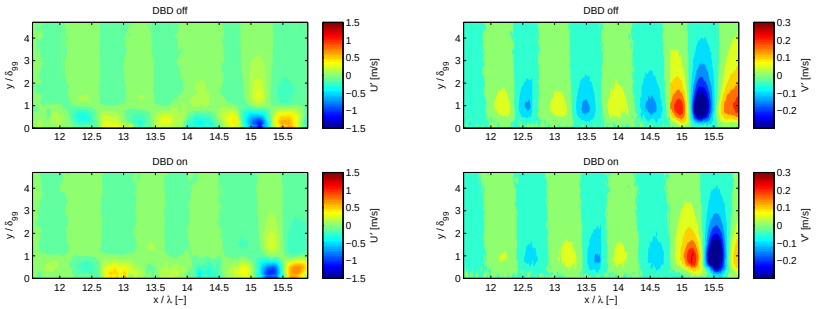

(a) Streamwise fluctuation u'

(b) Wall-normal fluctuation v'

Figure 4.6: Comparison of streamwise (a) and wall-normal (b) disturbance amplitudes at $U_\infty = 20\,\mathrm{m/s}$ and artificial disturbance excitation at $f_{\mathrm{exc}} = 250\,\mathrm{Hz}$. Cases without (upper) and with (lower) DBD operation at $T = 11.3\,\mathrm{mN/m}$ ($P = 45.7\,\mathrm{W/m}$).

The effect of a DBD actuator positioned at $x = 350\,\mathrm{mm}$ is investigated. It covers the whole spanwise dimension of the test section (440 mm) such that a two-dimensional forcing can be assumed if the actuator is operated at $T = 11.3\,\mathrm{mN/m}$ ($P = 45.7\,\mathrm{W/m}$). The PIV system is aligned in the center plane of the test section and traversed to four different locations downstream of the actuator. This extended measurement region covers approximately 4.5 disturbance wavelengths ($\lambda = 31.5\,\mathrm{mm}$) and allows the resolution of the spatial wave evolution. The wavelength λ is henceforth used to normalize the streamwise coordinate x.

The results presented in Figure 4.6 indicate that the application of the continuously operated DBD actuator at $x/\lambda = 11.2$ leads to a substantial reduction of average TS wave amplitudes. Illustrated are the contour levels of the streamwise (a) and wall-normal (b) velocity fluctuation components u'_Φ and v'_Φ for one phase angle Φ after subtracting the mean flow $\hat{u}$ and $\hat{v}$, respectively. The comparison of the streamwise component with and without DBD operation shows a reduction of 10% immediately downstream of the actuator. Interestingly, the wall-normal velocity component is significantly higher damped by $20 - 25\%$. Apart from the immediate amplitude reduction close to the actuator, the downstream evolution of the waves is of major importance for the transition process. As the flow propagates downstream, unstable waves are amplified and the growth rates become

measurable. Without DBD operation, the streamwise amplitude increases from 0.3 to 1 m/s over a distance of 4λ, the wall-normal component as well triples from 0.06 m/s to 0.2 m/s. With the DBD in operation, a lower amplification by only a factor of 2 is observed up to $x/\lambda = 15$.

Furthermore, an acceleration of the disturbance propagation speed is observed through the flow-control effect. Until the end of the domain, the disturbances under influence of the DBD have traveled $0.3\,\lambda$ farther than without flow control. The phase speed of the waves is not abruptly increased at the actuator location but continuously downstream. This suggests that the changed stability properties rather than an immediate flow acceleration lead to a change of the disturbance propagation behavior. The results are in quantitative agreement with linear stability analysis by Duchmann et al. [24] showing an increase of the phase speed by pulsed DBD operation in the order of 10%. The observed change of the convective speed macroscopically indicates the changed stability properties. The induced momentum changes the velocity distribution inside the boundary-layer profile and, hence, the ambient conditions for disturbance propagation. Since the phase speed $c_r = \omega/\alpha_r$ is coupled to the angular frequency $\omega = 2\pi f$ and the complex wavenumber α, it is plausible that a change of the flow stability leads to altered propagation properties.

The macroscopic effects of DBD operation on TS instabilities become apparent by the chosen measurement method. Nevertheless, a more detailed focussing on the stability properties of the boundary-layer profiles is necessary to understand the mechanisms of stability enhancement and to eventually optimize the DBD actuator for this task. In the following, the velocity profiles in the zone of maximum acceleration due to the discharge will be more thoroughly analyzed.

Analysis of the localized influence of DBD actuation on the boundary-layer profiles next to the exposed electrode allows a quantification of the impact on the flow stability. Although the mean velocity profile is only slightly changed, the shape factor is altered significantly at the actuator location. A local change of this value indicates an impact on hydrodynamic stability and subsequently the expected transition location. Figure 4.7 illustrates the shape factor H_{12} calculated for velocity profiles obtained by PIV without any phase locking upstream and downstream of the actuator. In order to resolve the actuator effect and to guarantee a sufficient resolution of the boundary layer in wall-normal direction, the measurement window of 32 mm width is traversed to four downstream locations, yielding a total field of view of 120 mm. To reduce the influence of measurement uncertainties

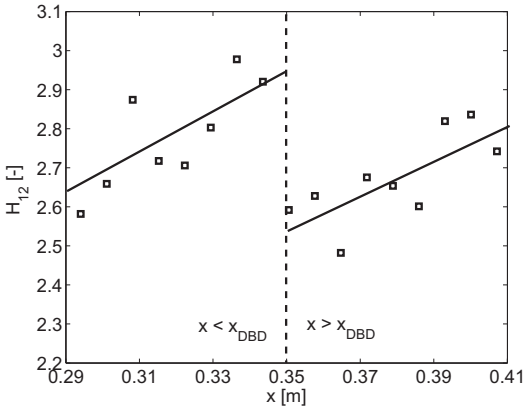

Figure 4.7: Shape factor H_{12} around actuator location $x = 0.35\,\mathrm{m}$, derived from PIV measurements. $U_\infty = 20\,\mathrm{m/s}$, $T = 11\,\mathrm{mN/m}$ ($P = 45.7\,\mathrm{W/m}$).

and surface reflections on the calculated shape factor, ensemble averaging and spatial averaging in streamwise direction are necessary. Two thousand single velocity fields from PIV are ensemble averaged to reduce the impact of mean-flow velocity fluctuations and random errors. In streamwise direction, twenty velocity profiles are averaged in sections of 6 mm to reduce the error by surface reflections and enhance the accuracy close to the wall. From these averaged profiles, the local shape factor can be calculated to derive a trend of the development upstream and downstream of the actuator. Solid lines, which are fitted by a least square procedure, are illustrated to resolve the trends despite large data scatter. Upstream of the actuator, the shape factor slope due to the adverse pressure gradient is slightly exaggerated caused by measurement uncertainties. Despite these uncertainties, a clear drop of the shape factor by approximately $\Delta H_{12} = 0.35$ is noted at the actuator location. This local decrease may be interpreted similar to a local flow acceleration, which is stabilizing the flow. Downstream, the shape factor increases since the actuator effect is spatially confined. Albrecht et al. [2] showed for electromagnetically forced flow that a monotonic relation between the shape factor and the critical Reynolds number cannot be assumed. Locally, the flow can be even more stable than an asymptotic exponential profile obtainable from continuous boundary-layer suction. Therefore, a linear stability analysis of the experimental velocity

profiles has to be conducted, but spatially finer resolved velocity data is required than PIV can provide at the resolution used in this section. Due to the opposing constraints to resolve the whole boundary-layer thickness and provide sufficient data points close to the wall, a different measurement technique is chosen to obtain the necessary velocity profiles.

4.3 Laser Doppler Anemometry

Two-velocity component laser Doppler anemometry (LDA) enables highly-resolved pointwise flow measurements of two perpendicular velocity components. In the present work, the streamwise and the wall-normal velocities u and v within the boundary-layer flow are acquired. In contrast to the PIV measurements reported before, the following experiment focusses on the accurate measurement of averaged boundary-layer profiles. The small interferometric sensor volume in combination with the transparent acrylic surface of the flat plate avoids reflections and enables accurate velocity measurements close to the surface. This is of importance for the determination of the exact wall distance and profile curvature. Since the velocity profile curvature discussed in Chapter 2.1 is not only relevant for inviscid instability mechanisms (see Fjørtoft [33]) but also for the considered Tollmien-Schlichting instability, it needs to be sufficiently well resolved for adequate analysis of the viscous flow stability.

Although only slight modifications of the laminar velocity profiles close to the operating DBD actuator are attained, the flow stability is strongly influenced. Figure 4.8 illustrates the averaged velocity profiles (circles), the first derivative (squares) and the second derivative (triangle) with respect to the normalized wall normal coordinate y/δ_1 at $x = 360\,\mathrm{mm}$, namely 10 mm downstream of the single DBD actuator. The values are normalized with the respective maximum to facilitate combination of all quantities in one graph. Filled symbols illustrate the baseline case whereas empty symbols represent DBD actuation at $T = 13.5\,\mathrm{mN/m}$ ($P = 55.1\,\mathrm{W/m}$). A difference between the averaged profiles with and without DBD operation is hardly visible, but especially the second derivative shows a significant deviation by DBD actuation. Since the second derivative indicates the profile curvature which is of major importance for the flow stability as described in Chapter 2.1, a small alteration can have significant impact on the transition process. The acquisition of such accurate boundary-layer data is difficult and time consuming and should be limited to the region where an impact of DBD

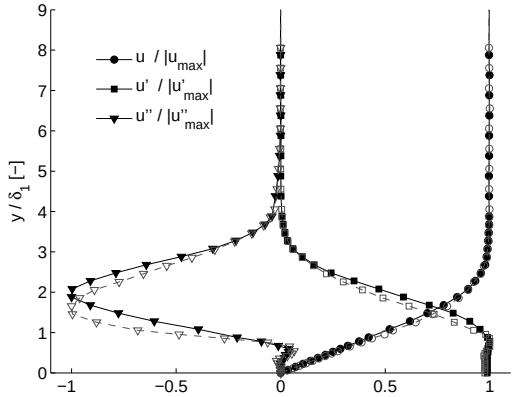

Figure 4.8: Streamwise velocity profiles $u(y)$ normalized with $U_\infty = 20\,\mathrm{m/s}$ (circles) as well as first (squares) and second (triangles) derivatives with respect to the wall-normal direction y, obtained with LDA measurements. Filled symbols without, empty symbols with DBD actuation at $T = 13.5\,\mathrm{mN/m}$ ($P = 55.1\,\mathrm{W/m}$).

forcing on the velocity profiles is expected. The finely resolved data is directly analyzed with the linear stability code elaborated in Chapter 3.5.3 and the results are presented in Chapter 5.3.

The different experimental measurement techniques enable the correct localization of the transition process and quantification of its delay by DBD operation. Laser-optical measurements resolve the immediate flow velocities found within the acceleration region of the ionized plasma, illustrate the response of modal disturbances to the DBD forcing and contribute to the discussion of the stabilizing actuator effect.

4.4 Flow-Control Optimization

For increased effectiveness of DBD flow control, an optimization of the obtainable transition delay is desired. Earlier investigations by Grundmann [43] demonstrated enhanced transition delay by increasing the actuator thrust and changing the actuator location. Since the actuator thrust induces a certain momentum in the flow which has to be related to the

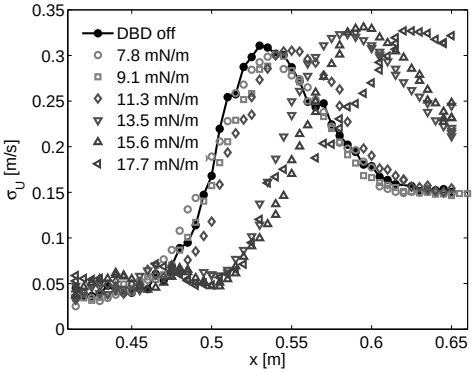

Figure 4.9: Hotwire standard deviation σ_U along the flat plate as a function of actuator thrust T.

freestream momentum, a monotonic influence on the achievable transition delay may be expected. Concerning the actuator placement, the non-trivial and frequency-dependent stability characteristics of the flow require consideration. By systematic variation of both parameters, the dependence between actuator forcing and the flow stability properties is explored and conclusions concerning the flow-control effectiveness are drawn.

4.4.1 Thrust Variation

The actuator thrust is varied to evaluate the influence on the transition delay. By systematically increasing the supply voltage, the power consumption and subsequently the force field magnitude increase according to Table 4.1. The peak of the hot-wire standard deviation σ_U is again utilized to quantify the transition delay $\Delta x_{\mathrm{trans}}$ for a single DBD actuator at $x = 350\,\mathrm{mm}$, compare Figure 4.9. The transition location without DBD forcing is now found at $x = 0.52\,\mathrm{m}$ due to a reconstruction of the wind tunnel after the measurements presented in Section 4.1. The aim of the wind-tunnel modifications [15] was to enhance the flow quality by introduction of improved screens and a honeycomb, leading to a reduced turbulence intensity of $Tu = 0.19\%$ for the flow at $U_\infty = 20\,\mathrm{m/s}$ and a downstream shift of the transition location even without flow control. At low actuator thrust, the obtained transition delay is hardly measurable. Due to the na-

T [mN/m]	Δx_{trans} [mm]
7.8	10
9.1	15
11.3	30
13.5	55
15.6	65
17.7	95

Table 4.2: Transition delay dependent on integral actuator thrust.

ture of dielectric barrier discharges, a threshold voltage around $V_{pp} = 3\,\text{kV}$ exists below which no plasma is formed for the actual actuator configuration. Between 3 and 6 kV, an uneven plasma distribution characterized by single filaments creates a three-dimensional force field. Although the force magnitude is small, even a negative influence on transition is seen in some data points for $T = 7.8\,\text{mN/m}$ due to the random nature of the filaments. The measurement at $V_{pp} = 8\,\text{kV}$ and $T = 11.3\,\text{mN/m}$ provides a homogeneous surface discharge and a small delay of transition is observed. For higher applied body forces, the transition delay effect is enhanced, but care has to be taken not to exceed the breakdown voltage which destroys the actuator. This voltage is defined by the material and thickness of the dielectric. Excessively high voltages and associated fluid accelerations have the additional disadvantage that an overshoot in the velocity profile can occur. This leads to a destabilization of the flow, rendering the actuation useless for transition delay. Riherd and Roy [86] analyzed the occurrence of inviscid instability modes for excessively distorted velocity profiles. For high forcing at $T = 17.7\,\text{mN/m}$ the typical shape of the σ_U-curve is distorted around $x = 550\,\text{mm}$, indicating the onset of initial undesired effects.

A downstream shift of the transition location in the range of $10 - 95\,\text{mm}$ is obtained by varying the integral actuator thrust between 7.8 mN/m and 17.7 mN/m. Grundmann [43] proposed the existence of an optimum body force for transition delay at much lower flow velocities between $U_\infty = 6 - 8\,\text{m/s}$. At the present flow speed and with the given actuator materials, no optimum can be identified due to breakdown-voltage limitations. Yet it remains promising to increase the DBD thrust if adequate dielectric material is available, especially if flow control at even higher freestream velocities is attempted. Presently, it appears more promising to apply consecutive actuator arrays with lower individual force magnitudes in the

linear amplification range of Tollmien-Schlichting instabilities.

4.4.2 Actuator Arrays

After thorough analysis of the transition behavior influenced by a single DBD actuator at a fixed location, the actuator position is focussed to enhance the transition control effectiveness. Besides the position of a single actuator, arrays of actuators consecutively placed in streamwise direction promise a more homogeneous flow forcing at reduced force magnitude levels.

Three identical DBD actuators are flush-mounted on the flat plate at different locations $x_1 = 320\,\mathrm{mm}$, $x_2 = 350\,\mathrm{mm}$ and $x_3 = 380\,\mathrm{mm}$. They can be operated independently or in combination at any desired thrust within the range of Table 4.1. The DBD operating frequency $f_{pl} = 6\,\mathrm{kHz}$ is kept constant to facilitate the comparison with the single-actuator experiments at $x_{mathrmDBD} = x_2 = 350\,\mathrm{mm}$. The integral thrust is maintained at an intermediate level of $T = 15.6\,\mathrm{mN/m}$ or corresponding power consumption $P = 64.4\,\mathrm{W/m}$ to avoid premature actuator damage and obtain a relatively large transition delay. In the case of multiple actuator arrays, the net actuator length increases and the total consumed power is multiplied by the number of actuators.

First, the DBD actuators are operated independently at various locations to evaluate the effect of positioning on the transition delay. Figure 4.10 illustrates the hot-wire standard deviation along the flat plate for DBD operation at the three positions $x_1 - x_3$. At x_1, almost no transition delay is observed whereas DBD forcing at x_2 approximately confirms the $\Delta x_{\mathrm{trans}} = 55\,\mathrm{mm}$ found from Table 4.2 for $T = 15.6\,\mathrm{mN/m}$ ($P = 64.4\,\mathrm{W/m}$). The slightly reduced $\Delta x_{\mathrm{trans}} = 50\,\mathrm{mm}$ might derive from subtle variations of the wind-tunnel conditions. If operated at x_3, the transition is significantly postponed, yielding $\Delta x_{\mathrm{trans}} = 120\,\mathrm{mm}$. If the first and last actuator are operated together ($x_{1,3}$), the additional improvement of the transition delay is marginal, $\Delta x_{\mathrm{trans}} = 140\,\mathrm{mm}$, in comparison to separate operation of the third actuator. By adding the remaining actuator ($x_{1,2,3}$), another 25 mm are gained to $x_{\mathrm{trans}} = 165\,\mathrm{mm}$.

In context of position variation of single DBD actuators, the placement at the farthest downstream position x_3 is most effective to delay transition. Following this trend, the existence of an optimum location can be expected since the actuator will not be effective if positioned beyond the natural transition location. Further downstream placements would have required complex modifications of the test rig, such that no optimum location is

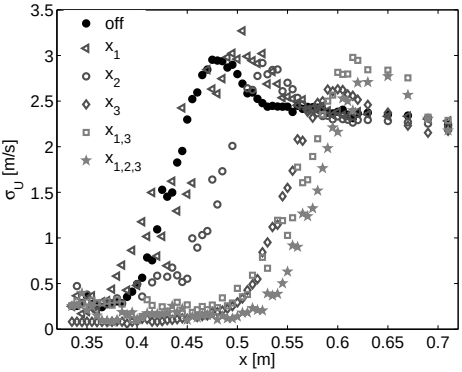

Figure 4.10: Transition positions as a function of actuator placement and array permutation, $T = 15.6\,\mathrm{mN/m}$ ($P = 64.4\,\mathrm{W/m}$), $U_\infty = 20\,\mathrm{m/s}$.

identified. If other actuators are added, only slight improvements are measured at the cost of doubled or tripled power consumption. In terms of efficiency, relating the net effect to the energy expenditure, operation of all three actuators at the same power consumption cannot be recommended although the effectiveness is enhanced. Adaption of the actuator magnitude according to the respective position may be a final necessity to optimize the flow-control efficiency. Nevertheless, the presented results indicate that correct actuator positioning is of higher importance for increasing the overall transition-delay effectiveness.

4.5 Conclusions

Generic flat plate experiments are performed to demonstrate the control of naturally occurring, TS-wave dominated transition by means of a single DBD actuator. Statistical and integral evaluation of hot-wire measurements within the transitional boundary layer reveal a transition delay of $30 - 50\,\mathrm{mm}$, summing up to an increase of the transition Reynolds number of 10%. Spectral analysis of the hot-wire data clarifies the stabilizing effect of DBD actuation over a broad range of flow instability frequencies, such that single frequency and multi-band disturbances are attenuated by the thrust field.

Phase-locked PIV of artificially introduced disturbances illustrates the effect of plasma forcing on the propagation speed of boundary-layer disturbances. A corresponding change of the mean-flow stability properties is validated by additional measurements attesting a significant impact on the shape factor H_{12} of the laminar boundary layers next to the actuator location. The reduction of this value is related to an increase of the hydrodynamic flow stability, explaining the macroscopically observed transition delay. A further non-intrusive measurement technique is employed to derive highly-resolved boundary-layer profiles for a stability analysis of experimental data presented in Chapter 5.4.

A variation of the DBD actuator thrust leads to an optimization of the flow-control application. Increased effectiveness is found for higher forcing; however no optimum is identified at the speed of $U_\infty = 20\,\mathrm{m/s}$. The limited momentum induced by the single actuator compared to the freestream momentum restricts the obtainable effect. Due to the danger of dielectric breakdown at excessively high voltages, a limitation of the actuator power is necessary, such that the best achievable transition delay is limited by the actuator performance and not by stability effects. A variation of the actuator position and application of multiple-actuator arrays yields significantly enhanced effectiveness for optimized locations. The adequate positioning of an actuator appears more important than a multiplication of the force locations and the power consumption. Numerical investigations can be of great help to determine the most appropriate actuator location and simulate array combinations. Therefore, the next chapter presents results of such numerical investigations.

5 Stability Impact

Experiments on a generic flat plate setup in an open-circuit wind tunnel have shown the sensitivity of DBD transition delay to actuator number, positioning and thrust magnitude. For more advanced flow geometries on larger setups and if an optimization regarding the mutual dependence of all parameters is coveted, experimental studies are too time- and cost-intensive. Availability of adequate numerical tools is a necessity to comprehensively explore the parameter space and approach a net benefit of transition control. Numerical methods with adequate implementation of the underlying physical laws have been described in Chapter 3.5. Nevertheless, the incorporation of the DBD force needs to be validated based on experiments. The antecedently described generic experimental setup is a convenient test case for validation of the numerically simulated DBD effect.

In this chapter, a boundary-layer code with force implementation and subsequent linear stability analysis will be validated against experimental findings from Chapter 4.1. An empirical transition-prediction law is employed to relate the numerical stability analysis to experimentally measured transition locations. Alternatively, the stability analysis can be performed directly with experimentally measured boundary-layer profiles. Highly resolved data is acquired for this purpose via laser-optical measurements as presented in Chapter 4.3. The numerical analysis also facilitates the simulation of various thrust levels and multi-actuator geometries to be compared with measurements presented in Chapter 4.4. Linear stability analysis is utilized to relate the local flow stability properties to the variation of the actuator position. The positive results ordain the numerical codes for design of DBD transition control applications. This tool kit is used to design a flow-control experiment on a laminar wing glove, for which in-flight results will be presented in Chapter 6.3.

5.1 Code Validation by Comparison to Numerical Data

The boundary-layer solver and stability code presented in Chapters 3.5.1 and 3.5.3, respectively, have been employed for a parametrical study of airfoil boundary-layer flow by Köhler [56], comparing the results to another numerical tool kit extensively used at KTH in Stockholm. The good agreement of integral boundary-layer quantities evinces the applicability for flat plate and NLF airfoil boundary-layer flow. In addition to the boundary-layer solver, the linear stability analysis needs to be validated for prediction of TS-wave growth under the influence of DBD actuation. The linear stability code has proven its value for analysis of DBD influenced boundary-layer flows from large eddy simulations (LES) by Quadros [83] as shown in [24]. A thorough validation of the numerical methods, employing different setups or benchmark flow situations, is beyond the scope of this project and not provided in the manuscript. Nevertheless, some validatory computations are pursued to prove the correct implementation of the force field and adequate representation of the actuator effect on the flow stability.

Lüdeke et al. [66] analyze results from direct numerical simulations (DNS) based on stability theory to validate a linear stability code. Therefore, simulated TS waves are artificially introduced in the computations and the amplitude evolution is compared to stability theory. Following this approach, the presently elaborated stability code is applied to DNS computations of Blasius boundary-layer flow by Vieira et al. [111] as presented in [25]. The DNS simulates flat-plate flow at $U_\infty = 10\,\mathrm{m/s}$ and artificial excitation of two-dimensional waves at $x = 0.22\,\mathrm{m}$ at a frequency of $f = 110\,\mathrm{Hz}$. Two DBD actuators, positioned at $x_1 = 0.325\,\mathrm{m}$ and $x_2 = 0.425\,\mathrm{m}$, are simulated with the experimentally derived force field discussed in Chapter 3.5.2 and a thrust of $T = 7.8\,\mathrm{mN/m}$ each. Figure 5.1 (a) compares the wave amplitude evolution from DNS (markers) with a linear stability analysis (lines) of the averaged DNS velocity profiles for three different cases: without flow control, with DBD operation at x_1 and with simultaneous operation at x_1 and x_2. The integral N-factor, defined in equation (2.22) as the ratio of the local disturbance amplitude A and the amplitude A_0 at the critical point x_{crit} is illustrated over the streamwise direction. Almost coinciding evolutions for the numeric experiments via DNS and the amplification prediction by the linear stability solver are observed, although the DNS data comprises a non-parallel base flow with increasing boundary-layer thickness over the domain. Only in the exact proximity of the actuator location, the stability

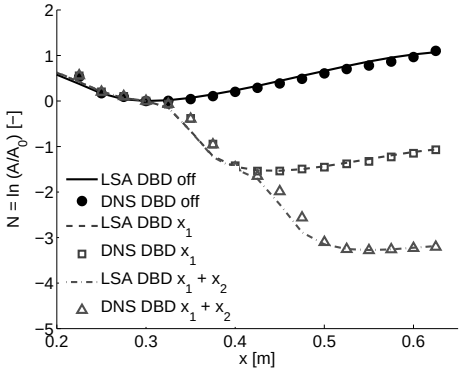

Figure 5.1: Comparison between wave amplitude evolutions from direct numerical simulation (DNS) and linear stability analysis (LSA) for Blasius boundary-layer flow subjected to DBD forcing at $x_1 = 0.325\,\mathrm{m}$ and $x_2 = 0.425\,\mathrm{m}$, from [25].

code predicts the amplitude decrease to be initiated slightly upstream as compared to the DNS. This effect is assumed to derive from the local non-parallelism of the flow induced by the actuator, which cannot be accounted for by linear stability analysis. Nevertheless, the downstream evolution of disturbance amplitudes is well captured by the LSA. As will be shown in the following section, transition prediction based on N-factors from LSA and an empirical law regarding the mean-flow turbulence level by Mack [68] yields excellent agreement with measured transition locations. More details on the application of LSA for transition prediction in boundary-layer flow subjected to DBD actuation are elaborated in [28]. A final validation of the numerical procedure is provided in the following by comparing experimentally measured transition locations to transition positions predicted by the LSA N-factor method.

5.2 Code Validation with Generic Flat Plate Experiments

To enable parametric studies of DBD transition control situations, a numerical boundary-layer solver developed by Köhler [56] together with a linear

stability code by Reeh [84] is employed. Both numerical methods are reviewed in Chapter 3.5. The boundary-layer code has not been employed for flow-control purposes before, such that a validation with experimental data is desired. The generic flat plate setup discussed in Chapter 4 is ideal for this purpose since integral boundary-layer quantities as well as transition measurements are available. Although the boundary-layer code cannot simulate flow transition, the combination with the linear stability code facilitates a transition prediction based on the e^N-method.

The input to the boundary-layer code is a pressure distribution along the flat plate. This can either be derived from measurements or simplified numerical approaches. The linearized pressure distribution from Figure 4.1 allows a computation of the laminar boundary-layer profiles within the measurement region. It does not account for the whole plate length or the leading edge region which is not accessible with the experimental equipment. Therefore, a simple Reynolds-averaged Navier-Stokes (RANS) computation of the experimental setup illustrated in Figure 3.7 provides the pressure distribution along the flat plate. The code *Open-FOAM* is used since experience with various geometric configurations for numeric DBD flow control is already available [63, 69]. A fully laminar calculation without any DBD forcing at the flow speed of $U_\infty = 20\,\mathrm{m/s}$ provides a pressure distribution which is in good agreement with the experimental data within the measurement region. Further on, this finely-resolved numeric representation of the pressure distribution constitutes the necessary input to the boundary-layer solver. Alternatively, the pressure distribution could have been obtained from a potential flow solution, but in this case the boundary-layer growth would not have been accounted for, slightly influencing the pressure gradient. The boundary-layer profiles are calculated with the finite-differences routine elaborated in Chapter 3.5.1.

The grid size in streamwise direction x is defined by the resolution of the input pressure distribution. Tests with different grid resolutions have shown that an equidistant grid spacing of 2.5 mm is sufficient to resolve the full length $l = 1.8\,\mathrm{m}$ of the flat plate with 750 streamwise positions. The wall-normal resolution scales with the Blasius length scale (3.3) for an optimal resolution dependent on the streamwise position. After convergence of the boundary-layer solution, this data is fed into the stability analysis routine described in Chapter 3.5.3. The accuracy of the wall-normal discretization by the spectral Chebyshev collocation method is validated by varying the number of Gauss-Lobatto grid points between 60 and 240. During validation, a number of 100 points proved sufficient to accurately

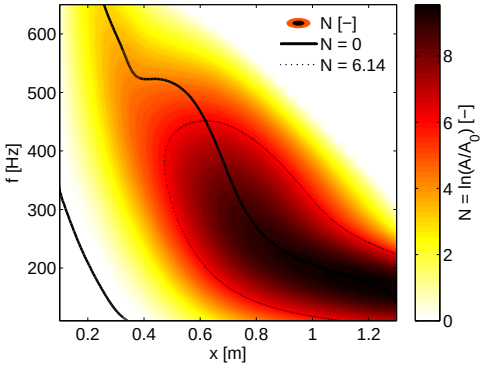

Figure 5.2: N-factor contours and neutral stability curve (solid line) of flow without DBD actuation. The dotted line illustrates the iso-contour of $N = 6.14$, corresponding to the transition threshold N_t for $Tu = 0.24\%$.

identify the most amplified Tollmien-Schlichting mode and compute the critical Reynolds number $Re_{\text{crit}} = 519.08$ of the zero-pressure gradient Blasius flow in close agreement with literature data (e.g. $Re_{\text{crit}} = 519.4$ in [91]).

The spatial formulation of the stability equations is chosen to solve for the two-dimensional Tollmien-Schlichting mode in the flat plate case, predicting the disturbance growth rates for given disturbance frequencies. Integration of the growth rates along the streamwise direction starting from the point of neutral stability allows the formulation of the N-factor as defined in equation (2.22). Despite being based on linear theory and therefore neglecting important characteristics of the transition to turbulence, the e^N-method can be utilized as an indicator for the transition occurrence. Figure 5.2 illustrates the N-factor development of the flow along the flat plate without DBD operation. N-factor iso-contours are plotted as a function of the downstream position x and the dimensional frequency f. Although the stability computations are conducted in normalized coordinates employing the Blasius length scale, the results shown in the illustration are presented in physical dimensions to facilitate comparison to the experiments in Chapter 4. The neutral stability curve is plotted as a thick solid line to separate the stable and unstable flow regime. An additional dotted

isoline is included which represents the level of $N = N_t = 6.14$. This critical N-factor value is calculated based on Mack's equation (3.32) for the turbulence intensity $Tu = 0.24\%$ encountered during the initial transition measurements presented in Chapter 4.1. It is first reached for a frequency of $f = 380\,\mathrm{Hz}$ in the vicinity of $x = 0.48\,\mathrm{m}$. This result differs by only 4% from the experimentally determined location of maximum standard deviation at $x = 0.5\,\mathrm{m}$ without flow control seen in Figure 4.2 (a). A very good agreement between the numerical prediction incorporating the ambient turbulence intensity and experimentally observed transition without flow control can be attested. The next step is to check the agreement under DBD forcing.

In order to implement the DBD force field presented in Chapter 3.1 into the boundary-layer code, the computational grid needs to be refined in the streamwise dimension. The pressure distribution in the area around the actuator position is linearly interpolated on 100 additional grid points. This increases the resolution of the boundary-layer grid and enables interpolation of the measured streamwise force field, compare Figure 3.2 (a), on the grid points. In order to guarantee comparability with the experimental results, the numerically implemented force field strength needs to coincide with the thrust magnitude in the experiments. For the thrust configurations between $T = 7.8 - 15.6\,\mathrm{mN/m}$ indicated in Table 4.1, experimentally measured force field distributions are available for numerical implementation. Only these force field distributions are used without modification for all numerical investigations, such that it is convenient to indicate the integral thrust magnitude T for each computational result.

For the initial flat plate experiment described in Chapter 4.1, the integral thrust is $T = 11.3\,\mathrm{mN/m}$. To experimentally validate the force implementation, the integral boundary-layer quantities under influence of the force field can be compared. A local decrease of the boundary-layer displacement thickness δ_1 due to DBD operation is reported by several authors [24, 40, 46, 52, 83, 96], leading to a decrease of the shape factor H_{12}. The shape factor evolution according to the numerical solution of the boundary-layer code is illustrated in Figure 5.3 (dashed line) and compared to experimental PIV (squares) and hot-wire (circles) measurements from Chapter 4.2. Both the PIV measurements and the numerics indicate a sharp drop of the shape factor of $\Delta H_{12} = 0.3$ at the actuator location. The numerical representation of the shape factor asymptotically converges towards the initial value ahead of the actuator. A strong gradient with subsequent asymptotical behavior appears physically reasonable due to the

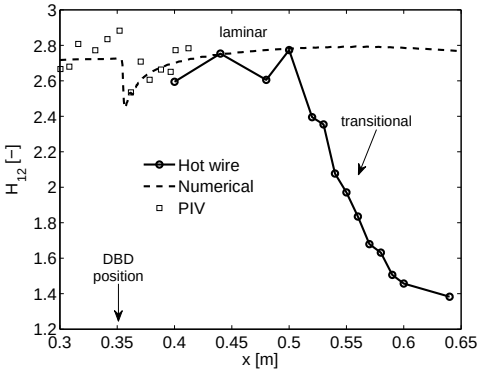

Figure 5.3: Shape factor evolution measured by hot-wire and PIV compared to the numerical boundary-layer solution. Actuator forcing at $x = 0.35\,\mathrm{m}$ with $T = 11.3\,\mathrm{mN/m}$.

local confinement of the actuator force, showing decreasing magnitude and spatial extent along the streamwise direction.

Also included in the plot are the experimental results from hot-wire measurements downstream of the single operated DBD actuator (solid line). All presented results are in good agreement between $x = 0.3\,\mathrm{m}$ and $x = 0.5\,\mathrm{m}$ considering the experimental difficulties of determining the shape factor. Since the boundary-layer solver does not predict transition and therefore delivers a fully laminar solution, the development of the shape factor in the transition region downstream of $x = 0.5\,\mathrm{m}$ deviates from the measured values obtained with hot-wire anemometry.

If the flow is controlled, a representation of the neutral stability curve as in Figure 5.2 is not expedient since the body force stabilizes the flow within the normally unstable region. The neutral stability curve cannot be represented by a single line and contour plots reveal an unusual shape. Therefore, an analysis of the N-factor evolution for discrete disturbance frequencies is more convenient. The disturbance evolutions are provided in Figure 5.4 (a) for the case without actuation. In agreement with the conclusions from Figure 5.2, the most amplified disturbance for the transition threshold $N_t = 6.14$ is approximately $f = 380\,\mathrm{Hz}$ in the vicinity of $x = 0.48\,\mathrm{m}$. The effect of the local stabilization due to DBD operation is illustrated in Figure 5.4 (b). The cumulative growth factor downstream of

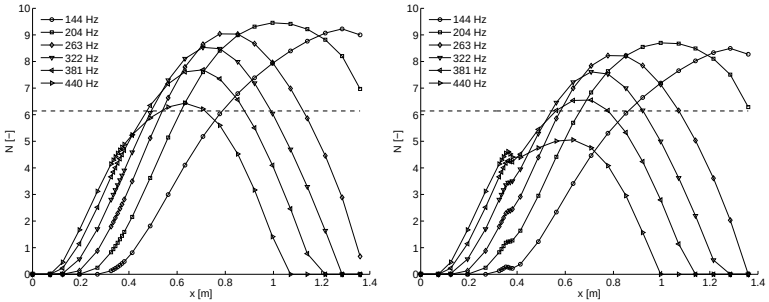

(a) DBD off (b) $T = 11\,\mathrm{mN/m}$

Figure 5.4: N-factor evolution for discrete disturbance frequencies (various markers) with transition threshold $N_t = 6.14$ (dashed line) without (a) and with (b) DBD actuation at $T = 11.3\,\mathrm{mN/m}$.

the actuator location $x = 0.35\,\mathrm{m}$ is significantly reduced for all frequencies. The disturbance amplitudes start to grow again a few millimeters downstream, but the location of crossing the transition threshold is moved to $x = 0.54\,\mathrm{m}$. This shift of the threshold location of approximately 55 mm downstream slightly overpredicts the experimentally measured transition delay, quantified by $30 - 50\,\mathrm{mm}$ in Chapter 4.1. Additionally, the stability analysis reveals that the frequency relevant for transition is shifted towards lower values, here to approximately $f = 320\,\mathrm{Hz}$.

For further validation of the numerical approach, a parametric simulation of the actuator thrust and position variation presented in Chapter 4.4 is performed.

Figure 5.5 illustrates a comparison between the experimentally measured and numerically predicted transition delay during variation of the actuator thrust. The experimental data was already presented in tabular form in Table 4.2. The numerical transition prediction is based on Mack's law (3.32) and a critical N-factor $N_t = 7$ accounting for the lower turbulence intensity $Tu = 0.19\%$ after the wind-tunnel reconstruction mentioned in Chapter 4.4. The trend of the transition prediction for various actuator thrusts agrees well with the experimentally measured values. The variation of the turbulence intensity according to the changed wind-tunnel conditions additionally validates the applicability of the empirical transition prediction based on the inflow conditions.

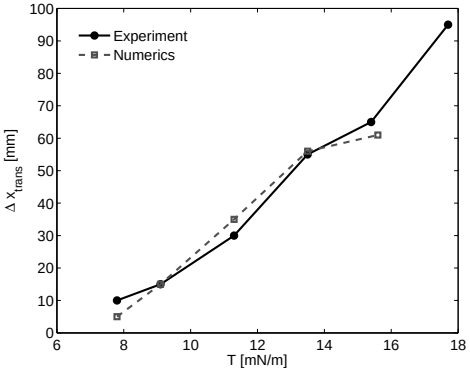

Figure 5.5: Experimentally measured and numerically predicted transition delay for various thrust magnitudes. Transition threshold $N_t = 7$ for a turbulence intensity of $Tu = 0.19\%$.

5.3 Numerical Optimization of Generic Flow Control Experiments

The good agreement of empirical transition prediction based on linear stability analysis with experiments for different thrust levels predestines the numerical tools for flow-control optimization. The experimental position variation presented in Chapter 4.4.2 suggests an optimal location for the force allocation, although the absolute determination of such a position is beyond the scope of the experiments. Experimental configurations with different positions and combinations of multiple actuators are reproduced with the boundary-layer solver and analyzed with the stability code. Table 5.1 facilitates a comparison of these numerical results and the measurements for an assumed critical N-factor $N_t = 7$. The results indicate that the boundary-layer code with subsequent linear stability analysis reproduces the trends of transition delay qualitatively correct without providing a quantitative match with the experiments. The numerical results underestimate the importance of correct actuator positioning, whereas the effect of streamwise serialization of actuator arrays is overrated. Apparent reasons could be the disregard of the position dependence of the absolute disturbance amplitude and non-linear effects, rendering it a problem of the linear stability analysis.

$x_{\mathrm{DBD}}[mm]$	$\Delta x_{\mathrm{trans,\ exp}}[mm]$	$\Delta x_{\mathrm{trans,\ num}}[mm]$
330	15	38
350	50	56
380	120	72
330 & 380	140	140
330 & 350 & 380	165	182

Table 5.1: Comparison of experimentally measured and numerically predicted transition delay for varying actuator locations and arrays on a flat plate. The actuator thrust is fixed at $T = 15.6\,\mathrm{mN/m}$ in agreement with the experimental setup.

Nevertheless, the wave amplitude evolution in DNS computations for multiple actuator arrays by Vieira et al. [111] is in good agreement with a stability analysis of the DNS boundary-layer profiles as illustrated in Figure 5.1 (a). This partially validates the stability code and points towards incorrect representation of multiple actuators in the boundary-layer code. After ruling out incorrect grid interpolation and scrutinizing the integral thrust within the computational domain of the boundary-layer code, it is deemed possible that the cumulative effect of multiple actuators is treated inappropriately as a simple linear addition of the stabilizing effects. The finite-differences solver requires further experimental validation with more extensively distributed actuator arrays to determine the exact reasons for these deviations.

The mentioned DNS computations by Vieira et al. [111] indicate increased effectiveness of multiple actuators for TS-wave attenuation within the linear evolution regime. Whereas a second actuator significantly reduces the absolute amplitudes, a third actuator does not add supplementary benefit for flat plate flow at $U_\infty = 10\,\mathrm{m/s}$. This diminishing marginal utility renders large actuator arrays unappealing unless a complete suppression of the disturbance growth can be attained along the surface. The effect of large actuator arrays at very low thrust with minimized power consumption is simulated with the boundary-layer code and analyzed with the stability code. The results of distributed DBD forcing on the generic flat plate setup at $U_\infty = 20\,\mathrm{m/s}$ are presented in Figure 5.6. 26 DBD actuators between $x = 0.33 - 0.58\,\mathrm{m}$ are simulated with 10 mm streamwise spacing to operate at a minimal thrust level of $T = 7.8\,\mathrm{mN/m}$. Downstream of the first actuator location, the resulting N-factor evolution shows almost

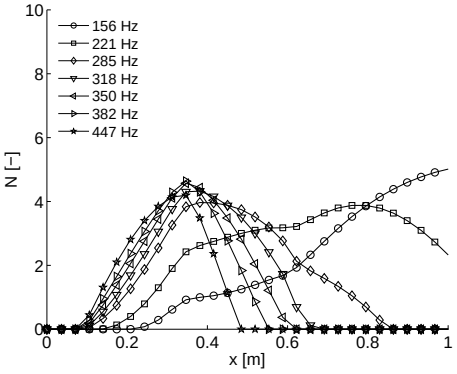

Figure 5.6: N-factor evolution under distributed DBD forcing.

complete suppression of the wave amplitude over a large frequency range and attenuation to subcritical values for frequencies above 200 Hz. Such a configuration is presently not feasible in experiments due to spacing limitations imposed by the electric potential differences, but specialized future DBD actuators may enable spatially continuous thrust generation. If this can be achieved, the flow-control impact can be compared to continuous boundary-layer suction yielding very stable flow conditions [35, 36].

A different approach to optimize the control effectiveness is a numerical sensitivity analysis to find the most sensitive location for flow-control forcing. For such an analysis, an adjoint formulation of the underlying equations is additionally required. Brandt et al. [16] present a stability method to compute the sensitivity of zero-pressure gradient boundary-layer flow to mean-flow forcing. This method considers non-modal disturbance interactions and the results indicate maximum flow sensitivity to time-invariant forcing in streamwise direction between branch I and II of the neutral stability curve (as defined in Figure 2.2). Such results suggest that flow control should be applied within this area to increase the flow-control effectiveness. Additionally it is shown that streamwise forcing, optimized to attenuate Tollmien-Schlichting waves, hardly affects other disturbances modes, e.g. lift-up mechanisms leading to streamwise streaks. A negative effect of the TS-transition control on other disturbance modes is therefore not expected.

A similar sensitivity computation was conducted for a DBD flow-control

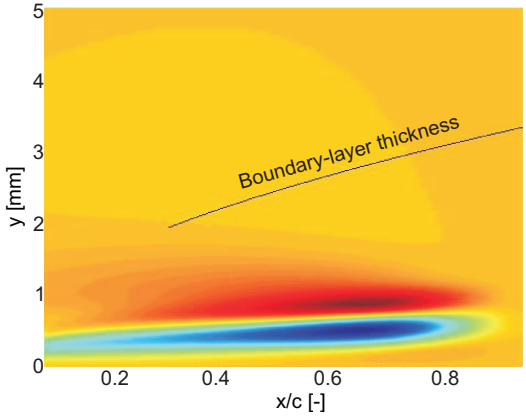

Figure 5.7: Gradient of E_Ω with respect to mean-flow forcing, computations by A. Hanifi based on [16].

application on a flat plate. Figure 5.7 illustrates the gradient of the total energy E across the whole flow domain Ω as a function of the flow-control position. The highest negative gradient (blue) is found close to the surface at the normalized streamwise distance $x/c = 0.685$, indicating the position for best total energy reduction. Adversely, high positive gradients (red) favoring disturbance growth are found at the same streamwise positions but further away from the wall ($y > 1\,\text{mm}$). The force field of DBD actuators with its limited extent in the wall-normal direction appears perfectly suitable to benefit from this sensitivity distribution. The results also indicate that actuation far downstream is more effective than close to the leading edge, which is in agreement with the experimental and numerical position variation results compiled in Table 5.1.

5.4 Stability Analysis of Experimental Data

To validate the stability considerations based on boundary-layer computations, experimentally acquired boundary-layer profiles are analyzed with the linear stability code. The DBD actuator at $x_{\text{DBD}} = 350\,\text{mm}$ is operated at various thrust levels and laser Doppler anemometry provides the averaged velocity profiles 10 mm downstream illustrated in Figure 4.8. The experimental data is converted into an adequate format by scaling the ve-

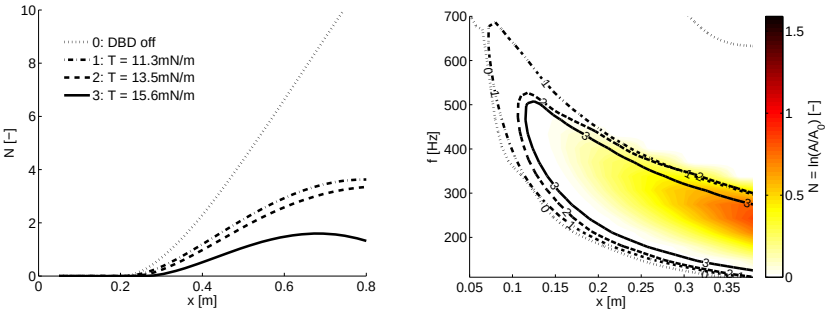

(a) N-factor evolution (b) Neutral stability curves

Figure 5.8: N-factor evolution of a discrete disturbance frequency of 200 Hz (a) and neutral stability curves (b) for DBD thrust variation between $T = 11.3 - 15.6\,\mathrm{mN/m}$.

locity with the freestream speed and the wall-normal distance with the Blasius length scale. Subsequently, the normalized profile is projected in the streamwise dimension by varying the Blasius length scale. This corresponds to an assumption of self-similarity and an analytical variation of the local Reynolds number for the given profile. It is important to note that the following considerations are of purely theoretical nature, since a constant boundary-layer shape along the streamwise direction is assumed, only increasing the boundary-layer thickness according to theoretical scaling laws. In fact, the velocity profile is modified only within a short distance downstream of the actuator. The following considerations can be understood as an approximation of a boundary-layer flow under the influence of repeated actuation, e.g. by an array of plasma actuators. The theoretical amplification of disturbances along the streamwise direction can then be calculated with the linear stability code. The impact of DBD thrust variations is quantified by the growth rate of single disturbance frequencies or in terms of the neutral stability curves, both approaches being visualized in Figure 5.8. Figure 5.8 (a) portrays the predicted N-factor evolution of a modal instability at $f = 200\,\mathrm{Hz}$ under a variation of the actuator thrust. Without DBD operation, the flow under the effect of an adverse pressure gradient is unstable leading to increasing N-factors throughout the whole investigated flow domain. Based on $N_t = 6.14$ used before for the empirical transition prediction, a transition location of $x = 0.6\,\mathrm{m}$ would be expected.

This agrees with the expectations since the flow stability at $x = 0.36\,\mathrm{m}$ is still relatively high and decreases in the downstream direction. Therefore, an analysis based on the single velocity profile automatically yields a postponed transition location compared to the experimental data. If the DBD actuator is operated, attenuation of the growth rates with increasing actuator thrust is observed. This also agrees with expectations since the DBD actuation 10 mm upstream enhances the flow stability and leads to a delayed transition.

Since transition is not initiated by a single frequency disturbance, the analysis of the neutral stability curve is more convenient. Unlike in the boundary-layer computations in Section 5.2, no localized stabilization is observed. Based on the similarity approach, a global influence on the stability is projected, avoiding discontinuities in the neutral curves. Figure 5.8 (b) contains the neutral stability curves for the same DBD thrust levels with the same line styles as in (a). The color levels additionally illustrate the N-factor evolution for the highest thrust case 3. The four neutral stability curves show increasing values of the critical point x_{cr} with increasing thrust. Whereas the critical point is hardly distinguishable without DBD operation, it can be found at $x = 0.072\,\mathrm{m}$ for $T_1 = 11.3\,\mathrm{mN/m}$. At the maximum thrust level $T_3 = 15.6\,\mathrm{mN/m}$, it is delayed until $x = 0.117\,\mathrm{m}$, which corresponds to an increase by 62% compared to the minimum thrust value.

To enable a stability analysis at various locations and to avoid the self-similar scaling approach, fine resolution is required not only of the wall-normal, but also of the streamwise direction. Such measurements would be time consuming, but surely help to further quantify the stabilization impact and its gradient in the streamwise direction. If various thrust levels are additionally incorporated in an extensive study, the dependence on this parameter could also be experimentally quantified. As an additional outcome, force field calculations based on the spatial momentum distribution within the boundary-layer flow could be performed. Such data could be used to quantify the force field variations due to altering flow velocities.

5.5 Design Tool Kit for Flight Experiments

The following task is the application of the obtained insights for the design of a DBD transition control experiment. The wing glove presented in Chapter 3.4 is to be equipped with a DBD actuator for transition control. Power supply limitations restrict the experiment to a single DBD actuator of 600 mm length across the acrylic measurement insert on the glove

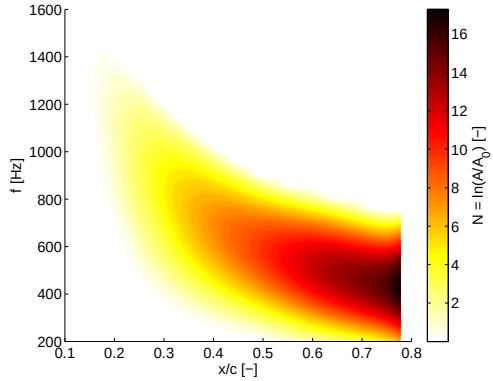

Figure 5.9: Stability diagram of wing glove pressure side, $\alpha = 0.7°$ and $U_{\mathrm{TAS}} = 38\,\mathrm{m/s}$. Contour levels indicate N-factor magnitude.

pressure side. Positioning of this actuator at $x/c = 0.33$ is forseen and the predicted beneficial influence on the transition location by actuation needs to be evaluated.

Earlier flight experiments by Weismüller [114] as well as initial wind-tunnel tests (described in Chapter 6.1) suggest a design angle-of-attack $\alpha = 0.7°$ and corresponding flight speed $U_{\mathrm{TAS}} = 38\,\mathrm{m/s}$ for flow-control experiments. Boundary-layer computations (using a *Xfoil* pressure distribution of the wing glove geometry with these flow parameters) are performed as shown in [56]. In contrast to the considerations in the previous section, the evolution of the boundary-layer velocity profiles along the streamwise direction is correctly reproduced. Nevertheless, the laminar code diverges downstream of $x/c = 0.777$ due to the strong pressure gradient imposed by the reflexed trailing edge, predicting laminar separation. In the experiment, the transition trip or rapid TS wave amplification are expected to trigger transition ahead of this position, which cannot be represented by the numerical method. The results of a linear stability analysis of the flow case are depicted in Figure 5.9. The first amplified disturbance is found at $x/c = 0.12$ for a frequency $f = 1400\,\mathrm{Hz}$ yielding an approximate Reynolds number of $Re_{\mathrm{crit}} = 4.1 \times 10^5$. Mack's relation (3.32) is not directly applicable for airfoil flow under atmospheric conditions due to the influence of pressure gradients and inflow turbulence. Nevertheless, transition N-factors on airfoils between 9 and 11 are typically reported from aircraft

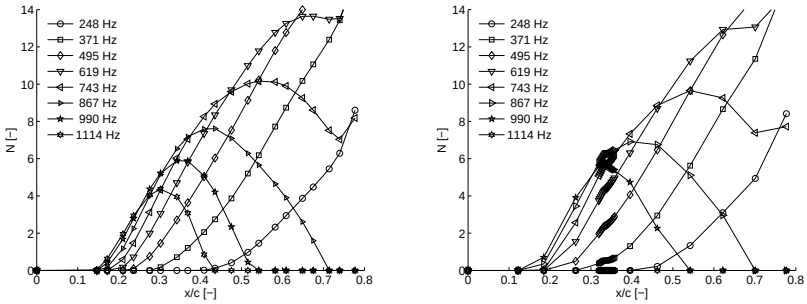

(a) DBD off

(b) $T = 15.6\,\mathrm{mN/m}$

Figure 5.10: N-factor evolution of discrete disturbance frequencies (a) without and (b) with DBD thrust $T = 15.6\,\mathrm{mN/m}$.

flight measurements. A NLF wing glove was tested under atmospheric conditions in flight on a *LFU 205* aircraft [49], reporting approximately $N_t = 10$ from comparisons to stability computations as reviewed by Arnal et al. [7]. If this value is employed for the present and very similar setup, transition is expected at $x/c = 0.485$. For the design of the flow-control experiment, this imposes a limitation on the possible actuator location. Actuator placement in the turbulent region downstream of $x/c = 0.485$ is unlikely to provide any useful effects. On the upstream side, the implemented disturbance source at $x/c = 0.18$ requires a certain downstream distance to develop fully two-dimensional wave fronts. Although the main aim is to control naturally developing transition, a systematic investigation into artificially excited transition should not be made impossible at the design stage. The position $x/c = 0.33$ is a good compromise in the center between the disturbance source and the expected transition location.

The boundary-layer code in connection with the implemented force model and subsequent stability analysis is used to evaluate the impact of actuator positioning at $x/c = 0.33$ on the pressure side of the wing glove airfoil. The N-factor evolution of discrete disturbance frequencies is illustrated in Figure 5.10 (a) without DBD forcing. For comparison, the case of maximized actuator thrusting at $T = 15.6\,\mathrm{mN/m}$ is presented in Figure 5.10 (b). For the flow-control case, the expected critical N-factor $N_t = 10$ is crossed at $x/c = 0.503$, yielding a predicted transition delay of $\Delta x_{\mathrm{trans}}/c = 1.85\%$. Considering the flow speed and the large chord

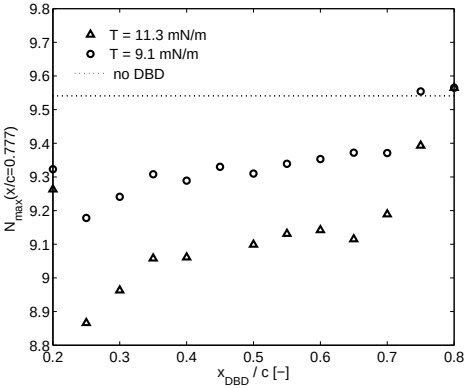

Figure 5.11: Sensitivity of N-factor growth to actuator placement. Maximum N-factor at end of the domain $x/c = 0.777$ for various actuator locations x_{DBD}/c and thrust levels T.

Reynolds number of approximately $Re_c = 3 \times 10^6$, this transition delay corresponding to $\Delta x_{\mathrm{trans}} \approx 25\,\mathrm{mm}$ would be a significant success.

Since the actuator force field can be arbitrarily positioned along the surface of the investigated body in numerical studies, the sensitivity of the flow stability to a variation of the actuator location can be evaluated. A criterion which represents the integral impact over the whole domain as defined in the adjoint-based sensitivity analysis presented in Figure 5.7 is beyond access with the presented method. Alternatively, the maximum N-factor at the end of the domain is evaluated as a function of the actuator placement. The limitation of the boundary-layer code to laminar calculations leads to a prediction of N-factors by the stability code even in the range where fully turbulent flow is expected. DBD forcing positions downstream of the transition location are not sensible, nevertheless the maximum N-factor at $x/c = 0.777$ is taken to quantify the flow-control impact. Figure 5.11 illustrates the results of these computations by comparing the maximum N-factors for different actuator positions and thrust magnitudes. The results recommend a DBD placement at the location $x/c = 0.25$ where the maximum N-factor is minimized. Table 5.2 summarizes the predicted transition locations $x_{\mathrm{trans}} = x(N_t = 10)$ for DBD actuation at the projected $x/c = 0.33$ and the optimal $x/c = 0.25$. The results for various thrust magnitudes and equivalent power consumption are listed, facilitating easy

T [mN/m]	P [W/m]	x_{trans}/c	
		$x_{\mathrm{DBD}}/c = 0.33$	$x_{\mathrm{DBD}}/c = 0.25$
0	0.0	0.485	0.485
7.8	3.7	0.488	0.488
9.1	38.1	0.492	0.493
11.3	45.7	0.497	0.498
13.5	55.1	0.503	0.505
15.6	64.4	0.503	0.506

Table 5.2: Comparison of predicted transition locations for varied thrust and two optional DBD actuator locations, $x_{\mathrm{DBD}}/c = 0.33$ and $x_{\mathrm{DBD}}/c = 0.25$.

comparison of the investigated cases. As the actuator thrust is increased, higher transition-delay predictions are observed for both actuator positions. A saturating trend is observed for elevated thrust magnitudes, limiting the possible transition delay. The overall impact on the transition location by changing between the two actuator locations is negligible in comparison to optimizing the actuator thrust. Based on this observation, the actuator is positioned at $x/c = 0.33$ in the experimental setup due to simplified implementation and cabling.

5.6 Conclusions

A numerical solution of the boundary-layer equations with implemented DBD actuator force distribution shows good agreement with experimentally measured integral boundary-layer properties. The shape factor drop measured close to the DBD actuator coincides closely with numerical simulations based on a finite-difference approximation of the boundary-layer profiles. Linear stability analysis is conducted with the resulting data, suggesting that the local growth rates are decreased for a broad range of frequencies. This implies that the boundary layer is locally stabilized against linear disturbances of such frequencies. Additional adjoint computations show a spatial variation of the flow sensitivity to mean-flow forcing.

The computational results support manifold experimental observations of transition delay with DBD actuators, and validate the experimentally measured dependence of the achievable transition delay on the actuator

position. Under adequate conditions of operation, the imparted momentum locally alters the boundary-layer profiles and increases the hydrodynamic stability of the boundary-layer flow. If the actuator is positioned within the linear disturbance regime, instabilities of all frequencies are damped, maintaining the laminar flow state.

Linear stability analysis shows increased critical Reynolds numbers and an overall diminution of the instability region, based on similarity-scaling of experimental velocity-profile data. A reduction of wave amplification rates confirms the numerical observation of enhanced stability properties under the influence of DBD forcing.

The measured transition locations reported in Chapter 4 correlate well with an empirical e^N-prediction of numerical data under consideration of the measured freestream turbulence intensity. The chosen experimental approach confirms the results of the combined numerical method using a laminar boundary-layer computation together with linear stability analysis. The qualitatively correct transition prediction for varying actuator thrust and position predestine the numerical tool kit for a customized design of DBD based transition control. Nevertheless, additional effort needs to be spent on the problems associated with multi-actuator arrays in the numerical routine.

A flow-control application on a NLF wing glove is investigated, predicting a considerable delay of transition and associated drag reduction. The observed dependence of the flow-control effectiveness on the thrust level as well as the overall agreement with the numerically predicted transition delay are experimentally verified in Chapter 6.

6 Airfoil Experiments

Application of DBD actuators for flow control under realistic scenarios is a prerequisite to enhance the level of maturity of the devices and motivate further research. Wind-tunnel experiments on flat plates and airfoils have so far demonstrated successful transition delay at limited Reynolds numbers. In order to investigate the flow-control impact of DBD actuators under realistic flight conditions, a wing glove is fitted on a G109b motor glider.

Since no experience with flow control on the wing glove configuration (described in Chapter 3.4.2) is available, initial wind-tunnel experiments are conducted to define a suitable parameter space for the following flight experiments. The accessability of the measurement equipment and good repeatability of the flow conditions inside the wind tunnel enable a comprehensive variation of parameters. Before the instrumentation equipment can finally be stored in the underwing pods and on the vibration-isolated platform in the fuselage, a suitable combination of flight speed and angle of attack needs to be identified. The central requirements are that the transition process is observable with the given sensor systems and controllable via the implemented DBD actuator.

Once an opportune configuration is identified, the DBD actuator needs to demonstrate its value under flight conditions. Decreased ambient pressure and temperature with increasing flight altitude under varying humidity change the thermodynamic and aerodynamic properties of the fluid. To maintain constant flow-control authority, it is desirable to obtain a constant forcing of the DBD actuator despite the variable ambient conditions. Therefore, the effects of these variable quantities on the DBD power consumption are identified and a closed-loop controller is developed to ensure equal flow-control impact across the whole flight mission.

Finally, the possible transition delay due to actuator operation is quantified in flight. Prior steps are the accurate determination of the transition location and the identification of error sources of the different sensor systems. This is more arduous to accomplish at 10′000 ft altitude in comparison to the well-defined wind-tunnel conditions, which are described in the following section.

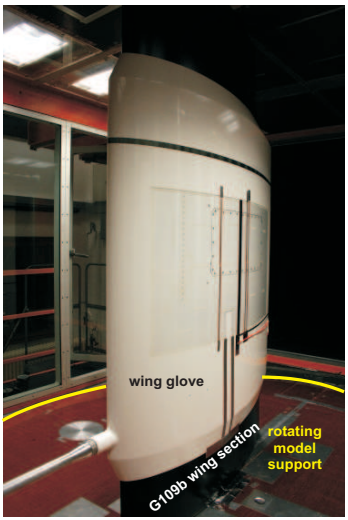

Figure 6.1: Overview of the NLF wing glove, mounted on the G109b support wing section inside the NWK wind tunnel. The rotating model support enables angle-of-attack variations.

6.1 Initial Windtunnel Experiments

The NLF wing glove (presented in Chapter 3.4.2) can alternatively be placed on the glider wing or on a specially adjusted support to fit into the 2.2 m $\times$ 2.9 m test section of the closed-loop *NWK* wind tunnel at TU Darmstadt. The support consists of an original wing section of a G109b glider suited to match the vertical dimension of the wind tunnel and is equipped with a bearing, allowing it to be mounted on a wind-tunnel balance underneath the test section. Although no force measurements are conducted in the current investigation, the balance facilitates rotation of the wind-tunnel model around the vertical axis. For the given setup, this enables an adjustment of the wind-tunnel support angle α_{sup} of the wing glove. A six-bladed fan driven by a 300 kW direct-current motor accelerates the fluid and provides velocities up to 68 m/s downstream of a 1 : 12 contraction nozzle. All steady flight states within the envelope of the glider can be reproduced inside the test section. An overview of the setup is illustrated in Figure 6.1.

The turbulence intensities below 0.1% typically encountered in the atmo-

sphere are not reproducible inside the closed-loop tunnel. Here, they range from 0.4% to 0.5% in the velocity range of $27 - 40\,\mathrm{m/s}$ relevant for the investigated configuration. The fluid density and pressure within the wind tunnel are also mainly defined by the ambient conditions. The same applies to the flow temperature which increases during the measurements due to thermal dissipation of the axial compressor. Although the motor is externally cooled, the flow temperature T_a increases from approximately 10°C to 22°C throughout the day during measurements in the winter season. The thermodynamic properties of the fluid are measured and the speed can be adjusted, i.e. to compensate for a constant Reynolds number. Hot-wire anemometry measures the flow velocities inside the wing glove boundary layer, requiring thorough calibration. Since this measurement technique is particularly sensitive to temperature variations, a temperature correction is applied, compare (3.1).

Due to the geometric angle of incidence of the setup, the true angle of attack α of the wing glove relative to the flow and the support angle α_{sup} deviate by 0.7° which is accounted for by the relation

$$\alpha = \alpha_{\mathrm{sup}} - 0.7^\circ. \tag{6.1}$$

For enhanced comparability to numerical and flight measurements, all data hereafter will be referred to α.

The wing glove and the supporting wing constrict the test section by their mere presence, inducing blockage effects which become more pronounced for elevated angles of attack [114]. Since the experiments reported hereafter cover angles of attack between -1° and $+2^\circ$, the projected model area is in the order of the maximum airfoil thickness of 0.16 m. This yields a blocked area of 5.6% of the total cross section. Neither the overall circulation of the model nor the bulk velocity are decisively influenced. Nevertheless, a small influence on the pressure distributions is noted in comparison to the flight cases. Reynolds-averaged computations of the Navier-Stokes equations (RANS) have been performed by A. Hanifi at Linné FLOW Center, KTH Stockholm, to estimate the effect of wind-tunnel walls on the pressure distribution. Figure 6.2 compares the pressure distributions with wind-tunnel walls and under undisturbed conditions. The wind-tunnel wall effects are negligible as compared to the deviation from wind-tunnel measurements, additionally displayed including experimental error bars. Reasons for the differences between numerics and experiment are uncertainties of pressure tap locations and determination of the correct static pressure inside the wind tunnel. A more detailed discussion of the differences between flight and wind-tunnel measurements with the wing glove setup is

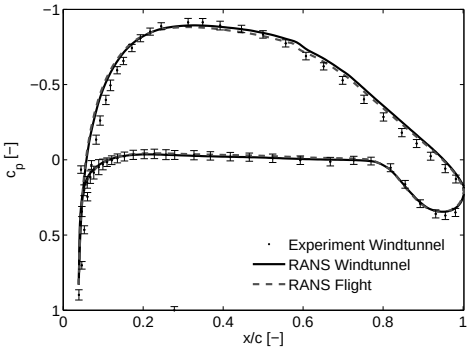

Figure 6.2: Pressure distributions from experiments and RANS computations at $\alpha = 0.7°$.

provided in [114], including the deviations of the lift-drag polar (illustrated in Figure 6.28 for the later discussion on efficiency).

In steady gliding flight, one angle of attack α is coupled to an unique true airspeed U_{TAS} via the necessity to produce lift compensating the actual aircraft weight. The relationship can either be derived from flight performance considerations or from flight measurements with the actual aircraft, the latter approach being chosen here. Figure 6.3 illustrates the relation across the flight envelope for two segments of one measurement flight, indicating measurement uncertainties and a small spread due to fuel-consumption induced weight variation. The variable ambient conditions, discussed in Section 6.2.1, are additional reasons for the small deviations in the data points. The shown relationship implies that the angle of attack and the flow speed have to be adjusted both at a time. This complicates the experimental procedure in the wind tunnel where constant lift is not a prerequisite. Since in the initial wind-tunnel tests only a qualitative estimate for the transition location is strived for, a constant flow speed is selected and the angle of attack is marginally varied around a design point in the order of $\pm 2°$.

6.1.1 Identification of Adequate Transition Locations

To initiate successful flow-control measurements, the most promising flow conditions for transition experiments on the wing glove pressure side is

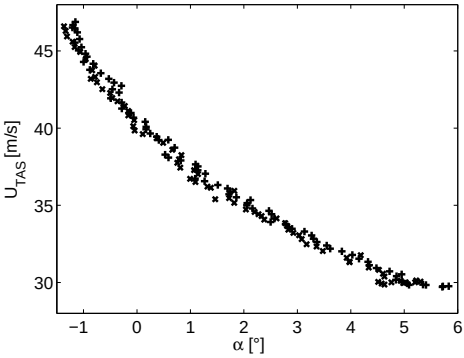

Figure 6.3: Relationship between true airspeed U_{TAS} and true angle of attack α for constant lift, measured during two segments of one measurement flight. Variations are due to different fuel levels and ambient condition deviations.

sought for. Contrary demands pose an optimization problem; low flow speeds are required to retain a sufficient actuator effect due to its limited force field magnitude. On the other hand, low velocities are associated with high angles of attack which lead to a very stable flow on the pressure side. At high angles of attack, transition to turbulence occurs far downstream and is likely to be triggered by the zig-zag tape close to the reflexed trailing edge. If transition occurs too far downstream, a DBD actuator positioned close to the leading edge is unlikely to have an effect on the transition process. A compromise has to be found to ensure hydrodynamic unstable flow and transition locations accessible with the chosen measurement probes.

The transition process along an airfoil is most conveniently analyzed by varying the local Reynolds number $Re_x = U\,x/\nu$. This can be achieved by maintaining the sensor position constant and systematically changing the flow velocity $U = U_{\mathrm{TAS}}$ and the corresponding angle of attack. Alternatively, the flow speed and angle-of-attack are kept constant and the sensor is traversed to several downstream locations x or distributed sensor arrays are employed. It has to be kept in mind that changing the flow state might alter the transition process, such that multiple or relocatable sensors appear more appropriate in flight. In the present investigation, both approaches are pursued and even combined. If a quick overview over

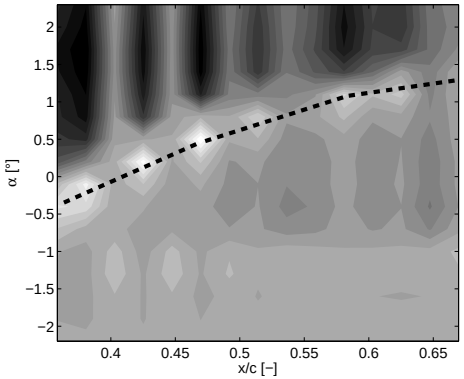

Figure 6.4: Microphone standard deviation related to the angle of attack.

the general transition behavior is desired, measurements with distributed sensors at various positions x in combination with a systematic change of the flow velocity U_{TAS} are advantageous.

The flush-mounted microphone array in the center portion of the measurement insert monitors the level of velocity fluctuation associated with laminar-turbulent transition along the wing glove chord x/c. The contour levels in Figure 6.4 illustrate the streamwise evolution of the microphone signal standard deviation σ_M as the angle of attack is varied between $\alpha = -2.2°$ and $2.3°$ for a constant flow velocity $U_{\mathrm{TAS}} = 38\,\mathrm{m/s}$. Bright colors represent high fluctuation levels, indicative for the flow intermittency during laminar-turbulent transition. By maintaining a fixed velocity and changing the angle of attack of the model, the pressure gradient on the pressure side is varied and the resulting displacement of the standard deviation peak is quantified. The dashed line, approximating the evolution of the maximum standard deviation, clearly shows that the transition location can be adjusted within the measurement region $x/c = 0.35 - 0.67$ for varying angles of attack $\alpha = -0.2 - -1.3°$. The initial parametric study yields an angle of attack of $\alpha = 0.7°$ as most promising to obtain the boundary-layer transition approximately in the center of the exchangeable measurement insert. For this design angle and the corresponding flow speed $U_{\mathrm{TAS}} = 38\,\mathrm{m/s}$, maximum intermittency is obtained at $x/c = 0.51$ at the 8^{th} microphone position. The local Reynolds number at this position is $Re_x = 1.7 \times 10^6$.

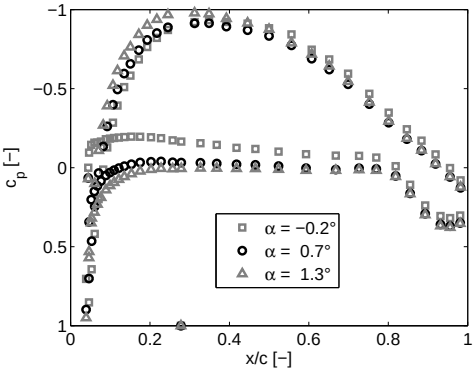

Figure 6.5: Dimensionless pressure distribution for varying angles of attack at constant speed $U_{\mathrm{TAS}} = 38\,\mathrm{m/s}$.

The pressure distribution at $U_{\mathrm{TAS}} = 38\,\mathrm{m/s}$ and varying angles of attack $\alpha = -0.2 - 1.3°$ is illustrated in Figure 6.5. The dimensionless pressure coefficient c_p along the streamwise chord position x/c characterizes the pressure gradients on the suction and pressure side of the wing glove. For $\alpha = -0.2°$, a strong positive gradient of $\mathrm{d}c_p/\mathrm{d}(x/c) = 0.23$ is found on the pressure side in the relevant region $x/c = 0.2 - 0.7$, indicating highly unstable conditions. Under such low angles of attack, transition is expected to occur close to the position of the DBD actuator at $x/c = 0.33$, and evidence can be found in Figure 6.4 through the microphone data. At the higher $\alpha = 1.3°$, the pressure gradient is approximately neutral ($\mathrm{d}c_p/\mathrm{d}(x/c) = 0.01$), leading to a much higher flow stability and postponed transition. For the design angle of attack $\alpha = 0.7°$, the dimensionless pressure gradient $\mathrm{d}c_p/\mathrm{d}(x/c) = 0.09$ is only slightly destabilizing the flow. Under such conditions, DBD flow control is effective for transition delay as shown in the following.

6.1.2 Quantification of Transition Delay

After having found an adequate setup such that transition occurs on the exchangeable acrylic insert and is measurable with the sensors, the transition control experiments are initiated. The primary objective of the following wind-tunnel tests is to identify DBD actuator configurations to effectively control the transition.

Although arrays consisting of multiple actuators have shown to be very effective in delaying transition on a flat plate, a reduction of complexity is gained if only a single DBD actuator is applied. Thorough investigations of a reduced parameter set decrease time consumption and the obtained insights are a necessary prerequisite for further enhancements. Owing to power supply limitations and ease of mechanical implementation, a single DBD actuator is placed at $x/c = 0.33$. This position was numerically investigated in Chapter 5.5 to ensure effective transition control.

As expected, application of the single DBD plasma actuator leads to a downstream shift of the transition process. This can be quantified either by integral boundary-layer quantities like the shape factor H_{12} or the standard deviation of a sensor signal. All these values can be evaluated with a single hot-wire probe which is traversed with the 3-axis boundary-layer traverse described in Chapter 3.4.6. The hot wire enables acquisition of averaged boundary-layer velocity profiles as well as a statistical analysis of the anemometer signal. Figure 6.6 illustrates the effect of DBD actuation on the standard deviation σ_U of the velocity, acquired by a hot wire. The sensor is positioned at the wall ($y = 0\,\mathrm{mm}$) and traversed in streamwise direction x along the chord c. The peak of the signal fluctuation, encountered during maximum intermittency of the flow between the laminar and turbulent state, is found at $x/c = 0.47$ without DBD actuation for an angle of attack of $\alpha = 0.7°$ and slightly downstream ($x/c = 0.5$) for the less unstable $\alpha = 0.8°$. With DBD actuation, these positions are moved downstream, to $x/c = 0.5$ for $\alpha = 0.7°$ and even outside the observation region for $\alpha = 0.8°$. Although these results show a first and very successful delay of transition at large Reynolds numbers, measurement uncertainties impede an exact quantification of the actuator impact. Therefore, other quantities are investigated to validate the observations.

The shape factor H_{12} of the boundary-layer profile is illustrative for the transition process by combining the trends of the displacement thickness δ_1 and the momentum loss thickness δ_2. The shape factors of the same cases investigated before are illustrated in Figure 6.7, all showing a negative slope which is indicative for the ongoing transition. Despite data scatter and ambiguous detection of the wall position, the solid lines without DBD operation are set off from the dashed lines (indicating the flow-control cases). If the chord positions of two cases are evaluated for the same shape factor, e.g. $H_{12} = 1.8$, an offset by approximately $\Delta x/c = 0.03$ is observed. This value agrees quantitatively with the offset observed in the signal standard deviation in Figure 6.6.

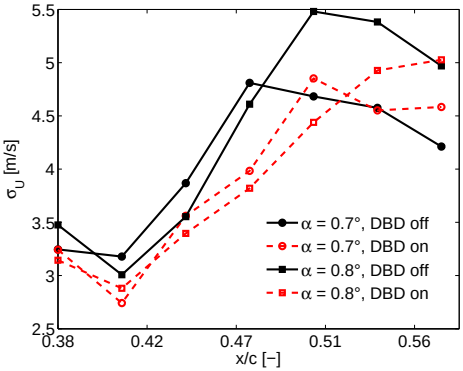

Figure 6.6: Standard deviation of hot-wire signal σ_U at the wall for various downstream locations x/c. The peaks indicate the maximum flow intermittency which is representative for the transition process.

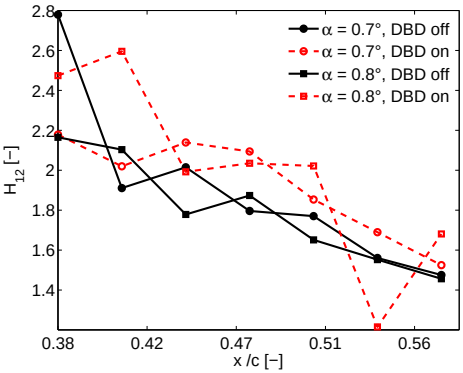

Figure 6.7: Shape factor H_{12} of the boundary layer as a function of the streamwise position x for two different angles of attack α.

The measured offset of both quantities translates into a physical transition delay of approximately $\Delta x_{\text{trans}} = 40\,\text{mm}$. This is far less than the gain on the flat plate reported in Chapter 4, but exceeds the expectations of $\Delta x_{\text{trans}} \approx 25\,\text{mm}$ based on the numerical tools used in Chapter 5.5. The experiments are very successful considering the high freestream velocity and the pronounced adverse pressure gradient. The determined combination of angles of attack and flow speed is promising for further investigation in flight.

Unfortunately, the microphone array is not helpful for the evaluation of the transition delay in the wind tunnel. For $\alpha = 0.7°$, the peak of the microphone standard deviation σ_M at $x/c = 0.58$, indicated in Figure 6.8, quantitatively disagrees with the hot-wire readings presented in Figure 6.6. Additionally, DBD actuation does not produce any significant difference in this position, leading to the conclusion that wind-tunnel noise and the coarse spacing of reliable microphones limits the chances of acquiring the correct transition location. Despite various approaches to correctly calibrate the microphone array as described in Chapter 3.4.4, 7 sensors did not provide sufficient signal-to-noise ratio under the conditions of wind-tunnel operation and were excluded from the data postprocessing. This becomes visible by the coarse resolution of only 8 data points in streamwise direction in Figure 6.8. The problem possibly derives from variant sensitivity of the microphones stated by the manufacturer ($10\,\text{mV/Pa}$ $\pm 2.5\,\text{dB}$) or clogged surface orifices. Only after completion of the wind-tunnel tests, all microphones could be revised and the surface connection reestablished. During the flight measurements presented in Section 6.3 similar problems occurred, indicating that the sensitivity of single microphones was too low to provide useful data. In the aftermath of the experiments it was found out that the sealing between the inaccurate microphones and the surrounding acrylic was not airtight, effectively increasing the air volume and reducing the signal accuracy.

Neither the functional microphones nor the hot-wire data reveal the frequencies involved in the transition process. Fourier transformations of all hot-wire and microphone measurements primarily reveal the disturbance frequencies introduced by the wind tunnel. A broadband spectrum, illustrated in Figure 1.1, is audible even outside the test section during wind-tunnel operation. The propulsion additionally causes periodic flow fluctuations, visible in the two low-frequency peaks of the solid curve in Figure 6.9, representing the frequency spectrum of the microphone signals between 20 and 2'000 Hz. The 63 Hz peak and its 21 Hz subharmonic origi-

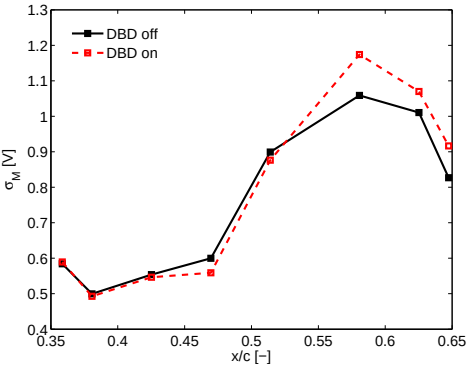

Figure 6.8: Standard deviation of the microphone signals σ_M at a fixed angle of attack $\alpha = 0.8°$.

nate from the blade passing of the six-bladed rotor inside the wind tunnel. Measurements at various speeds confirmed a dependency of these frequency peaks on the rotatory speed of the motor. The same peaks at are found in the hot-wire data (dashed line) at worse frequency resolution. The lower amplitudes of the peaks indicate towards an acoustic source since the hot wire is less sensitive to minute pressure fluctuations.

Despite problems with the microphone array and high acoustic disturbances inside the wind-tunnel flow, a suitable setup and parameter range for flow-control experiments is identified. A delay of transition by approx. 40 mm or 3% chord is achieved without further optimization. In the next step, the setup is mounted on the G109b glider wing to perform transition delay experiments in flight, based on the identified parameters. Before these measurements can be successfully performed, some constraints of in-flight experiments need to be addressed.

6.2 Constraints of Flight Operation

The flight conditions pose the problem of identifying the correct angle of attack. Unlike in the wind-tunnel experiments, no geometric angle can be measured or defined but the angle of attack α_{FL} is available from the *Dornier Flight Log* wind vane, introduced in Chapter 3.4.4. Since the geometric angle of incidence of the vane relative to the glove chord is difficultly

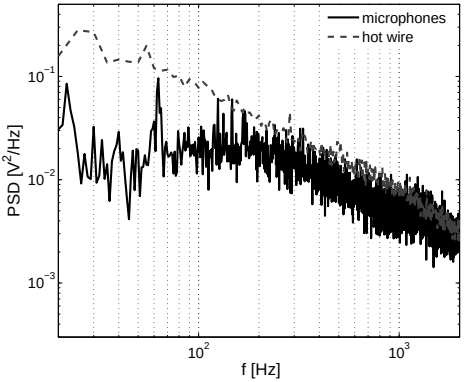

Figure 6.9: Power spectral density of hot-wire signals across the boundary layer (dashed) and microphone signals along the chord (solid).

measurable and the induced angle of attack α_i depends on the actual angle of attack α, a constant offset cannot be expected and a calibration is necessary. Weismüller [114] presents a calibration of the device by comparing pressure measurements in flight to numerical data. The pressure distribution over the wing glove measured during flights at constant α_{FL} is compared to a variety of two-dimensional flow calculations with *Xfoil* at different α_{2D}. A least-square-fit of the finely resolved pressure data yields a reference between both angles. The same approach is chosen for the present setup and data from calibration flights composes Figure 6.10. The almost linear relationship between the measured α_{FL} and $\alpha = \alpha_{2D}$ is expressed by the relation

$$\alpha = 0.725 \cdot \alpha_{\mathrm{FL}} - 0.747^{\circ}. \tag{6.2}$$

Again, all flight data will be related to α for comparability with wind-tunnel measurements and numerical results.

Lissajous figures composed of the supply voltage and the charge across a monitor capacitance describe the DBD power consumption as illustrated in Figure 3.3. In order to precisely evaluate the power consumption, it is not sufficient to sample these data at twice the plasma operating frequency. The Lissajous figure is highly sensitive to subtle variations of the exact shape and phase lag of the periodic signals, requiring acquisition in the MHz range. On ground, these quantities can be acquired using a digital oscilloscope *Tektronics TDS 3032C* at sampling rates of up to 300 MHz. Size and

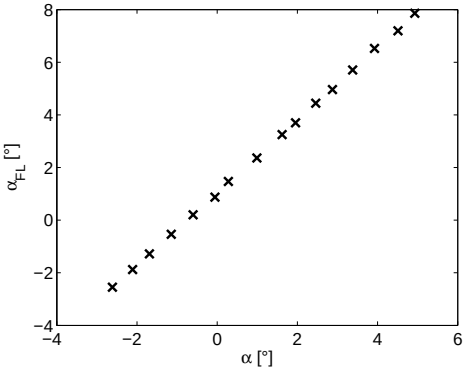

Figure 6.10: Functional relation between measured Flight Log angle of attack α_{FL} and fitted 2D angle of attack α.

weight limitations as well as automatization demands prohibit the use of such oscilloscopes during measurement flights. The available *National Instruments 9074 cRIO* with various analog-digital converter modules cannot be used for this task since the high sample rate would impose unnecessary data density and performance requirements on the full flight data acquisition. Instead, a computer based digital oscilloscope *Picotech PicoScope 4424* is connected via USB to the flight computer to sample two channels at 1 MHz independently from the remaining data acquisition at 16 kHz. The *LabView* environment facilitates the implementation of manifold acquisition hardware and synchronized data recording.

Before the effect of DBD actuation on the flow can be quantified, the influence of the experimental conditions on the gas discharge requires consideration. A deterioration of DBD performance due to increasing flow velocities has been reported [61, 70], and similar influences of pressure and humidity have been investigated [10, 11]. The ranges of the ambient conditions, including the flight speed encountered during the measurements, are summarized in Table 6.1. The table is divided into parameters with dependence on the actual flight altitude and independent quantities. The dependence between altitude, pressure, density and temperature is expressed by the definition of the International Standard Atmosphere [50]. Functional relations between these parameters provide a reference frame for aviation measurement techniques, e.g. to calculate the altitude from static pres-

Altitude	A	$10'000$	-	0	ft
Pressure	p	0.7	-	1	bar
Density	ρ	0.86	-	1.3	kg/m^3
Temperature	t	-20	-	30	$°C$
Velocity	U_∞	20.3	-	44.5	m/s
Turbulence intensity	Tu	0.02	-	0.5	%
Relative humidity	h_{rel}	10	-	100	%

Table 6.1: Ambient conditions during measurement flights, divided into altitude dependent (top) and independent (bottom) quantities.

sure data. Although non-standard conditions are typically encountered in the atmosphere, the physical relations maintain their validity. They will not be reviewed in detail but are exemplified by the ordering within the table. With decreasing altitude, the pressure, density and temperature increase. The remaining factors are not functionally related to the altitude but depend on the flight state and the weather.

In the past, several experimental investigations have aimed at mimicking flight conditions relevant for commercial aviation industry, in order to evaluate DBD actuator efficiency under such circumstances. Laboratory setups lack the simultaneous agreement of all relevant quantities with realistic conditions. The separated investigation of single parameter effects is commendable, but parametric studies have revealed effects which are partially contradictory under flight conditions. Although only flight experiments with DBD actuators and simultaneous acquisition of ambient conditions enable a comprehensive discussion of the net impacts, several parametric studies will be reviewed in the following.

Bénard and Moreau [8] investigate the decrease of pressure, temperature and density associated with an altitude increase and identify the pressure to have the most prominent effect on DBD operation. With increasing altitude, the maximum velocities induced by a DBD actuator in quiescent air are reduced. At the same time, the power consumption and extension of the plasma along the surface increase.

Due to the primary importance of the pressure, several researchers concentrate on the corresponding effect on the actuator performance. In general, increasing power consumption is found for decreasing pressure [1, 58], but conflicting observations are made concerning the flow-control authority. Either linear [42] or non-linear dependencies between ambient pressure and

the actuator thrust [1, 105, 107], induced mass flow [9] or maximum induced velocities [118] are derived. Others [110] describe a monotonic dependence of ionization and plasma extent for pressures beyond 1′000 mbar which are irrelevant for testing under atmospheric conditions. The effectiveness of DBD forcing at pressure levels summarized in Table 6.1 remains ambiguous since several authors identify peaks of the investigated quantities at differing pressures. Notwithstanding, the sensitivity of the gas discharges towards pressure changes causes Chartier et al. [20] to suggest the application of DBD as pressure sensors. The referred investigations show the importance of controlling either the pressure or the actuator performance if a constant flow control output is desired. Only the latter is achievable for atmospheric flight experiments and is described in Section 6.2.2.

The temperature effect has largely been neglected, systematic investigations mainly concentrate on the impact of temperatures above the range of interest (e.g. for $30° < T_a < 200°$ in [110]). Nevertheless, the findings forebode that for the ambient temperatures and small variations found in the flight experiments, a significant impact is unlikely.

The flow velocities encountered in flight have an additional impact on the actuator performance. The impact of a velocity variation on the power consumption reported by Kriegseis [58] suggests a linear dependency although the data shows significant spread below 50 m/s. Under transonic conditions, Pavon et al. [76] identify an impact of the actuator placement since the velocity and pressure field experience drastic spatial variations. During most of the flight tests presented in Section 6.3, the pressure distribution and the flow velocity are kept as constant as possible to maintain a steady flight state. Only at steady flow conditions, the effect of the actuator can be appropriately identified with the sensor equipment. The flight experiments are conducted during the early morning when the air is as calm as possible. Only in the absence of thermals a desired flight state can be maintained to ensure repeatability. For these experiments, neither velocity variations nor turbulence are expected to provoke undesired actuator performance variations.

The relative humidity ϕ is the ratio between the partial pressure of water vapor e_w and the saturated vapor pressure e_w^* and therefore depends on the temperature as well as the ambient pressure. This quantity is macroscopically defined by the weather situation but locally dependent on the altitude. The formation of clouds indicates saturation ($\phi = 100\%$), and flight through clouds is expected to provoke large humidity gradients. Anderson and Roy [4] perform a variation of the air humidity in a small range

between $\phi = 43 - 53\%$ and find increasing DBD flow-control effectiveness for higher humidity. Nevertheless, the authors themselves stress the preliminary character of the study and suggest thorough validation. Subsequently, Bénard et al. [11] experience a non-monotonic behavior of humidity variation on the power consumption: between $\phi = 0.4 - 0.6$, the power consumption increases, for $\phi = 0.6 - 0.85$ it decreases and grows again between $\phi = 0.85 - 1$. The increase at high humidity levels is explained by local deposition of water droplets and the resulting modification of the conductance on the surface. Finally, a reduction of the induced velocities and mass flow rate at high humidity levels is reported which can be overcome by adjusting the supply voltage. The important possibility to compensate for these control authority variations enables closed-loop control of the actuator impact. The monotonic relation between the force produced and the power consumed by a DBD actuator reported by Kriegseis et al. [59] enables the evaluation of the actuator control authority by electrical power measurements and feedback adjustments to maintain it constant. Since the monotonic relation was evaluated during constant ambient conditions, a thorough experimental study of the force and power under varying conditions is highly recommended but beyond the experimental possibilities of this project.

To summarize, the pressure and humidity of the ambient air have a significant impact on the performance of DBD flow control. These single quantities have to be monitored during all flight experiments and a quantification of the combined impacts is presented in the next section.

6.2.1 Quantification of Ambient Condition Influences

A comprehensive study of the isolated effects of the single parameters on the DBD performance cannot be conducted in flight. Such an investigation is beyond the scope of this work since usually a combination of parameters varies either independently or with mutual dependence. Nevertheless, under some conditions, a predominant effect by one parameter can be identified which will subsequently be discussed. In order to evaluate the effects of the ambient condition on the power consumption of a single DBD actuator, the control voltage fed into the *MiniPuls 2.1* supply is kept constant. Under steady conditions, a constant high voltage amplitude is provided and the power consumption does not change over time. For the presented experiments, the single DBD actuator is operated at the resonance frequency $f_{pl} = 7.8\,\mathrm{kHz}$ of the actuator combined with the power supply to achieve maximized electrical efficiency.

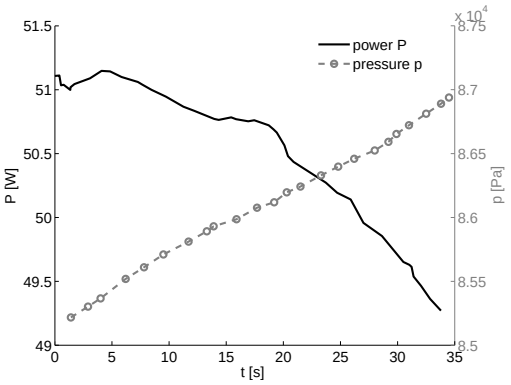

Figure 6.11: Power variation during pressure increase in gliding flight. The abscissa illustrates the measurement duration in seconds.

The typical flight procedure for flow-control experiments (reported in Section 6.3) is a motorless gliding descent starting from 10′000 ft altitude. The descent rate depends on the flight velocity chosen for the measurement, and the actual altitude is calculated from pressure measurements. The static pressure from the ambient air data system is indicated in Figure 6.11 during a typical measurement flight, showing increasing pressure during the descent. Due to the atmospheric dependence between temperature and pressure, the temperature also increases slightly. The above described domination of the pressure influence on DBD performance renders the small temperature increase of approximately 1° C negligible. The air humidity during this specific flight remains almost constant at $67\% \pm 2\%$ whereas the momentary power consumption is illustrated to derive the dependence between the pressure and DBD power consumption. The trend of decreasing power consumption with increasing pressure agrees well with the observations in [1, 8, 58]. A 3% pressure increase leads to a 4% decrease of the consumed power, Kriegseis [58] also reports a linear dependence in the order of 1.

Air humidity is the next important parameter under investigation. A horizontal, motor-powered flight is conducted to remove the influence of pressure changes while flying through air layers of varying humidity beneath the cloud base level. A strong humidity variation by 30% is contrasted to the power consumption in Figure 6.12. Due to saturation and condensation

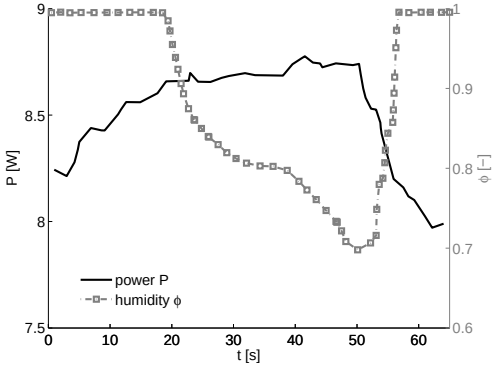

Figure 6.12: Power modification due to humidity variation.

on the surface, the humidity reads 100% at the beginning and the end of the flight segment. This cannot be resolved by the sensor but strongly influences the power consumption as also reported by Bénard et al. [11]. A gradient of the power consumption is therefore also found in regions of saturated, constant humidity. The power variation is in the order of 5% for a 30% humidity change.

Obviously, the relative sensitivity of DBD performance towards humidity gradients is minor than for pressure changes. Nevertheless, the pressure decreases slightly but continuously during the measurement flights, whereas strong humidity gradients can occur instantaneously. During regular atmospheric flights both influences can couple and additional, unpredicted effects may lead to DBD performance variation. Therefore, a closed-loop control of the actuator power is desired to maintain a constant performance during flow-control measurements. The following section introduces the concept and shows the successful application of a closed-loop control algorithm in the free-flight experiments.

6.2.2 Closed-Loop Performance Control

A necessity for real-time feedback control is adequate processing time of input and output signals. The *National Instruments 9074 cRIO* real-time module enables fast data acquisition and can even perform simple algorithmic operations on a FPGA level. In principle, the Lissajous-based power

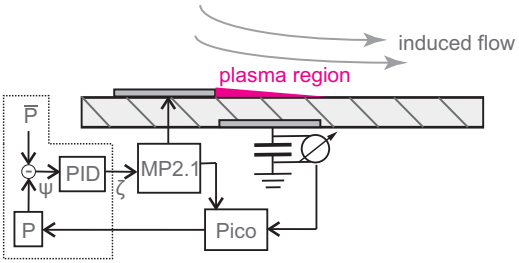

Figure 6.13: Sketch of the closed-loop power control setup including PID controller, *MiniPuls 2.1* (MP2.1) and *PicoScope* (Pico).

measurements provide a value for the consumed power for every plasma cycle, i.e. at 7.8 kHz. Averaging of several cycles is recommended due to measurement uncertainties and still provides power data at a sufficient rate to compensate ambient condition variations in a frequency range of 10^{-1} Hz.

The *LabView* based real-time data acquisition facilitates the implementation of a control algorithm for the DBD performance. A feedback controller allows a comparison between the measured (P) and the target ($\bar{P}$) power value under any flight condition. The *National Instruments NI 9263* digital-analog output module closes the loop and sends a control signal ζ to the *MiniPuls 2.1* power supply to adjust the operating voltage. The principal setup of a closed-loop control circuit for the DBD power surveillance is illustrated in Figure 6.13.

A PID architecture is chosen for the software implementation of the control algorithm. An available *LabView* PID subroutine is implemented in a loop structure to iteratively process the incoming data. The PID controller comprises a combination of proportional, integral and differential processing of the input signal ψ to determine a suitable output signal ζ.

$$\zeta = k_p \psi + \frac{1}{T_i} \int \psi dt + \frac{1}{T_d} \frac{\mathrm{d}\psi}{\mathrm{d}t} \tag{6.3}$$

While the dynamics of the controller are largely determined by the proportional and differential components, integration avoids any permanent control offset. The parameters k_p, T_i and T_d need to be adjusted such that the power consumption is stably maintained over a wide range of power levels $\bar{P}$ while optimizing the dynamic behavior. Analytical or empirical methods are applicable to specify proper parameter combinations. For

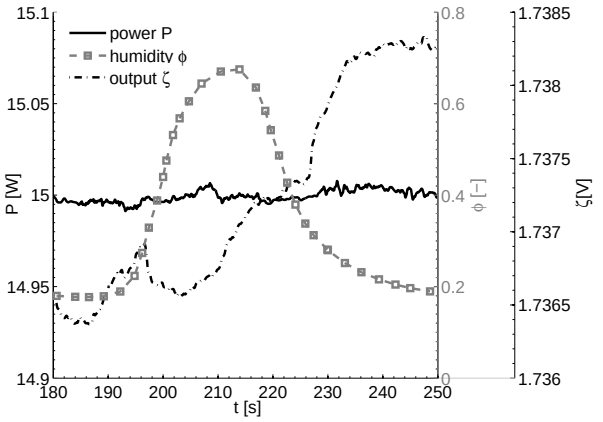

Figure 6.14: Closed-loop control of actuator power during humidity variation.

analytical approaches, the transmission behavior of the complete control circuit needs to be known. Derivation of a model or system identification are time consuming and avoided because the empirical Ziegler - Nichols method [120] quickly revealed suitable parameters. A differential component was not necessary and only increased overshooting in case of abrupt changes of the reference power $\bar{P}$. Hence, a suitable PI-combination is found in $k_p = 0.011895$ and $T_i = 0.006199$ applied in all following flight measurements.

Flight tests were performed to evaluate the operability of the power controller under varying conditions. Figure 6.14 illustrates measurements while crossing beneath a cloud base in motorized horizontal flight. The humidity increases significantly and the controller output is adjusted while maintaining the power constant at $P = \bar{P} = 25\,\mathrm{W/m}$. During the gliding flow-control flights reported in the following section, no such abrupt changes of the ambient conditions occur since these are performed either above or far from clouds. Nevertheless, the aptitude of the controller to level out different target powers under varying conditions needs to be demonstrated. Figures 6.15 (a) and 6.15 (b) indicate the maintained $\bar{P} = 34.5\,\mathrm{W/m}$ and $\bar{P} = 69.2\,\mathrm{W/m}$ power levels relevant for transition control reported in the following section. Despite varying ambient conditions during the gliding

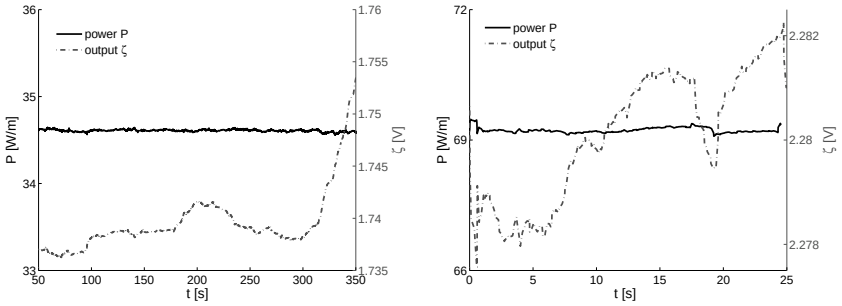

(a) $\bar{P} = 34.5\,\mathrm{W/m}$ (b) $\bar{P} = 69.2\,\mathrm{W/m}$

Figure 6.15: Closed-loop control of actuator power at different power levels.

flight (noticeable through the slight adjustments of the controller output ζ) the power level remains almost constant for both cases with a maximum deviation of $0.5\%\,\bar{P}$.

6.3 Transition Delay in Flight

In order to correctly quantify the impact of DBD flow control on transition, a steady flight state must be maintained. Several possible error sources require consideration for flight measurements. Small angle-of-attack or slip angle variations, vibrations or acoustic excitation can alter the transition location on the wing glove.

To reduce the probability of such disturbances, all measurement flights are performed with the motor turned off in quiescent air early in the morning. After climbing to an altitude of $10'000\,\mathrm{ft}$ the motor is turned off and the propeller rotated to a minimum resistance position. The pilot approaches the selected angle of attack and ensures steady conditions before the measurement is started. At a minimum altitude of $3'500\,\mathrm{ft}$, the measurement is stopped, the motor is turned on again and the next climb can be initiated.

Any abrupt control input by the pilot excites dynamic eigenmodes of the aircraft movement. Two of the most important eigenmodes are the short period mode and the phugoid. The short period mode comprises strong angle-of-attack modulations but is highly damped and does not play a significant role. The phugoid provokes an exchange between potential and kinetic energy, leading to periodic changes of the flight speed and altitude

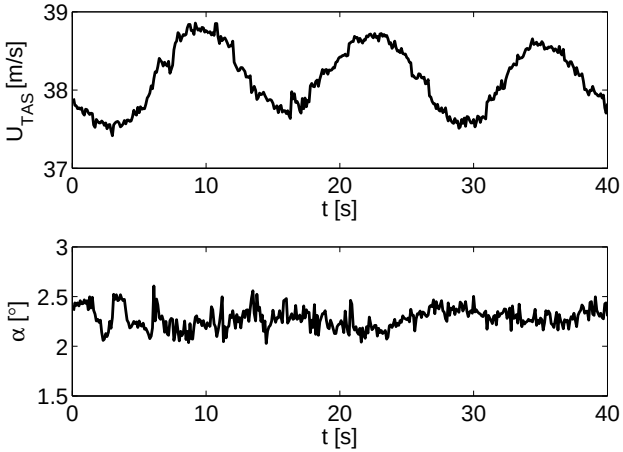

Figure 6.16: Phugoid eigenmode in measurement signals.

at almost constant angle of attack. The damping rate of the phugoid mode is inversely proportional to the high lift-to-drag ratio of the glider aircraft, because of which it cannot be neglected. The period of the phugoid is in the order of $13-14\,\mathrm{s}$, both visible in Figure 6.16 measured at an angle of attack of $2.3°$ as well as confirmed by *AVL* computations. A slightly damped oscillation of the speed is observed for a constant angle of attack. For the flight experiments this means that a low-pass filtering (below $0.1\,\mathrm{Hz}$) of the velocity data is necessary. After abruptly changing the flight state, $3-5\,\mathrm{s}$ seconds are necessary before the next measurement may be initiated to allow for sufficient damping of oscillations. Therefore, constant angles of attack are preferred and applied during most of the measurement flights.

Alternatively, a continuous change of the angle of attack leading to a constant acceleration or deceleration may be beneficial to quickly characterize the transition process. If the angle of attack is continuously changed at a rate below $|\dot{\alpha}| \leq 0.1°/\mathrm{s}$, the aircraft does not experience excitation of an eigenmode and the flight state can be considered quasi-steady. Figure 6.17 (a) shows the standard deviation of a single hot-wire signal close to the wall during acceleration ($\dot{\alpha} < 0$) and subsequent deceleration ($\dot{\alpha} > 0$). For both signals shown in the plot, low values are found at high angles of attack, depicting laminar boundary-layer flow due to the stable pressure conditions. At sufficiently low angles of attack, the boundary layer tran-

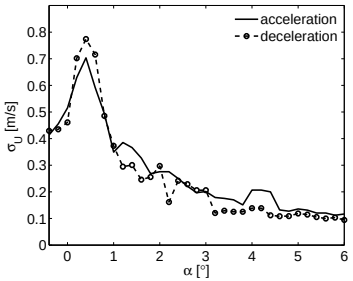

(a) Hysteresis of hot-wire signal during acceleration and deceleration.

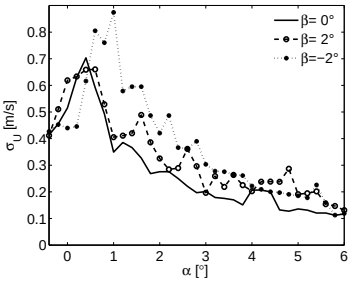

(b) Influence of the sideslip angle β.

Figure 6.17: Hotwire signal standard deviation at the surface at $x/c = 0.38$ for variation of the angle of attack.

sitions and exhibits the intermittency peak at $\alpha = 0.4°$. The transition is characterized congruently for both the acceleration and the deceleration and no hysteresis is found. It can be concluded that the flight state is quasi-steady and boundary-layer transition is not influenced by dynamic effects.

In a similar manner, the effect of slip-angle variations on the transition process is investigated. Apart from angle-of-attack variations due to the phugoid, pilot commands or wind gusts, excessive slip angles also influence transition. For negative slip angles, the sting mounted in front of the wing glove sheds vortices onto the leading edge. The $\beta = -2°$ case in Figure 6.17 (b) shows intermittency at higher angles of attack as compared to the neutral or positive slip angle. This illustrates the promotion of transition due to the sting interference and suggests to perform flights rather at positive slip angles β.

6.3.1 Microphone Measurements

In the following, measurements at a constant angle of attack are described while observing sensor signals at different positions. The available wall-mounted microphone array enables synchronized measurements at 8 locations distributed in streamwise direction. The problems with 7 of the originally 15 microphones, encountered during wind tunnel operation and described in Section 6.1, could not be solved before the start of the flight

campaign such that the data of these sensors was not post-processed. Despite the reduced spatial resolution, the boundary-layer state can quickly be evaluated by considering the signal spectra as in Figure 6.9. If the spectral amplitudes of frequencies f are visualized for each streamwise sensor position x/c in a contour level plot, Figure 6.18 (a) is obtained. The ordinate shows the streamwise microphone positions whereas the frequencies are found on the abscissa. Red illustrates high amplitude levels whereas low amplitudes are blue. For $\alpha = 0.7°$ and without DBD operation, laminar flow is found at streamwise locations up to approximately $x/c = 0.47$, indicated by low disturbance amplitude levels. Only a confined range of higher amplitudes exists around $f = 600 - 800\,\mathrm{Hz}$, which represents the amplifying Tollmien-Schlichting instabilities. A broadband increase of disturbance magnitudes associated with transition to turbulence occurs downstream of $x/c = 0.47$. This transition location agrees well with the wind-tunnel microphone measurements, illustrated in Figure 6.4. The effect of the single DBD actuator operated at controlled $P = 66.6\,\mathrm{W/m}$ and corresponding $T = 16.2\,\mathrm{mN/m}$ becomes apparent in Figure 6.18 (b). A delay of the transition is indicated by further downstream occurrence of the broadband amplitude increase around $x/c = 0.5$. Due to the coarse microphone spacing, a correct quantification of the transition delay is difficult, but interpolation forebodes approximately 3%. These results show the first successful DBD transition delay performed in flight under atmospheric conditions.

A variation of the actuator thrust and power shown in Figure 6.19 enables efficiency optimization to find the highest possible transition delay at the least necessary power consumption. At constant experimental conditions of $\alpha = 0.7°$, increasing DBD power consumption leads to a downstream propagation of the transition line. A limit is reached at $x/c = 0.5$ for $P = 66.6\,\mathrm{W/m}$ beyond which no further effect can be noticed but energy expenditure increases. This confirms the numerically predicted saturation of the actuator effectiveness presented in Table 5.2. In addition to unnecessary energy waste, higher power consumption and associated voltage amplitudes can lead to premature deterioration of the dielectric material. Based on these results it is advantageous to continue the flow-control experiments at a nominal thrust of $T = 16.2\,\mathrm{mN/m}$ and power consumption of $P = 66.6\,\mathrm{W/m}$.

The low disturbance conditions in flight favor measurements without installation of the obstructive hot-wire traverse. To quantify the influence of the traverse on the transition location, the traverse is removed and microphone measurements are performed. Figure 6.20 (a) indicates the transition

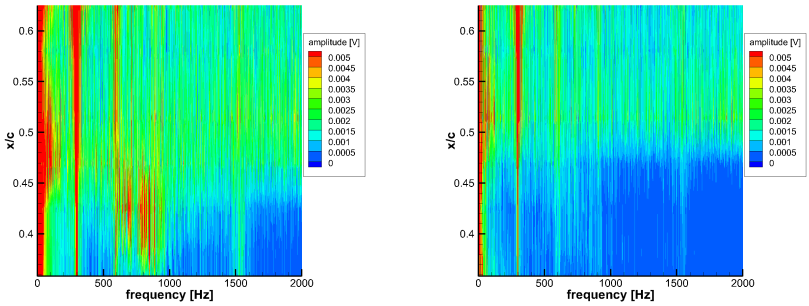

(a) DBD off

(b) DBD on

Figure 6.18: Spectrogram of microphone signals for $\alpha = 0.7°$, traverse system installed, DBD on/off at $T = 16.2\,\mathrm{mN/m}$ ($P = 66.6\,\mathrm{W/m}$). Low signal amplitudes indicated in blue, high levels in red.

evolution at the same angle of attack as for the measurements with traverse from Figure 6.18. If only the measurements without flow control are considered, the results indicate that the removal of the traverse provokes a significant downstream shift of the transition location. Without the traverse, the transition occurs approximately 11% further downstream at $x/c = 0.58$ for the same angle of attack. This significant difference encountered in flight could not be quantified appropriately in the initial wind-tunnel experiments due to the acoustically disturbed conditions which prevented successful microphone measurements. At the same time, the visibility of the natural instability frequencies is enhanced by removal of the traverse. The reasons for this behavior are found in the disturbance spectra of the microphone data visualized in Figures 6.18 and 6.19, showing distinct peaks at 300 Hz and 600 Hz if the traverse is installed. These frequencies may originate from structural vibrations due to the additional traverse installation or from acoustic excitation. Systematic variation of the flight speed leads to varying disturbance frequencies, such that acoustic excitation due to flow separation on the traverse appears to be the most likely explanation. An estimate of the Strouhal number, based on the average thickness of the traverse components $l_{\mathrm{ref}} = 12\,\mathrm{mm}$, the flight speed $U_{\mathrm{TAS}} = 38\,\mathrm{m/s}$

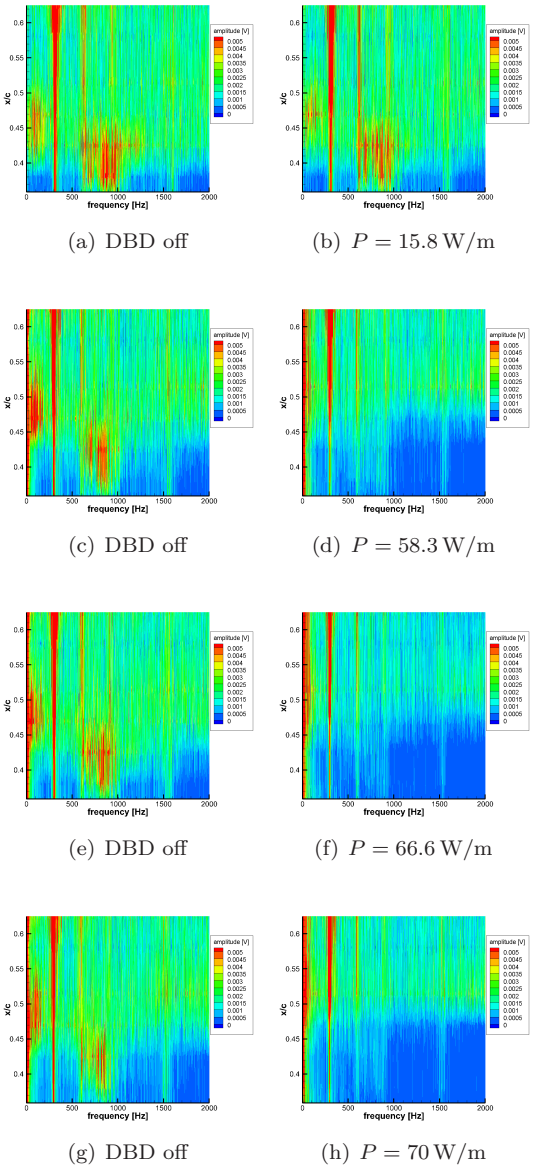

(a) DBD off (b) $P = 15.8\,\mathrm{W/m}$

(c) DBD off (d) $P = 58.3\,\mathrm{W/m}$

(e) DBD off (f) $P = 66.6\,\mathrm{W/m}$

(g) DBD off (h) $P = 70\,\mathrm{W/m}$

Figure 6.19: Spectrogram of microphone signals, actuator power variation.

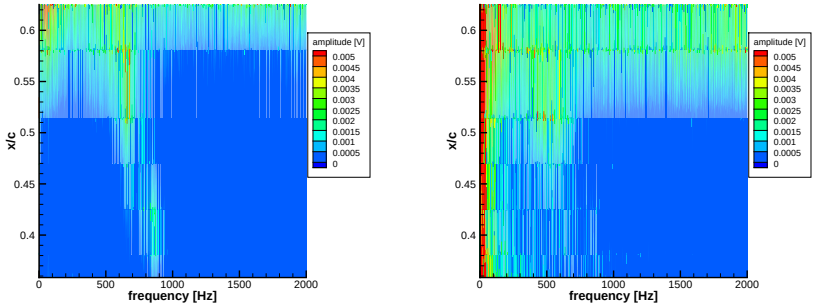

(a) DBD off

(b) DBD on

Figure 6.20: Spectrogram of microphone signals without traverse, DBD on/off at $T = 16\,\mathrm{mN/m}$ ($P = 66.6\,\mathrm{W/m}$) for $\alpha = 0.7°$, $U_{\mathrm{TAS}} = 38\,\mathrm{m/s}$.

and the frequency $f = 600\,\mathrm{Hz}$, yields

$$St = f\,\frac{l_{\mathrm{ref}}}{U_{\mathrm{TAS}}} = 0.189 \tag{6.4}$$

which is in close agreement to the expected value $St = 0.2$ for bluff body vortex shedding. A better aerodynamic fairing of the traverse structure to reduce the acoustic influences remains to be designed in the future.

The pressure distributions in Figure 6.21 underline the experienced differences due to the traverse installation. Since the outboard traverse support is fixed at $x/c = 0.71$ in immediate spanwise proximity of the pressure taps, the pressure measurements are corrupted along the aft quarter of the glove pressure side. Upstream of the support position, increased pressures are observed due to a ram effect whereas flow acceleration leads to decreased pressures downstream.

Without the traverse installation, the microphone data shows a much smoother frequency distribution and no singular peaks are found, facilitating the comparison with numerical stability analysis. Boundary-layer computations and stability analysis of the wing glove have been discussed in Chapter 5.5. The corresponding stability diagram for $\alpha = 0.7°$ and $U_{\mathrm{TAS}} = 38\,\mathrm{m/s}$ is illustrated in Figure 5.9. The results can be compared to the microphone data in Figure 6.20 (a) revealing good agreement of the instability frequencies. The tongue-shaped instability range shows a decrease

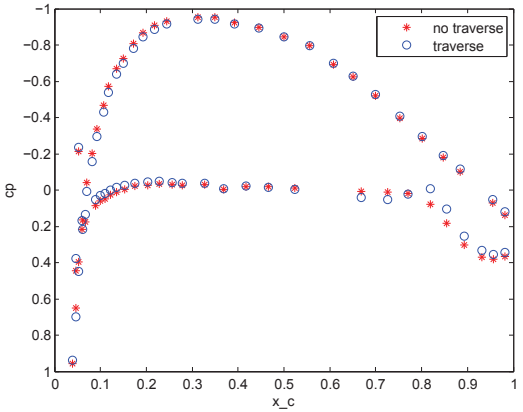

Figure 6.21: Effect of the traverse system on the pressure distribution, $\alpha = 0.7°$, $U_{\mathrm{TAS}} = 38\,\mathrm{m/s}$.

of the unstable frequencies for increasing streamwise positions, both in the experiments and the numerical stability analysis.

As indicated in Figure 6.20 (b), DBD operation does not delay the transition for $\alpha = 0.7°$ but rather accelerates it if the traverse is not installed. Although the actuator mainly imparts momentum in streamwise direction, it may also induce disturbances if operated in the stable boundary-layer region. The receptivity mechanism by which the presence and operation of the DBD is transformed into disturbances which trigger the transition cannot be understood from these experiments and would require further systematic investigation. Nevertheless, it can be seen that the instabilities around 800 Hz in the region between $x/c = 0.35 - 0.45$ are effectively attenuated by the DBD operation. Disturbance frequencies below 100 Hz are strongly excited, but ground measurements in the absence of fluid flow show similar frequency peaks at low frequencies if the DBD actuator is operated. It is therefore likely that the observed frequencies derive from electromagnetical coupling to the measurement equipment.

In order to successfully delay transition, the actuator position in relation to the transition location must be chosen appropriately. Since the actuator location cannot be easily adjusted in the experimental setup, the transition location may be shifted to obtain better results. By lowering the angle of attack to $\alpha = 0°$ for flights without the traverse, the flow speed and the adverse pressure gradients are increased by 2 m/s and $\mathrm{d}c_p/\mathrm{d}(x/c) = 0.2$

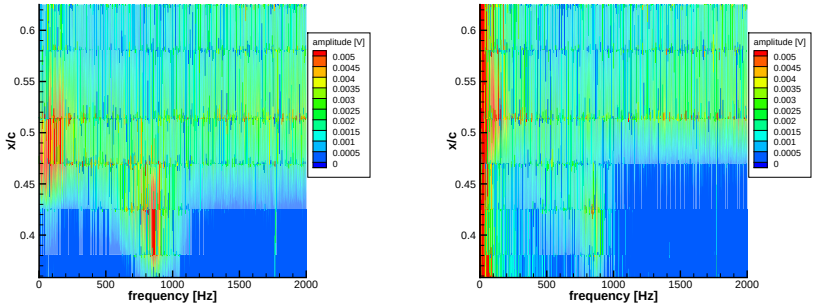

(a) DBD off

(b) DBD on

Figure 6.22: Spectrogram of microphone signals without traverse, DBD on/off at $T = 16.2\,\mathrm{mN/m}$ ($P = 66.6\,\mathrm{W/m}$) for $\alpha = 0°$, $U_{\mathrm{TAS}} = 40.3\,\mathrm{m/s}$

and transition moves upstream. Figure 6.22 (a) illustrates the broadband disturbance increase at $x/c = 0.46$. This transition location is comparable to the case with traverse at $\alpha = 0.7°$, presented in Figure 6.18 (a). Again, the removal of singular disturbances at $f = 300$ and $600\,\mathrm{Hz}$ is achieved as compared to the case with traverse. Activating the single DBD actuator at $T = 16.2\,\mathrm{mN/m}$ ($P = 66.6\,\mathrm{W/m}$) as illustrated in Figure 6.22 (b), the obtained transition delay to $x/c = 0.49$ is in the same order of magnitude as for the case with traverse. This is surprising since the conditions are much more destabilizing due to higher speed and a stronger adverse pressure gradient. These adverse effects may be compensated by the lack of deterministic instabilities introduced by the traverse installation. After all, an exact quantification based on the microphone data is difficult due to coarse spacing of functional sensors. Failing better flush-mountable sensors for transition detection, the traverse is re-installed to quantify the obtainable transition delay, condoning the disturbances introduced by the installation itself.

6.3.2 Hot-Wire Measurements

As in Chapters 4.1 and 6.1.2, the transition process is identified by hot-wire measurements. Figure 6.23 illustrates normalized velocity profiles acquired at four streamwise positions within the transition zone on the wing glove

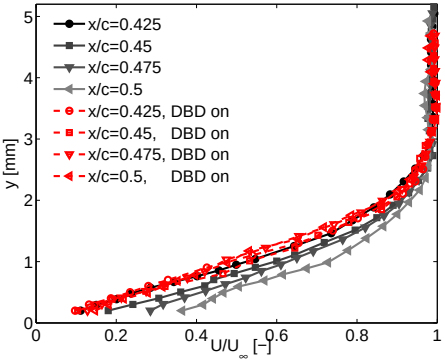

Figure 6.23: Velocity profiles on pressure side for $\alpha = 0.56°$, $U_{\mathrm{TAS}} = 38.6\,\mathrm{m/s}$, DBD on/off at $T = 16\,\mathrm{mN/m}$ ($P = 66.6\,\mathrm{W/m}$). Wall offset not corrected.

at $\alpha = 0.56°$,$U_{\mathrm{TAS}} = 38.6\,\mathrm{m/s}$. The profiles have not been corrected for the wall-normal offset; hence the impression may arise that the no-slip condition is not satisfied. Solid lines indicate measurements without, dashed lines with DBD operation at $T = 16.2\,\mathrm{mN/m}$ ($P = 66.6\,\mathrm{W/m}$). With increasing streamwise distance, the velocities measured directly at the wall increase continuously without flow control. This indicates the increasing momentum exchange within the wall-near region associated with temporal occurrence of turbulent spots. The last velocity profile at $x/c = 0.5$ exhibits the turbulent characteristic of a fuller velocity distribution in the proximity of the wall. For the flow-control case, the velocity profiles do not show significant variation along the streamwise dimension. The boundary-layer thickness increases insignificantly over the illustrated 10% chord and no evidence of initiated transition is found if the DBD actuator is operated.

Despite this indication of postponed transition in the case of DBD forcing, the uncertainty of the data acquisition needs to be addressed. The variation of the normalized freestream velocity at the boundary-layer edge by 4% indicates that the flight state cannot be maintained throughout the complete measurement. Data acquisition at 45 wall-normal positions for each velocity profile plus traversing of the probe sum up to six minutes duration for one complete set of data. Two seconds of measurement time at each probe location are necessary to reduce the effect of vibrations induced by the traverse movements. A necessary limitation to four profiles

impedes a detailed analysis of the shape factor evolution. During the measurement, the plane descends 3′000 ft and the Reynolds number increases by 5.9% due to increasing air density and viscosity, even if the flight velocity is maintained. To ensure the comparability of results, the same flight maneuvers are performed once without and, after climbing to the initial altitude, again with DBD actuation. Marginal attitude variations can either be induced by the pilot, plane eigenmodes or wind gusts and are likely to occur during long measurements. For adequate characterization of the transition location, a quicker measurement scheme is necessary.

If only the velocity fluctuation at the wall is considered, a finer resolution in streamwise direction can be combined with lower acquisition times through dramatic reduction of measurement positions. As shown before, the velocity standard deviation is indicative of the transition process and enables quantification of the transition delay. Figure 6.24 displays the evolution of the hot wire standard deviation at the wall ($y = 0\,\mathrm{mm}$) along the streamwise coordinate for two different angles of attack $\alpha = 0.6°$ (a) and $\alpha = 0.4°$ (b). The hot wire is traversed to 25 wall-positions with 5 mm spacing, enhancing the spatial resolution by a factor of 6 in comparison to the microphone measurements. Each position is held for 10 seconds during which the DBD actuator is operated for 5 seconds. Due to the alternating operation and deactivation of the DBD actuator, the power consumption is not closed-loop controlled but a constant control signal $\zeta = 2.7\,\mathrm{V}$ is provided to the *MiniPuls 2.1*. The average power consumption during the measurements is quantified with $P = 54.2 \pm 0.4\,\mathrm{W/m}$, such that an approximate thrust of $T = 13.4\,\mathrm{mN/m}$ is exerted on the flow. This procedure ensures similar ambient conditions and comparability of the datasets.

A trend of the hot wire fluctuations can be identified for flights without and with DBD actuation. A least-square-fitted trend line is approximated by a 4th-order polynomial for each case. Measurements with activated flow control at $\alpha = 0.6°$, $U_{\mathrm{TAS}} = 38.6\,\mathrm{m/s}$, shown in Figure 6.24(a), hardly reveal the signal peak at the downstream end of the domain. Here, only the parallel displacement of the trend line slopes Δ_{par} can be compared, rendering the transition delay 2.5%. A more precise quantification is possible for the decreased $\alpha = 0.4°$, $U_{\mathrm{TAS}} = 39\,\mathrm{m/s}$ in Figure 6.24(b). For both the controlled and uncontrolled cases, the intermittency peak is observed within the measurement area. The displacement of the peak Δ_{peak} and of the slopes both indicate a transition delay of 2%. The trend of diminishing transition delay for lower α is consistent with the decreasing boundary-layer stability due to flow speed and pressure gradient augmentation.

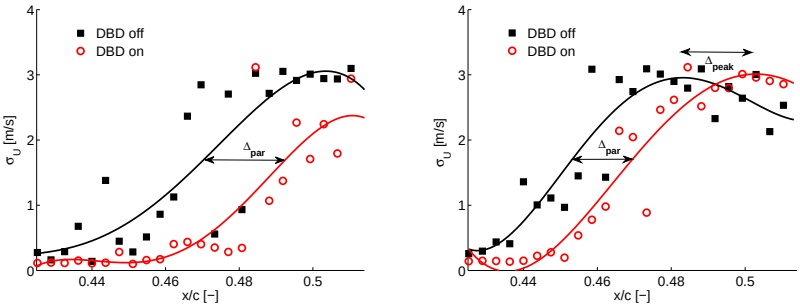

(a) $\alpha = 0.6°$,$U_{TAS} = 38.6\,\mathrm{m/s}$ (b) $\alpha = 0.4°$,$U_{TAS} = 39\,\mathrm{m/s}$

Figure 6.24: Standard deviation of the hot-wire signals at the wall ($y = 0\,\mathrm{mm}$) under varying flight states, DBD on/off at $T = 13.4\,\mathrm{mN/m}$ ($P = 54.2\,\mathrm{W/m}$).

Since the frequency spectra of the microphone signals provide valuable information about the boundary-layer state during the flight measurements, a spectral analysis of the hot-wire is conducted. For each of the 25 measurement positions along the streamwise direction, a one-second segment of the hot wire signal is processed with FFT. An example is shown in Figure 6.25 (a) for the hot-wire position $x/c = 0.47$, illustrating the ability of the actuator to reduce fluctuations inside the boundary-layer flow. The power spectral density without flow control (solid line) exhibits broadband characteristics and is one order of magnitude higher compared to the case with DBD actuation (dashed line). The assumption of transitional flow without and laminar flow with DBD actuation at this streamwise position is in agreement with the observations from Figure 6.24 (a).

Processing of the spectral content of all 25 hot-wire signals along the streamwise direction in the same manner as for the microphones reveals the contour plots in Figure 6.25 (b) and (c). Strong interferences at discrete frequencies due to the traverse system, as detected in the microphone spectra, are not visible in the hot-wire signals. This again supports the hypothesis that the disturbances are caused by acoustic noise instead of mechanical vibrations since the hot wire is less sensitive to acoustic forcing. The contour plots basically show the same characteristics as the standard deviation plot in Figure 6.24 (a). The broadband increase is postponed from $x/c = 0.465$ to $x/c = 0.49$ due to DBD forcing, indicating a transition

delay of about 2.5% chord length. In close agreement with all experimental results, this even exceeds the predictions of 1.8% based on a numerical solution of the flow case presented in Chapter 5.5.

Another way to quantify the transition is to maintain the probe position constant and vary the flow speed. During the flight experiments, this is achieved by a constant acceleration or deceleration as described earlier in this section. The results obtained can be reviewed in Figure 6.17 (a) since no difference between flights without and with DBD operation, even at different thrust settings $T \geq 16.2\,\mathrm{mN/m}$, are gauged. One plausible explanation is the strong influence of changing angles of attack on the pressure distribution. The strengthening of the adverse pressure gradient during acceleration leads to a fast upstream propagation of the transition location. Since the DBD actuator is only effective if the distance to the transition line is not excessively high, the possible beneficial effects may be suppressed by the continuous advancement of the transition line.

6.3.3 Forced Transition and Stability Analysis

Microphone data and stability computations clearly reveal an amplified frequency range between $600 - 800\,\mathrm{Hz}$ ahead of the transition line for the cases without the traverse. To preclude that these frequencies originate from structural vibrations and demonstrate that they initiate the natural transition, controlled disturbance experiments are conducted. Defined disturbance conditions are useful to identify which frequencies most effectively initiate the transition process. By comparing the experimental results (dashed line) in Figure 6.26 with a computational prediction of the spatial growth rates (contour) of a clean wing, unstable frequencies are identified.

Multiple constant acceleration glides are performed while defined frequencies are excited by the disturbance source at $x/c = 0.18$. The signal deviation of a hot wire positioned on the surface at $x/c = 0.46$ is monitored to detect the angle of attack at which transition occurs. The disturbance amplitude is chosen carefully to influence the transition process only and not to bypass the process of Tollmien-Schlichting wave amplification, immediately triggering turbulent conditions. Separate acceleration flights are performed for excited frequencies between $f_{\mathrm{exc}} = 400 - 1100\,\mathrm{Hz}$ and the angle of attack at which the peak of the standard deviation occurs is identified.

The corresponding angle of attack at each excitation frequency is illustrated with a dashed line in Figure 6.26. The frequency of $f_{\mathrm{exc}} = 800\,\mathrm{Hz}$

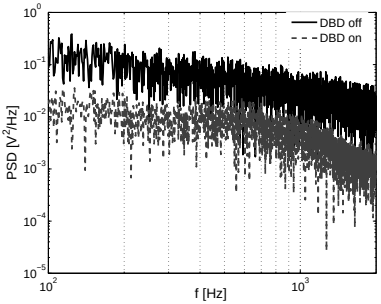

(a) Spectrum for hot-wire signal at $x/c = 0.47$, DBD off (solid) and on (dashed)

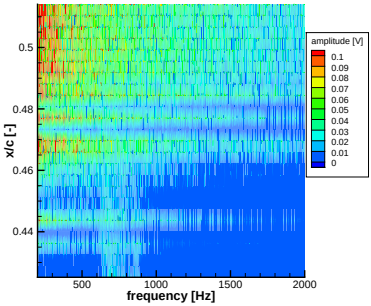

(b) Spectrogram of hot-wire signals, DBD off

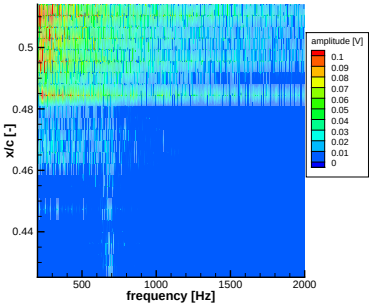

(c) Spectrogram of hot-wire signals, DBD on

Figure 6.25: Spectrum of hot-wire signals at the wall ($y = 0\,\text{mm}$) between 100 and 2'000 Hz, $\alpha = 0.6°$, $U_{\text{TAS}} = 38.6\,\text{m/s}$, DBD on/off at $T = 13.4\,\text{mN/m}$ ($P = 54.2\,\text{W/m}$).

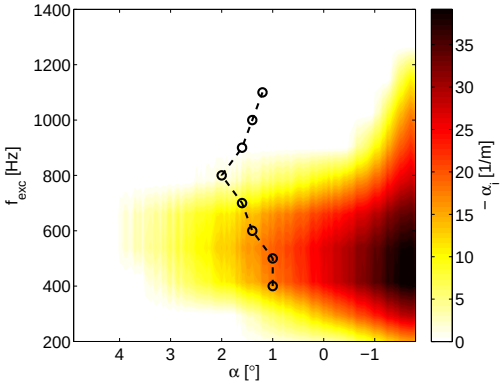

Figure 6.26: Spatial growth rates (contour levels) versus transition location (dashed line) for forced disturbance conditions.

enforces the signal peak to occur under the most stable conditions at $\alpha = 2°$ whereas other frequencies require more unstable angles of attack to ensure transition at this streamwise position. This indicates that the boundary layer is most receptive to this frequency at the given location, which is in agreement with the microphone measurements presented before. The underlying contour levels, indicating the streamwise spatial growth rates α_i, are obtained from a stability analysis of a computational study. For this purpose, the boundary-layer profiles at $x/c = 0.46$ on the wing glove pressure side are computed with the boundary-layer code for varying angles of attack and the growth rates are obtained from linear stability analysis. The tongue-shaped countour levels indicate the range of the unstable frequencies with maximum instability at $f = 600\,\mathrm{Hz}$. Of interest is the symmetric distribution around the most unstable frequency, found both in the experimental and the numerical data. The numerical growth rates indicate the disturbance amplification relevant far ahead of the actual transition location. It needs to be taken into account that the experimental data represents the points of maximum intermittency, indicating advanced stages of transition. The deviation of the frequencies may be explained by the shift of relevant instabilities during the downstream evolution which has also been observed in the experimental data, e.g. Figure 6.20. The influence of the hot-wire traverse also needs to be taken into account which cannot be represented in the numerical study.

6.4 Efficiency Estimate

The effectiveness η^* of DBD flow control is usually expressed by the ratio of a desired fluid mechanic effect, e.g. the produced thrust [58], to the consumed energy. In this form, it is a dimensional quantity and cannot be compared for different kinds of flow-control applications. More conveniently, the efficiency of active flow control can be defined by relating the net power savings to the invested energy per time. Moreau et al. [73] estimate the power savings of boundary-layer flow control by integration of the momentum flux across a control volume. The change of the momentum distribution due to DBD operation is experimentally measured with a pitot-tube and transformed into fluidic power by applying the conservation equation of kinetic energy.

In steady flight, the necessary propulsion power counterweights the aircraft resistance, which is to a large portion constituted by the wing drag. If the wing profile drag D can be reduced, the fluidic power consumption

$$P_p = D\,U_\infty \tag{6.5}$$

is diminished. The drag coefficient c_D is necessary to calculate the profile drag

$$D = c_D\,\frac{\rho}{2}\,l_{\mathrm{ref}}\,U_\infty^2 \tag{6.6}$$

where the reference length $l_{\mathrm{ref}} = 2.73\,\mathrm{m}$ is the circumferential arc length of the wing glove. The drag coefficient c_D is composed of a pressure drag component, $c_{D,p}$, and a friction drag component, $c_{D,f}$. The friction drag coefficient accounts for the viscous interaction of the flow with the surface within the boundary-layer. To calculate the friction drag coefficient $c_{D,f}$ of an airfoil, the local skin friction coefficient c_f is integrated along the arc length s

$$c_{D,f} = \int c_f\,\mathrm{d}s. \tag{6.7}$$

Computational fluid dynamics enables flow simulations deducing all flow quantities of interest. Simple panel methods are sufficient to deliver the lift and drag of airfoils at specified flow conditions. Here, *Xfoil* is employed to simulate the flight conditions on the wing glove at $U_{\mathrm{TAS}} = 38\,\mathrm{m/s}$ and $\alpha = 0.7°$. The drag coefficients are derived from two simulations with fixed transition on the pressure side, conservatively representing either the natural transition conditions ($x_{\mathrm{trans}}/c = 0.47$) or the transition location under DBD influence ($x_{\mathrm{trans}}/c = 0.5$), see Figure 6.18. For the density,

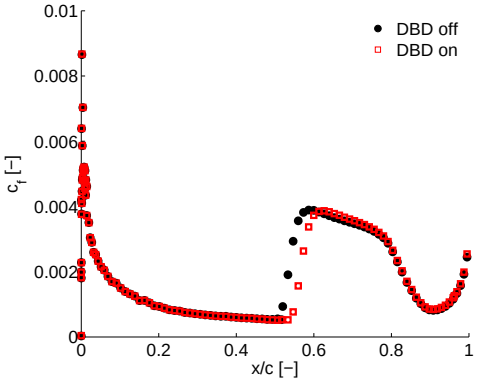

Figure 6.27: Friction coefficient along the glove pressure side derived from *Xfoil* for forced transition locations $x_{\text{trans}}/c = 0.47$ (DBD off, circles) and $x_{\text{trans}}/c = 0.5$ (DBD on, squares).

standard conditions ($\rho = 1.225\,\text{kg/m}^3$) are assumed. Figure 6.27 illustrates the local skin friction coefficient c_f along the pressure side of the glove with and without flow control. Illustrative, the difference between the area under the particular curves clarifies the integral effect of 3% transition delay. The drag coefficient c_D for the two cases is summarized in Table 6.2. In both simulated *Xfoil* cases, the pressure drag component is equal such that the drag coefficient reduction is caused only by the friction component, $\Delta c_D = \Delta c_{D,f} = 0.00008$. If these values are processed with equations (6.5) and (6.6), a reduction of the necessary propulsion power by $\Delta P_p = 3.6\,\text{W/m}$

Solver	x_{trans}/c	c_D
Xfoil	0.47	0.00539
Xfoil	0.5	0.00531
FLUENT	0.52	0.0048
EDGE	0.55	0.00854
EDGE	0.58	0.00841

Table 6.2: Comparison of drag coefficients from different numerical solvers. Transition is either triggered or computed at the indicated positions on the wing glove pressure side.

is computed. The flow-control efficiency can hence be defined by the ratio of the saved propulsion power ΔP_p to the actuator power consumption P.

$$\eta = \frac{\Delta P_p}{P} \tag{6.8}$$

The power consumed in the flight experiments is closed-loop controlled at $P = 66.6\,\mathrm{W/m}$, yielding an efficiency of $\eta = 5.4\%$. In the current setting, no net gain is achieved since the power consumption significantly exceeds the power savings which is a typical result encountered in active flow-control experiments. The calculations do not include the electrical efficiency η_e defined by Kriegseis [58] as the ratio of power supplied to the high voltage generator P_{input} and the power P consumed for the force generation. This efficiency is maximized around 60% if the DBD actuator is operated at the resonance frequency. Additionally, the simplified evaluation based on *Xfoil* computations does not account for a local skin-friction increase at the actuator location due to the flow acceleration reported by Quadros [83]. For these reasons, the resulting power savings may be slightly overrated.

Nevertheless, positive effects are also disregarded. The propulsion thrust created by the actuator in flow direction could be utilized by a moving object but cannot be considered in this simplification. The drag coefficient from *Xfoil* is compared to other CFD solvers and yields an intermediate value between *FLUENT* and *EDGE* computations, included in Table 6.2. The more sophisticated *EDGE* computations by A. Hanifi on unstructured grids predict higher drag savings based on a variation of the transition location, such that the total efficiency may be even higher than evaluated by *Xfoil*. Flight experiments by Weismüller [114] using the same wing glove geometry show that *Xfoil* underestimates the absolute drag in comparison to measurements with a wake rake, as illustrated in Figure 6.28. For the relevant lift coefficient of $c_L = 0.6$ for flights at $\alpha = 0°$, the total drag is undervalued by a factor of approximately 0.75.

6.5 Conclusions

Initial wind-tunnel measurements on the pressure side of a NLF wing glove indicate the possibility to delay natural transition occurring at moderate angles of attack $\alpha = 0.7°$ and flight speeds $U_{\mathrm{TAS}} = 38\,\mathrm{m/s}$. The obtained delay of 3% chord is quantified by hot-wire measurements of the boundary-layer shape factor as well as characteristic velocity fluctuations at the wall.

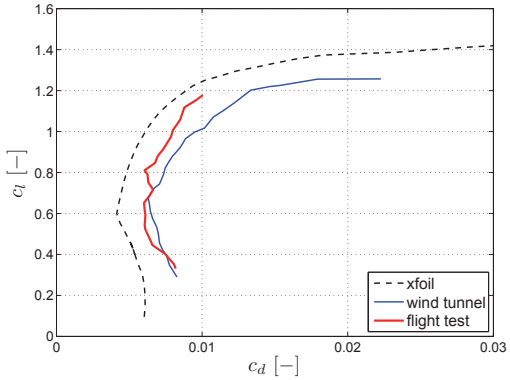

Figure 6.28: Lift-drag polar of the wing glove airfoil from wind tunnel and flight measurements by Weismüller [114] compared to *Xfoil* computations.

Microphone data does not provide valuable insights due to highly disturbed acoustic conditions in the wind-tunnel test section.

A qualitative evaluation of ambient condition changes on the performance of DBD actuators is performed at the beginning of the flight measurement campaign. A significant influence of air humidity and pressure is recognized, although a thorough quantification of the sensitivity towards each factor is impossible due to mutual coupling of the various effects. Nevertheless, a closed-loop controller successfully counterbalances these influences. The stabilized control authority thereby enables the first genuine flight application of DBD actuators under non-laboratory conditions.

First flow-control flights show the influence of dynamic aircraft eigenmodes and slip angle variations on the transition location, requiring steady and undisturbed flight conditions during the glides. To reduce the influence of variable flow conditions, the measurement time needs to be as short as possible, limiting the possible measurement approaches with the hot-wire traverse. The traverse itself has a significant impact on the transition process, promoting the intermittency peak to occur 11% upstream of the undisturbed location.

Nevertheless, the DBD actuator successfully delays the transition by 3% chord both with traverse installed as well as under the more unstable conditions of lower α without the traverse. The magnitude of the obtainable transition delay in the wind-tunnel experiments and in flight coincide pleas-

ingly well, even though the absolute transition locations for the same flow conditions do not agree perfectly. This is explained by the high-disturbance acoustics inside the wind tunnel which also inhibit the detection of natural instability frequencies.

These frequencies between 600 and 800 Hz are observed from microphone measurements in flight, showing good agreement with linear stability computations. A decrease of the primary instability frequency with increasing chordwise position is observed both in the experiments as well as in the numerical investigations. These disturbance frequencies are effectively attenuated by the DBD operation, leading to the macroscopic transition delay. The relevance of this frequency range for the transition process is scrutinized by controlled disturbance experiments. Artificial excitation of instabilities confirms the major sensitivity of the transition process to frequencies around 800 Hz.

A rough estimate for the efficiency of the flow control is attempted based on *Xfoil* computations. The measurable transition delay decreases the drag and the necessary propulsion power by 1.9%. Related to the energy consumption of the DBD operation, a net efficiency of $\eta = 5.4\%$ is achieved at $U_\infty = 38\,\mathrm{m/s}$ flight speed. Considering the novelty of the presented experiments and their preliminary nature, the calculated efficiency is close to a revelation.

The importance of these first flight experiments for the maturity of DBD flow control cannot be underrated. A thorough discussion of all observations, the lessons learnt and comprehensive conclusions are presented in the following.

7 Discussion

The present work significantly improves the knowledge on transition delay capabilities of dielectric barrier discharge plasma actuators. A combination of experimental and numerical investigations is used to clarify the effect of electro-hydrodynamic flow control on the stability properties of laminar boundary-layer flow. The question how and under which conditions DBD forcing leads to a measurable transition delay is addressed by wind-tunnel and flight measurements. The possibility to delay naturally occurring, Tollmien-Schlichting wave dominated transition under elevated flow velocities and Reynolds numbers is successfully explored. Validation of a newly developed numerical solver with the experimental data yields respectable results, qualifying the numerical procedure for the design of flow-control experiments. Finally, the application of DBD actuators on a motorized glider results in the first successful flow-control application of DBD actuators under elevated Reynolds numbers as well as atmospheric flight conditions, lifting the maturity of DBD flow control far beyond the status of academic laboratory research.

Several key questions concerning DBD flow-control experiments had been stated in Chapter 1.3 and have been addressed in the current study. In the following sections, these questions are recapitulated and comprehensively discussed considering the insights gained in the single chapters. Starting with a summary of the observations, the main discoveries and key messages as well as shortcomings are discussed, paving the way for a prospective outlook from a remote perspective.

7.1 DBD Effect on Stability

The experimental and numerical data obtained throughout the project enhance the understanding of the stabilizing impact of DBD actuation on laminar boundary-layer flow. Application of a linear stability solver to numerical and experimental boundary-layer data under the influence of DBD actuation yields increased critical Reynolds numbers and decreased amplification rates for a broad frequency range of modal disturbances. The broadband disturbance attenuation explains the suitability of continuous

DBD operation for the control of naturally occurring transition. The findings agree well with published observations of pulsed DBD actuation in large eddy simulations [24] due to the modification of the average velocity profiles. In contrast to the stability analysis of generic combinations of boundary-layer profiles with wall-jets investigated by Riherd and Roy [86], the present work employs an adequate numerical procedure for the approximation of the Navier-Stokes equations. The solutions from the boundary-layer solver with implemented body-force model enable an analysis of the stability properties. The overall reproducibility of modal disturbance evolutions by the stability method proves the relevance of the stabilizing actuator effect for the transition process. Speculations on instability deformations by flow confinement and wall-normal velocity components can be discarded since the modal instability attenuation is sufficient to explain the macroscopic transition delay.

For the first time DBD flow-control data has been analyzed within the PSE framework, accounting for slightly non-parallel flow features. The comparison of linear stability theory and the PSE computations on validatory DNS data from Vieira et al. [111] reveals a better match of PSE in the vicinity of the actuator. This underlines the importance of incorporating non-parallel effects induced by the localized flow manipulation into stability considerations. Surprisingly, the downstream evolution of modal disturbances is better quantified by the linear stability theory. Although the exact reasons for this behavior remain unknown from the attainable data, the availability of both procedures enables comparative investigations on additional computational setups. The initiated cooperation with KTH and their world-renown excellence in stability research will be helpful to further enhance the predictability of the Tollmien-Schlichting wave amplitude evolution under the influence of DBD actuation. Possibly a coupling of the different procedures or more sophisticated stability considerations will lead to satisfactory results, enabling convenient and reliable transition prediction for DBD flow-control applications.

Stability analysis of experimental boundary-layer profiles with high wall-normal resolution from optical measurements show an increase of the critical Reynolds number due to actuator operation. The increasing critical Reynolds numbers for increasing actuator thrust agree with observations from transition measurements, although a direct quantitative comparison is hindered unless the high resolution is extended to the streamwise dimension. Phase-locked particle image velocimetry reveals the quantitative evolution of artificially generated, single frequency Tollmien-Schlichting waves

approximately 4.5 wavelengths along the streamwise direction. Instead of tripled velocity fluctuation magnitudes observed without flow control, DBD actuation reduces the growth over the investigated domain to a factor of 2. More enlightening is the change of the propagation speed of the disturbances due to the flow-control application. The gradual acceleration along the surface can only be explained by altered stability properties and not by localized acceleration of the flow and the contained disturbance.

The shape factor as an integral boundary-layer quantity may not be directly used as a measure of flow stability in the proximity of flow-control devices. Albrecht et al. [2] shows that a monotonic dependence between the shape factor and the critical Reynolds number as described by Wazzan et al. [112] cannot be derived for electromagnetically forced flow. Nevertheless, the present results evince a shape factor decrease by DBD operation coupled to enhanced flow stability in laminar boundary layers. Both the experimental as well as the numerical data indicate decreasing shape factors which correlate with the obtained transition delay and decreased growth rates.

7.2 Optimization and Flow Control Design

In addition to the stability implications of DBD forcing, several parametrical studies increase the knowledge about relevant parameters related to the design of DBD flow-control applications. For a variation of the actuator thrust and position, an impact quantification based on transition measurements and boundary-layer computations is provided. The numerical procedure combines a finite-difference solution of the laminar boundary-layer equations with a DBD force field model and linear stability analysis, enabling transition prediction based on empirical laws. The validation of this numerical method with generic wind-tunnel experiments yields good agreement. The consistent data renders the introduced numerical method a valuable tool kit for flow-control design and transition prediction under the influence of DBD actuation.

Transition measurements on a flat plate and systematic variation of the actuator position suggest a strong impact of adequate device allocation. Dependent on the position within the flow, a DBD actuator exhibits a certain effectiveness for boundary-layer stabilization and resulting transition delay. The spatial extent of the DBD force field in relation to the boundary-layer thickness is of importance for enhanced control authority.

Experiments indicate that actuator positions far downstream are beneficial, but no optimum location can be determined. The maximum downstream positioning is limited by the natural transition location since DBD transition control is ineffective in already turbulent flow. Preliminary sensitivity calculations based on an adjoint formulation of the governing equations indicate that the local stability properties of the boundary layer require additional consideration. Numerical studies with the finite-differences boundary-layer solver and the linear stability code reproduce the general trend of the position sensitivity but lack a correct quantitative estimate for the effect on transition. A thorough revision of numerical possibilities to account for this influence is recommended. Further sensitivity calculations in cooperation with A. Hanifi from KTH Stockholm will lead to a better understanding of optimized actuator positioning and will help to validate the newly developed numerical codes.

In terms of thrust optimization for transition delay on a flat plate, the present results do not yield an optimum at elevated magnitudes as reported by Grundmann [43]. Unlike in the cited experiments, excessive distortion of the boundary-layer profile leading to a positive profile curvature and destabilizing effects is not found in the present work due to operation in higher freestream velocity surroundings. With increasing flow speed, higher energy expenditure is required to maintain the effectiveness of the flow manipulation. In the present work, the dielectric material limits the electric potential difference such that the optimal forcing conditions cannot be experimentally investigated.

7.3 In-Flight Application

Based on the numerical design tools developed in the course of this project, an experiment for the application of DBD transition control in flight has been developed. Initial wind-tunnel measurements and following flight tests on the G109b motorized glider demonstrate the possibility to delay naturally occurring transition by means of steadily operated DBD actuators under varying ambient conditions.

The atmospheric conditions and their influence on the DBD power consumption have been thoroughly analyzed, identifying the pressure and the humidity to provoke the largest detrimental effects. Flight measurements monitoring these quantities and the power consumed by DBD operation have paved the way for a successful implementation of a closed-loop performance controller. Based on the assumption of constant correlation be-

tween actuator power consumption and integral thrust, the stabilization of the power under varying ambient conditions enables constant flow-control authority during measurement flights.

Although the presented effort is not the very first airborne DBD application, compare [98], it is the first and only one to show a desirable flow-control effect under realistic flight conditions. The respectable transition delay of 3% chord length during the first non-optimized flights coincides with initial wind-tunnel measurements and exceeds the numerically predicted effect. The flight experiments indicate a saturation of the control effectiveness despite increasing thrust magnitude, such that an efficiency consideration between the energy expense and savings is necessary. A conservative calculation of the net drag reduction by approximately 1.9% results in a computed power efficiency of $\eta = 5.4\%$. Comparing this value to the flow control efficiency of DBD actuators (defined as the ratio between kinetic energy transferred into the fluid and the energy expenditure) which reaches maxima of 0.1% [58] in quiescent air, the found power savings indicate the high leverage effect of DBD application for transition control purposes.

8 Outlook

This thesis answers highly relevant questions related to the physical mechanisms of DBD transition delay, control effectiveness optimization and the applicability under non-laboratory conditions for higher Reynolds number flows. From a remote perspective, the state-of-the-art of DBD transition control was significantly improved over the course of the project. Motivated by low Reynolds number flat plate experiments with artificial disturbance excitation and little knowledge about the reasons for successful transition delay, the project results have contributed significantly in the maturity process of DBD transition control. Extensive parametrical studies have increased the knowledge on the stabilizing impact, leading to the development of numerical optimization tools for flow control. The successful proof-of-concept of in-flight transition delay defies natural transition mechanisms, high Reynolds numbers and varying atmospheric conditions. Future investigations may aim at optimizing the transition control effectiveness or at increased efficiency for a net benefit. Both procedures are viable and complementarily connectable. Although many new insights into the topic of DBD transition control have been obtained, the results give rise to a whole set of new questions and interesting outlooks for future investigations. It is the sincere hope of the author that further improvements of the experimental and numerical arrangements may lead to increased DBD flow-control effectiveness and eventually a positive net efficiency.

Fine-resolved boundary-layer profiles in both the wall-normal and streamwise direction should be obtained by laser-optical wind-tunnel measurements in the proximity of different DBD configurations. Such data can be analyzed with the available stability tools to provide a thorough experimental quantification of the stabilizing impact. As an additional benefit, it enables the force field distribution and the integral thrust to be computed. Varying the flow speed and the flow humidity, detrimental effects of changing ambient conditions on the thrust can directly be quantified. Simultaneous power measurements or closed-loop control of this quantity is expected to confirm the equivalence of power consumption and force magnitude, which is a basic assumption of the presented work.

Shortcomings of the flight instrumentation, leading to imprecise tran-

sition detection, have been identified within this thesis. These problems can be overcome by replacing microphones with flush-mounted hot-film sensors connected to a newly acquired multi-channel constant-temperature anemometer. To facilitate the comparison to the numerical data, wisely distributed hot-film sensor arrays may provide experimental instability growth rates, additionally mitigating the problems associated with the traverse installation. Aerodynamic improvements of the prototype hot-wire traverse will reduce the impact on the pressure field and transition along the wing glove, yielding advanced flight measurement data in the future. Additional improvements of the aircraft are under way, an inertial navigation unit as well as acceleration measurements on the fuselage and the wings will enhance the maintainability and detection of steady flight states. Neatly complementing the research on the influence of atmospheric turbulence on the transition process on the wing glove, a compensation of premature transition tripping due to high ambient turbulence is deemed possible by means of DBD flow control.

Sophisticated computations of the full wing glove airfoil with DBD implementation and adequate representation of turbulence is desired to correctly simulate the stabilizing effect and obtain a realistic estimate for the transition process. Such an extensive study provides a quantification of the undesired friction increase close to the actuator which has been neglected in the efficiency estimate. Additionally, it delivers a complete overview of the flow-control effect on the flow circulation, including lift and moment coefficients of the the airfoil. A more exact estimation of the airfoil drag, agreeing with experimentally measured values, would additionally increase the credibility of efficiency calculations. Direct numerical simulations reveal all relevant data and additional features of the transition mechanism, including non-linear instability effects. Such a study has been started in cooperation with D. Henningson at KTH Stockholm and is expected to enhance the overall effectiveness of various flow-control approaches on the laminar wing glove.

Although a net energy gain is not yet observed in flight application, the two-digit percentage range of the efficiency during a proof-of-concept renders future enhancements credible, e.g. by ceramic dielectric materials. These do not only increase the actuator durability but also enhance the electrical efficiency of the power cycle if the dielectric thickness can be minimized. Transition and separation control on the suction side of the wing glove may lead to a reduction of the friction and pressure drag on the whole airfoil.

Finally, the use of actuator arrays staggered in streamwise direction on the wing glove is suggested for an enhancement of the transition delay effectiveness. Multiple actuators and adapted power at each position will reveal further optimization chances even at non-design flight states. Combining the stabilizing effect of DBD actuation with selective cancelation of Tollmien-Schlichting waves has proven outstandingly valuable in wind-tunnel measurements, and needs to be verified in flight. Although additional sensors and sophisticated closed-loop control algorithms are necessary, the effort may eventually lead to a net benefit exceeding the power input, and further enhance the maturity of DBD flow control.

Bibliography

[1] T. Abe, Y. Takizawa, and S. Sato. Experimental study for momentum transfer in a dielectric barrier discharge plasma actuator. *AIAA J.*, 46(9):2248–2256, 2008.

[2] T. Albrecht, R. Grundmann, G. Mutschke, and G. Gerbeth. On the stability of the boundary layer subject to a wall-parallel Lorentz force. *Phys. Fluids*, 18(9):098103–+, Sept. 2006.

[3] B. T. Anderson, R. R. Meyer, and H. R. Chiles. Techniques used in the F-14 variable-sweep transition flight experiment. Technical report, NASA Dryden Flight Research Center, July 1988. Presented at 4th AIAA Flight Test Conference, San Diego, Calif., 1988.

[4] R. Anderson and S. Roy. Preliminary experiments of barrier discharge plasma actuators using dry and humid air. In *44th AIAA Aerospace Sciences Meeting and Exhibit, Reno, Nevada, USA*, 2006. AIAA 2006-0369.

[5] D. Arnal. *Transition, Turbulence and Combustion Modelling*, volume 6 of *ERCOFTAC Series*. Kluwer Academic Publishers, Dordrecht, Netherlands, 1999. ISBN 978-0-7923-5989-5.

[6] D. Arnal and J. Archambaud. Laminar-turbulent transition control: NLF, LFC, HLFC. In *AVT-151 RTO AVT/VKI Lecture Series, Rhode St. Genèse, Belgium (RTO-EN-AVT-151-15)*, pages 9–13, 2008. ISBN 978-92-837-0900-6.

[7] D. Arnal, D. Casalis, and R. Houdeville. Practical transition prediction methods: Subsonic and transonic flows. In *AVT-151 RTO AVT/VKI Lecture Series, Rhode St. Genèse, Belgium (RTO-EN-AVT-151-08)*, 2008. ISBN 978-92-837-0900-6.

[8] N. Bénard and E. Moreau. Effects of altitude on the electromechanical characteristics of a single dielectric barrier discharge plasma actuator. In *41st Plasmadynamics and Lasers Conference, Chicago, Illinois, USA*, Jun. 2010. AIAA 2010-4633.

[9] N. Bénard, N. Balcon, and E. Moreau. Electric wind produced by a single dielectric barrier discharge actuator operating in atmospheric flight conditions - pressure outcome. In *39th Plasmadynamics and Lasers Conference, Seattle, Washington, USA*, 2008. AIAA 2008-3792.

[10] N. Bénard, N. Balcon, and E. Moreau. Electric wind produced by a surface dielectric barrier discharge operating in air at different pressures: aeronautical control insights. *J. Phys. D: Appl. Phys.*, 41(4): 042002 (5pp), Feb 2008.

[11] N. Bénard, N. Balcon, and E. Moreau. Electric wind produced by a surface dielectric barrier discharge operating over a wide range of relative humidity. In *47th AIAA Aerospace Sciences Meeting, Orlando, Florida, USA*, 2009. AIAA 2009-488.

[12] N. Bénard, E. Moreau, J. Griffin, and L. Cattafesta. Slope seeking for autonomous lift improvement by plasma surface discharge. *Exp. Fluids*, 48(5):791–808, 2009.

[13] F. P. Bertolotti. Effect of atmospheric turbulence on a laminar boundary layer. In *XXVI OSTIV Congress, Bayreuth, Germany*, 1999.

[14] J. P. Boeuf, Y. Lagmich, T. Unfer, T. Callegari, and L. C. Pitchford. Electrohydrodynamic force in dielectric barrier discharge plasma actuators. *J. Phys. D: Appl. Phys.*, 40:652–662, Feb. 2007.

[15] A. Bousbia, C. Choucair, D. Freudenhammer, and M. Zimmer. Umgestaltung des Niedergeschwindigkeits-Windkanals (NWK2) der TU Darmstadt. Advanced Design Project, TU Darmstadt, 2011.

[16] L. Brandt, D. Sipp, J. O. Pralits, and O. Marquet. Effect of base-flow variation in noise amplifiers: the flat-plate boundary layer. *J. Fluid Mech.*, 687:503–528, 2011.

[17] L. N. Cattafesta and M. Sheplak. Actuators for active flow control. *Annu. Rev. Fluid Mech.*, 43:247–272, 2011.

[18] T. Cebeci. *An engineering approach to the calculation of aerodynamic flows.* Horizons, Long Beach, California, 1999. ISBN 0966846125.

[19] T. Cebeci and J. Cousteix. *Modeling and Computation of Boundary-Layer Flows.* Springer, Berlin, Germany, 2nd edition, 2005. SIBN 354024459X.

[20] B. J. Chartier, M. Arjomandi, and C. B. S. An investigation on the application of dbd plasma actuators as pressure sensors. In *47th AIAA Aerospace Sciences Meeting, Orlando, Florida, USA*, 2009. AIAA 2009-651.

[21] T. C. Corke, M. L. Post, and D. M. Orlov. Single dielectric barrier discharge plasma enhanced aerodynamics: Physics, modeling and applications. *Exp. Fluids*, 46:1–26, 2009.

[22] A. Drake and R. A. Kennelly. Selected experiments in laminar flow: An annotated bibliography. Technical report, NASA Ames Research Center, Dec. 1992.

[23] A. Duchmann, J. Kriegseis, S. Grundmann, and C. Tropea. Customizing DBD actuators for flow-control applications using PIV. In *8th International Symposium on Particle Image Velocimetry, Melbourne, Australia*, August 2009.

[24] A. Duchmann, A. Reeh, R. Quadros, J. Kriegseis, and C. Tropea. Linear stability analysis for manipulated boundary-layer flows using plasma actuators. In G. M. L. Gladwell, R. Moreau, P. Schlatter, and D. S. Henningson, editors, *Seventh IUTAM Symposium on Laminar-Turbulent Transition*, volume 18 of *IUTAM Bookseries*, pages 153–158. Springer Netherlands, 2010. ISBN 978-90-481-3723-7.

[25] A. Duchmann, D. Vieira, S. Grundmann, M. Schäfer, and C. Tropea. Linear stability analysis of direct numerical simulations of a boundary-layer flow controlled by plasma actuators. In *2nd International Conference on Computational Engineering, October 4-6, Darmstadt*, October 2011.

[26] A. Duchmann, A. Kurz, A. Widmann, S. Grundmann, and C. Tropea. Characterization of Tollmien-Schlichting wave damping by DBD plasma actuators using phase-locked PIV. In *50th AIAA Aerospace Sciences Meeting, Nashville, Tennessee, USA*, 2012. AIAA 2012-903.

[27] A. Duchmann, D. Vieira, S. Grundmann, and C. Tropea. Stabilization of laminar boundary-layer flow using dielectric barrier discharges. In *83rd Annual Meeting of the International Association of Applied Mathematics and Mechanics, March 26 -30, Darmstadt, Germany*, 2012.

[28] A. Duchmann, D. Vieira, S. Grundmann, and C. Tropea. Stabilization of laminar boundary-layer flow using dielectric barrier discharges. In *Proc. Appl. Math. Mech.*, volume 11. Wiley, December 2012.

[29] C. L. Enloe, M. G. McHarg, G. I. Font, and T. E. McLaughlin. Plasma-induced force and self-induced drag in the dielectric barrier discharge aerodynamic plasma actuator. In *47th AIAA Aerospace Sciences Meeting, Orlando, Florida, USA*, 2009. AIAA 2009-1622.

[30] P. Erb. *Untersuchung der Grenzschichttransition im Flugversuch.* PhD thesis, TU Darmstadt, 2002.

[31] A. Filippone. Data and performances of selected aircraft and rotorcraft. *Prog. Aeronaut. Sci.*, 36(8):629–654, 2000. ISSN 03760421.

[32] D. Fisher, K. H. Horstmann, and H. Riedel, editors. *Flight Test Measurement Techniques for Laminar Flow*, volume 23, October 2003. NATO RTO-AG-300-V23. ISBN 92-837-1107-6.

[33] R. Fjørtoft. Application of integral theorems in deriving criteria of stability for laminar flows and for the baroclinic circular vortex. *Geofys. Publ., Oslo*, 17(6):1–52, 1950.

[34] M. Forte, J. Jolibois, J. Pons, E. Moreau, G. Touchard, and M. Cazalens. Optimization of a dielectric barrier discharge actuator by stationary and non-stationary measurements of the induced flow velocity: Application to airflow control. *Exp. Fluids*, 43:917–928, 2007.

[35] J. H. M. Fransson. Investigations of the asymptotic suction boundary layer. Technical report, TRITA-MEK Tech. Rep. 2001:11. Licentiate Thesis, KTH, Stockholm., 2001.

[36] J. H. M. Fransson and P. H. Alfredsson. On the disturbance growth in an asymptotic suction boundary layer. *J. Fluid Mech.*, 482:51–90, 2003.

[37] J. H. M. Fransson, A. Talamelli, L. Brandt, and C. Cossu. Delaying transition to turbulence by a passive mechanism. *Phys. Rev. Lett.*, 96(6):064501, Feb. 2006.

[38] M. Fujino, Y. Yoshizaki, and Y. Kawamura. Natural-laminar-flow airfoil development for a lightweight business jet. *Journal of Aircraft*, 40(4):609–615, 2003.

[39] M. Gad-el-Hak. *Flow control: passive, active, and reactive flow management*. Cambridge University Press, Cambridge, UK, 2000. ISBN 0521770068.

[40] B. Gibson, M. Arjomandi, and R. M. Kelso. The response of a flat plate boundary layer to an orthogonally arranged dielectric barrier discharge actuator. *J. Phys. D: Appl. Phys.*, 45:025202, 2012.

[41] M. B. Glauert. The wall jet. *J. Fluid Mech.*, 1(06):625–643, 1956.

[42] J. W. Gregory, C. L. Enloe, G. I. Font, and T. E. McLaughlin. Force production mechanisms of a dielectric-barrier discharge plasma actuator. In *45th AIAA Aerospace Sciences Meeting and Exhibit, Reno, Nevada, USA*, 2007. AIAA 2007-185.

[43] S. Grundmann. *Transition Control using Dielectric Barrier Discharge Actuators*. PhD thesis, Technische Universität Darmstadt, 2008.

[44] S. Grundmann and C. Tropea. Experimental transition delay using glow-discharge plasma actuators. *Exp. Fluids*, 42(4):653–657, April 2007.

[45] S. Grundmann and C. Tropea. Active cancellation of artificially introduced Tollmien-Schlichting waves using plasma actuators. *Exp. Fluids*, 44:795–806, 2007.

[46] S. Grundmann and C. Tropea. Delay of boundary-layer transition using plasma actuators. In *46th AIAA Aerospace Science Meeting and Exhibit; Reno, Nevada, USA*, 2008. AIAA 2008-1369.

[47] S. Grundmann and C. Tropea. Experimental damping of boundary-layer oscillations using DBD plasma actuators. *Int. J. Heat Fluid Flow*, 30:394–402, 2009.

[48] M. Högberg and D. S. Henningson. Linear optimal control applied to instabilities in spatially developing boundary layers. *J. Fluid Mech.*, 470:151–179, 2002.

[49] K.-H. Horstmann and S. J. Miley. Data report of flight and wind-tunnel investigations of Tollmien-Schlichting waves on an aircraft wing. In *DLR Institutsbericht IB 129-91/18*, 1991.

[50] International Organization for Standardization, Geneva, Switzerland. ISO 2533:1975 standard atmosphere, 1975.

[51] J. Jacob, R. Rivir, C. Carter, and J. Estevadeordal. Boundary layer flow control using ac discharge plasma actuators. In *AIAA 2nd Flow Control Meeting, Portland, Oregon*, 2004. AIAA 2004 - 2128.

[52] J. D. Jacob and K. Ramakumar. Control of laminar and turbulent shear flows using plasma actuators. In *4th International Symposium on Turbulence and Shear Flow Phenomena, Williamsburg, VA*, 2005.

[53] R. D. Joslin. Aircraft laminar flow control. *Annu. Rev. Fluid Mech.*, 30:1–29, Jan. 1998. ISSN 0066-4189, 1545-4479.

[54] T. N. Jukes and K.-S. Choi. Control of unsteady flow separation over a circular cylinder using dielectric-barrier-discharge surface plasma. *Phys. Fluids*, 21(9):094106, 2009.

[55] U. Kogelschatz. Dielectric-barrier discharges: Their history, discharge physics, and industrial applications. *Plasma Chem. Plasma Process.*, 23:1–46, 2003. ISSN 0272-4324.

[56] M. Köhler. Development and implementation of a method for solving the laminar boundary layer equations in airfoil flows. Master thesis, TU Darmstadt, August 2011. URN: urn:nbn:de:tuda-tuprints-31734.

[57] Korff + Co. KG. *Flughandbuch Grob G109b, Triebwerk: Limbach L2400DT1*, 1st edition, March 2002.

[58] J. Kriegseis. *Performance Characterization and Quantification of Dielectric Barrier Discharge Plasma Actuators*. PhD thesis, TU Darmstadt, December 2011.

[59] J. Kriegseis, S. Grundmann, and C. Tropea. Power consumption, discharge capacitance and light emission as measures for thrust production of dielectric barrier discharge plasma actuators. *J. Appl. Phys.*, 110(1):013305, 2011.

[60] J. Kriegseis, B. Möller, S. Grundmann, and C. Tropea. Capacitance and power consumption quantification of dielectric barrier discharge (DBD) plasma actuators. *J. Electrost.*, 69(4):302 – 312, 2011. ISSN 0304-3886.

[61] J. Kriegseis, A. Kurz, A. Duchmann, S. Grundmann, and C. Tropea. Influence of air flow on the performance of DBD plasma actuators. In *50th AIAA Aerospace Sciences Meeting, Nashville, Tennessee, USA*, 2012. AIAA 2012-406.

[62] J. Kriegseis, C. Schwarz, A. Duchmann, S. Grundmann, and C. Tropea. PIV-based estimation of DBD plasma-actuator force terms. In *50th AIAA Aerospace Sciences Meeting, Nashville, Tennessee, USA*, 2012. AIAA 2012-411.

[63] K. Lackhove. Numerische Untersuchung der Ablösekontrolle mit DBD-Plasmaaktuatoren bei einem UAV. Bachelor thesis, TU Darmstadt, April 2011.

[64] G. Lemonis and T. Dracos. A new calibration and data reduction method for turbulence measurement by multihotwire probes. *Exp. Fluids*, 18(5):319–328, 1995. ISSN 0723-4864.

[65] A. V. Likhanskii, M. N. Shneider, S. O. Macheret, and R. B. Miles. Modeling of dielectric barrier discharge plasma actuators driven by repetitive nanosecond pulses. *Phys. Plasmas*, 14(7):073501, 2007. ISSN 1070-664X.

[66] H. Lüdeke, V. Wartemann, and A. Seitz. Direct numerical simulation of Tollmien-Schlichting waves to support linear stability analysis. In *17. DGLR-Fach-Symposium der STAB, Berlin*, Nov. 2010.

[67] Luftfahrtbundesamt. *Gerätekennblatt Nr. 817, Muster: Grob G109*, 11th edition, August 1995.

[68] L. M. Mack. Transition prediction and linear stability theory. Technical Report CP-224, AGARD Laminar-Turbulent Transition, 1977. 22p.

[69] I. Maden, R. Maduta, J. Kriegseis, S. Jakirlic, C. Schwarz, S. Grundmann, and C. Tropea. Experimental and computational study of the flow induced by a plasma actuator. In *9th International ERCOFTAC Symposium on "Engineering Turbulence Modelling and Measurements", Thessaloniki, Greece*, 2012.

[70] P. Magnier, V. Boucinha, B. Dong, R. Weber, A. Leroy-Chesneau, and D. Hong. Experimental study of the flow induced by a sinusoidal dielectric barrier discharge actuator and its effect on a flat plate natural boundary layer. *J. Fluids Eng.*, 131:011203, January 2009.

[71] T. C. Manley. The electric characteristics of the ozonator discharge. *J. Electrochem. Soc.*, 84(1):83–96, 1943.

[72] E. Moreau. Airflow control by non-thermal plasma actuators. *J. Phys. D: Appl. Phys.*, 40:605–636, 2007.

[73] E. Moreau, L. Léger, and G. Touchard. Effect of a dc surface-corona discharge on a flat plate boundary layer for air flow velocity up to 25 m/s. *J. Electrost.*, 64(3-4):215 – 225, 2006.

[74] W. Nitsche and A. Brunn. *Strömungsmesstechnik*, volume 2. Springer Verlag, Berlin, 2006.

[75] C. J. Obara and B. J. Holmes. Flight-measured laminar boundary-layer transition phenomena including stability theory analysis. Technical Report 2417, NASA Technical Paper, April 1985.

[76] S. Pavon, P. Ott, P. Leyland, J.-L. Dorier, and C. Hollenstein. Effects of a surface dielectric barrier discharge on transonic flows around an airfoil. In *47th AIAA Aerospace Sciences Meeting, Orlando, Florida, USA*, 2009. AIAA 2009-649.

[77] I. Peltzer, A. Pätzold, and W. Nitsche. In-flight experiments for delaying laminar-turbulent transition on a laminar wing glove. *Proc. Inst. Mech. Eng., Part G*, 223(6):619–626, 2009.

[78] W. Pfenninger and E. Groth. Low drag boundary layer suction experiments in flight on a wing glove of an F-94A airplane with suction through a large number of fine slots. *Boundary Layer and Flow Control*, II:981–999, 1961.

[79] K. Pohlhausen. Zur näherungsweisen Integration der Differentialgleichung der laminaren Grenzschicht. *ZAMM - Journal of Applied Mathematics and Mechanics / Zeitschrift für Angewandte Mathematik und Mechanik*, 1(4):252–290, Jan. 1921. ISSN 1521-4001.

[80] J. Pons, E. Moreau, and G. Touchard. Asymmetric surface dielectric barrier discharge in air at atmospheric pressure: Electrical properties and induced airflow characteristics. *J. Phys. D: Appl. Phys.*, 38(19): 3635, 2005.

[81] C. Porter, A. Abbas, K. Cohen, T. McLaughlin, and C. L. Enloe. Spatially distributed forcing and jet vectoring with a dielectric barrier discharge plasma actuator. In *46th AIAA Aerospace Sciences Meeting and Exhibit, Reno, Nevada*, 2008. AIAA 2008-1374.

[82] L. Prandtl. Über Flüssigkeitsbewegung bei sehr kleiner Reibung. In *Verhandlungen des dritten internationalen Mathematiker-Kongresses*, volume III, page 484. Teubner, Leipzig, 1904.

[83] R. Quadros. *Numerical Optimization of Boundary-Layer Control using Dielectric Barrier Discharge Plasma Actuator*. PhD thesis, TU Darmstadt, 2009.

[84] A. Reeh. Development and implementation of a method for linear stability analysis in natural and manipulated boundary layer flows. Studienarbeit, TU Darmstadt, 2008.

[85] E. Reshotko. Boundary-layer stability and transition. *Annu. Rev. Fluid Mech.*, 8(1):311–349, 1976.

[86] M. Riherd and S. Roy. Linear stability analysis of a boundary layer with plasma actuators. In *50th AIAA Aerospace Science Meeting and Exhibtion, 09 - 12 January, Nashville, Tennessee*, 2012. AIAA 2012-0290.

[87] J. P. Robert. Special course on skin friction drag reduction. Technical report, AGARD Report 786, 1992.

[88] J. R. Roth, D. Sherman, and S. P. Wilkinson. Boundary layer flow control with a one atmosphere uniform glow discharge surface plasma. In *36th AIAA Aerospace Science Meeting and Exhibit; Reno, Nevada, USA*, 1998. AIAA 1998-0328.

[89] L. J. Runyan, G. W. Bielak, R. A. Behbehani, A. W. Chen, and R. A. Rozendaal. The 757 NLF glove flight test results. Technical report, NASA Langley Research Center, Dec. 1987. Research in Natural Laminar Flow and Laminar-Flow Control, Part 3; p 795-818.

[90] H. Schlichting and K. Gersten. *Grenzschicht-Theorie*. Springer, 2005.

[91] P. J. Schmid and D. S. Henningson. *Stability and transition in shear flows*. Springer, Berlin, 2001. ISBN 9780387989853.

[92] V. Schmitt, J. Archambaud, K. Horstmann, and A. Quast. Hybrid laminar fin investigations. Technical report, RTO Symposium, Braunschweig, Germany, 2000.

[93] J. Schulze. Numerical simulation of various flow conditions on the g-109b research aircraft. Bachelor's thesis, TU Darmstadt, 2010.

[94] A. Seitz. *Freiflug-Experimente zum Übergang laminar-turbulent in einer Tragflügelgrenzschicht*. PhD thesis, TU Braunschweig, 2007. ISRN DLR-FB–2007-01, ISSN 1434-8454.

[95] A. Seitz and K.-H. Horstmann. In-flight investigations of Tollmien-Schlichting waves. In *IUTAM Symposium on One Hundred Years of Boundary Layer Research*, volume 129 of *Solid Mechanics and Its Applications*, pages 115–124. Springer, Berlin, 2006. ISBN 1402041497.

[96] A. Séraudie, E. Aubert, N. Naude, and C. J. P. Effect of plasma actuators on a flat plate laminar boundary layer in subsonic conditions. In *3rd AIAA Flow Control Conference, San Francisco, California*, 2006. AIAA 2006-3350.

[97] A. Séraudie, O. Vermeersch, and D. Arnal. DBD plasma actuator effect on a 2D model laminar boundary layer. Transition delay under ionic wind effect. In *29th AIAA Applied Aerodynamics Conference, Honolulu, Hawaii*, 2011. AIAA 2011-3515.

[98] A. A. Sidorenko, A. D. Budovsky, A. V. Pushkarev, and A. A. Maslov. Flight testing of DBD plasma separation control system. In *46th AIAA Aerospace Sciences Meeting and Exhibit, Reno, Nevada*, 2008. AIAA 2008-3731.

[99] B. Simon. Freiflug-untersuchungen zur laminar-turbulenten transition und deren beeinflussung mit dbd plasma-aktuatoren. Master thesis, TU Darmstadt, 2012.

[100] A. R. Sinclair and A. W. Robins. A method for the determination of the time lag in pressure measuring systems incorporating capillaries. Technical Report Technical Note 2793, National Advisory Commitee for Aeronautics, September 1952.

[101] K. P. Singh and S. Roy. Physics of plasma actuator operating in atmospheric air. *Appl. Phys. Lett.*, 92(11):111502, 2008.

[102] J. H. Spurk. *Strömungslehre: Einführung in die Theorie der Strömungen*. Springer, Berlin, 4. edition, 1996. ISBN 3540613080.

[103] H. B. Squire. On the stability for three-dimensional disturbances of viscous fluid flow between parallel walls. *Proc. R. Soc. London, Ser. A*, 142(847):621–628, 1933.

[104] D. Sturzebecher and W. Nitsche. Active cancellation of Tollmien-Schlichting instabilities on a wing using multi-channel sensor actuator systems. *Int. J. Heat Fluid Flow*, 24(4):572–583, 2003.

[105] M. Takagaki, S. Isono, H. Nagai, and K. Asai. Evaluation of plasma actuator performance in martian atmosphere for applications to mars airplanes. In *4th AIAA Flow Control Conference, Seattle, Washington, USA*, 2008. AIAA 2008-3762.

[106] C. Tropea, A. L. Yarin, and J. F. Foss. *Springer Handbook of Experimental Fluid Mechanics*. Springer, Berlin, 2007. ISBN 9783540251415.

[107] J. A. Valerioti and T. C. Corke. Pressure dependence of dielectric barrier discharge plasma flow actuators. *AIAA J.*, 50(7):1490–1502, 2012. ISSN 0001-1452.

[108] J. L. van Ingen. A suggested semi-empirical method for the calculation of the boundary layer transition region. Technical report, Delft University of Technology, January 1956.

[109] H. R. Velkoff and J. Ketcham. Effect of an electrostatic field on boundary-layer transition. *AIAA J.*, 6:1381–1383, 1968.

[110] P. Versailles, V. Gingras-Gosselin, and H.-D. Vo. Impact of pressure and temperature on the performance of plasma actuators. *AIAA J.*, 48(4):859–863, 2010.

[111] D. Vieira, J. Kriegseis, S. Grundmann, and M. Schäfer. Numerical simulation of boundary-layer stabilization using plasma actuators. In *European Congress on Computational Methods in Applied Sciences and Engineering, Vienna, Austria*, 2012.

[112] A. Wazzan, C. Gazley Jr., and A. Smith. Tollmien-Schlichting waves and transition: Heated and adiabatic wedge flows with application to bodies of revolution. *Prog. Aeronaut. Sci.*, 18:351–392, 1979. ISSN 0376-0421.

[113] J. Weideman and S. Reddy. A MATLAB Differentiation Matrix Suite. *ACM - Transactions on Mathematical Software*, 26(4):465–519, Dec 2000.

[114] M. Weismüller. *A new Approach to Aerodynamic Performance of Aircraft under Turbulent Atmospheric Conditions*. PhD thesis, TU Darmstadt, June 2011.

[115] A. Widmann, A. Duchmann, A. Kurz, S. Grundmann, and C. Tropea. Measuring Tollmien-Schlichting Waves using Phase-Averaged Particle Image Velocimetry. *Exp. Fluids*, 53(3):707 – 715, 2012.

[116] B. Wilke. *Aerodynamische Strömungssteuerung mittels dielektrischen Barriereentladungs-Plasmaaktuatoren*. PhD thesis, Technische Universität Darmstadt, DLR Göttingen, 2009.

[117] A. Winterfeld. Auslegung und Konstruktion einer schwingungsisolierten Instrumentierungs-Plattform für das Forschungsflugzeug G-109b. Studienarbeit, Technische Hochschule Darmstadt, 1988.

[118] Y. Wu, Y. Li, M. Jia, H. Song, Z. Guo, X. Zhu, and Y. Pu. Influence of operating pressure on surface dielectric barrier discharge plasma aerodynamic actuation characteristics. *Appl. Phys. Lett.*, 93 (3):031503, 2008.

[119] D. Zhang, Y. Chew, and S. Winoto. Investigation of intermittency measurement methods for transitional boundary layer flows. *Exp. Therm. Fluid Sci.*, 12(4):433 – 443, 1996. ISSN 0894-1777.

[120] J. G. Ziegler and N. B. Nichols. Optimum settings for automatic controllers. *Trans. ASME*, Vol. 64, No. 1:759–768, 1942.

Nomenclature

Latin letters

upper case

symbol	SI unit	description
A	–	disturbance amplitude
A_0	–	initial disturbance amplitude
A	–	hot wire calibration constant
B	–	hot wire calibration constant
C	F	capacitance
D	$\mathrm{N} = \mathrm{kg\,m/s^2}$	drag
$D_{i,j}$	–	differentiation matrix coefficients
$\boldsymbol{D_1}$	–	first order differentiation operator
$\boldsymbol{D_2}$	–	second order differentiation operator
E	V	voltage
E_Ω	J	total energy across flow domain
F	$\mathrm{N} = \mathrm{kg\,m/s^2}$	force
H_{12}	–	boundary-layer shape factor
I	A	electric current
$\boldsymbol{L}$	–	linear operator
L_p	dB	sound pressure level
Ma	–	Mach number
N	–	N-factor
N	–	vector size
n	–	hot wire calibration constant
P	W	actuator power consumption
$\bar{P}$	W	nominal power consumption
P_{input}	W	input power

P_p	W	propulsion power
Q	C	electric charge
R	Ω	electric resistance
Re	–	Reynolds number
St	–	Strouhal number
T	$\mathrm{N} = \mathrm{kg\,m/s^2}$	thrust
T	K	temperature
T_a	K	ambient temperature
T_d	–	controller differential coefficient
T_i	–	controller integral coefficient
T_j	–	Chebyshev polynomial
U	m/s	flow velocity
U_∞	m/s	free-stream velocity
U_e	m/s	boundary-layer edge velocity
U_{TAS}	m/s	true airspeed
U_{CTA}	m/s	calibrated hot wire velocity
V	V	actuator voltage
V_{pp}	V	actuator voltage amplitude (peak-to-peak)

lower case

symbol	SI unit	description
a	m/s	sonic speed
c	m	chord length
c	m/s	disturbance propagation speed
c_p	–	pressure coefficient
c_D	–	drag coefficient
$c_{D,f}$	–	friction drag component
$c_{D,p}$	–	pressure drag component
c_f	–	friction coefficient
c_L	–	lift coefficient
d	m	thickness of dielectric

f	$\mathrm{N/m^3}$	volume force
f	$\mathrm{Hz} = 1/\mathrm{s}$	disturbance frequency
f_{exc}	Hz	excitation frequency
f_c	Hz	filter cut-off frequency
f_{pl}	Hz	DBD operation frequency
g	$\mathrm{m/s^2}$	acceleration of gravity
h_1	–	grid parameter
k	1/m	wavenumber
k_p	–	controller proportional coefficient
l	m	length scale
m	–	dimensionless pressure gradient
m	kg	mass
m_{MTOW}	kg	maximum take-off weight
p	$\mathrm{Pa} = \mathrm{kg/m\,s^2}$	static gas pressure
p_{t}	Pa	total gas pressure
p_0	Pa	ambient pressure
q	$\mathrm{Pa} = \mathrm{kg/m\,s^2}$	dynamic pressure
$\hat{q}$	–	disturbance shape function
q'	–	disturbance amplitude
s_i	dB/V	microphone calibration factor
t	s	time
u	m/s	velocity component in x-direction
v	m/s	velocity component in y-direction
w	m/s	velocity component in z-direction
x	m	chordwise coordinate
y	m	wall-normal coordinate
z	m	spanwise coordinate

Greek letters

upper case

symbol	SI unit	description
ΔP_p	W	propulsion power saving
Δx_{trans}	m	chordwise transition delay
Φ	°	phase angle
Ψ	–	stream function
Ω	–	flow domain

lower case

symbol	SI unit	description
α	°	angle of attack
α_{FL}	°	Flight Log angle
α_i	°	induced angle of attack
α_{sup}	°	wind tunnel support angle
α_{2D}	°	two-dimensional reference angle of attack
$\dot{\alpha}$	$^\circ/s$	angle of attack change rate
α_i	1/m	streamwise spatial growth rate
β	°	slip angle
β_i	1/m	spanwise spatial growth rate
γ	–	intermittency
δ_N	m	Blasius length scale
δ_1	m	displacement thickness
δ_2	m	momentum loss thickness
ζ	V	control output voltage
η	–	efficiency
$\eta*$	[no standard]	effectiveness
λ	m	wavelength
μ	N s/m^2	dynamic viscosity

ν	m^2/s	kinematic viscosity
ξ	–	Gauss-Lobatto grid points
ρ	kg/m^3	density
σ	–	standard deviation
τ_w	$Pa{=}N/m^2$	wall-shear stress
ϕ	–	relative humidity
ψ	–	control input
ω	$1/s$	angular frequency

Mathematical symbols

symbol	description
∇	del operator
*	dimensional quantity
∂	partial derivative
$\bar{}$	averaged quantity
$\hat{}$	quantity amplitude
$'$	fluctuation quantity

Abbreviations

symbol	description
a	ambient
AC	alternating current
AWC	active wave cancelation
CCD	charged coupled device
CFD	computational fluid dynamics
corr	corrected
crit	critical
CTA	constant temperature anemometry
DBD	dielectric barrier discharge
DEHS	di-ethyl-hexyl-sebacat
DNS	direct numerical simulation
EHD	electro-hydrodynamic
FL	Flight Log
FFT	fast Fourier transform
HLFC	hybrid laminar flow control
HV	high voltage
KTH	Kungliga Tekniska högskolan
lam	laminar

LBA	Luftfahrt Bundesamt
LDA	laser Doppler anemometry
LES	large eddy simulation
LFC	laminar flow control
LFU	Leichtflugtechnik Union GmbH
LSA	linear stability analysis
max	maximum
meas	measured
MHD	magneto-hydrodynamic
min	minimum
MTOW	maximum take-off weight
Nd:YAG	neodymium-doped yttrium aluminum garnet
NLF	natural laminar flow
NWK	Göttinger-type wind tunnel facility
NWK2	Eiffel-type wind tunnel facility
PIV	particle image velocimetry
PSD	power spectral densitiy
PSE	parabolized stability equations
RANS	Reynolds averaged Navier-Stokes
ref	reference
RMS	root mean square
sup	support
SNR	signal-to-noise ratio
trans	transition
TS	Tollmien-Schlichting
TU	Technische Universität
turb	turbulent
UAV	unmanned aerial vehicle
w	wall
W	wire
2D	two-dimensional
3D	three-dimensional

List of Figures

List of Tables

Alexander Joachim Duchmann

Born on April 28, 1982, in Frankfurt am Main, Germany

Education

02/2008 - 10/2012	Doctoral Research in Mechanical Engineering, Technische Universität Darmstadt, Darmstadt, Germany
10/2002 - 01/2008	Studies in Mechanical Engineering (Dipl.-Ing.), Technische Universität Darmstadt, Darmstadt, Germany
09/2004 - 10/2005	ERASMUS Study Period Abroad, Universitat Politècnica de Catalunya, Barcelona, Spain
08/1992 - 05/2001	Liebigschule, Frankfurt am Main, Germany
07/1988 - 07/1992	Hartmutschule, Eschborn, Germany

Employment

since 03/2013	Development Engineer Flight Test Analysis Eurocopter Deutschland GmbH, Germany
02/2008 - 02/2013	Research Assistant Institute for Fluid Mechanics and Aerodynamics, Technische Universität Darmstadt, Germany
05/2007 - 11/2007	Research Assistant Department of Aerospace and Ocean Engineering, Virginia Polytechnic Institute and State University, Blacksburg, VA, USA
07/2005 - 10/2005	Internship Lufthansa Technik AG, Frankfurt, Germany